Epigenetic Responses to

Methyl-Metabolite Depletion

By

Spencer Allen Haws

A dissertation submitted in partial fulfillment of

the requirements for the degree of

Doctor of Philosophy

(Nutritional Sciences)

at the

UNIVERSITY OF WISCONSIN-MADISON

2021

Date of final oral examination: 4/22/2021

This dissertation is approved by the following members of the Final Thesis Committee:

John M. Denu, Professor, Department of Biomolecular Chemistry
Rozalyn M. Anderson, Associate Professor, Department of Medicine
Richard S. Eisenstein, Professor, Department of Nutritional Sciences
Dudley W. Lamming, Associate Professor, Department of Medicine
Rupa Sridharan, Associate Professor, Department of Cell and Regenerative Biology

Epigenetic Responses to Methyl-Metabolite Depletion

Spencer Allen Haws

Under the supervision of Professor John M. Denu
At the University of Wisconsin-Madison

Chemical modifications to DNA and histone proteins comprise the epigenome. Histone lysine methylation (K_{me}), a critical regulatory epigenetic modification, is deposited by histone methyltransferase (HMTs) enzymes that utilize S-adenosylmethionine (SAM) as their methyl-donor cofactor. SAM is the downstream metabolite of methionine in the methionine cycle, which is the only pathway known to support higher order eukaryote SAM availability. As a result, perturbations to methionine/SAM metabolism (i.e., methyl-donor metabolism) are capable of directly influencing HMT activity and subsequently chromatin biology/biochemistry. Interestingly, all forms of K_{me} are not equally sensitive to SAM deprivation despite their shared reliance on this cofactor. Therefore, the goal of this work was to determine whether epigenetic mechanisms exist which respond to decreased SAM availability and actively regulate specific K_{me} modifications to preserve essential chromatin functions.

Chapter 1 introduces the interdependence of metabolism and the epigenome which provided the conceptual foundation for these studies. In Chapter 2, I build upon this foundation and investigate the presence of conserved epigenetic responses to methyl-metabolite depletion using *in vitro* and whole-organism model systems. Through carefully designed and executed molecular biology, analytical chemistry, and biochemistry experiments, I uncovered a highly conserved epigenetic response to methyl-metabolite depletion at H3 Lys9 (H3K9). This response

comprised of active H3K9 mono-methylation in the presence of global losses in H3K9me2/3. I determined H3K9me1 is actively maintained by cytoplasmic and nuclear HMTs to acutely preserve heterochromatin stability and support long-term epigenetic persistence to methyl-metabolite depletion. This epigenetic response was preserved in young and aged C57BL/6J mice, highlighting the physiological relevance of these findings. Chapter 3 details development of the radiometric EZ-Tip (Enzyme Tip) Assay used in Chapter 4 to determine whether fundamental catalytic properties of H3K9me1 HMTs facilitate their preferential activity during methyl-metabolite depletion. Indeed, quantitative biochemical assessment of three distinct H3K9 HMT pairs revealed K_{me} multiplicity negatively impacts the rate of HMT catalysis, resulting in increased efficiency for H3K9 mono-methylation relative to di-/tri-methylation reactions. Together, this work revealed a critical epigenetic response to a metabolic perturbation and uncovered its mechanistic foundation. Conclusions and implications for future studies are presented in Chapter 5.

Acknowledgements

I would first like to thank my Ph.D. mentor, Dr. John M. Denu, for his patience, guidance, and enthusiasm over the course of my training. Your passion for science is inspiring and has fueled my motivation to discover. I feel grateful to have been able to work with you and am hopeful for more opportunities to interact as colleagues and friends in the future.

I would like to thank my thesis committee members Dr. Rozalyn M. Anderson, Dr. Richard S. Eisenstein, Dr. Dudley W. Lamming, Dr. David J. Pagliarini (former), and Dr. Rupa Sridharan for the direction you have provided throughout my training. You were all truly an invaluable resource for both my scientific and professional development.

I would like to thank the scientific collaborators I have had the pleasure of working with and learning from. From outside of the University of Wisconsin-Madison, this includes Dr. Benjamin Tu (University of Texas Southwestern Medical Center), Dr. Kazuhiko Igarashi (Tohoku University), Dr. Holly Brown-Borg (University of North Dakota), Dr. Peter Kaiser (University of California Irvine), Dr. Julie Ahringer (Cambridge University), and Dr. Raymond Trievel (University of Michigan). From within the University of Wisconsin-Madison, this includes Dr. Dudley W. Lamming, Dr. Vincent Cryns, Dr. Rozalyn M. Anderson, Dr. Rupa Sridharan, Dr. Richard S. Eisenstein, Dr. Eric Yen, and Dr. Bermans Iskandar.

I would like to thank the NIH T32 Metabolism and Nutrition Training Program, led by Dr. Richard S. Eisenstein, for providing both financial support and professional development opportunities during my training. Many of my most impactful experiences stemmed from this training program and as a result I cannot thank you enough for your efforts.

I would like to thank both past and present members of the Denu laboratory that I was able to learn from and share this unique experience with; Eric Armstrong, Dr. Josue Baeza, Dr.

Sherry Bakhtiar, Julie Bolding, Bianca Chavez, Ann Denu, Dr. Rush Dhillon, Dr. James Dowell, Dr. Jing Fan, Jessica Han, Dr. Mark Klein, Dr. Kimberly Krautkramer, Dr. Slava Kuznetsov, Alexis Lawton, Dr. Jin-Hee Lee, Cassie Leech, Dr. Ana Lindahl, Dr. Wallace Liu, Lily Miller, José Moran, Michael Smallegan, Dr. Zhangli Su, Sydney Thomas, and Yiming Qin. It is exciting to know fellow graduate student Cassie Leech is following up on some of this work where I left off and making it her own. I cannot wait to see the discoveries she makes and where the project leads her. I also want to specifically thank Mark Klein for his camaraderie and support over the years. I am proud to call Mark a friend and look forward to sharing more experiences together in the future.

I would like to thank my parents, Troy and Dawn, my brother and sister-in-law, Bryce and Clara, and my sister, Paige, for their love and support. I know I am lucky to have a supportive family behind me and it is not something I take for granted.

Lastly, I would like to thank my wife, Stephanie, most of all for her flexibility, understanding, and encouragement as I worked towards this Ph.D. Your willingness and openness to make sacrifices so I could pursue my dream is something I will forever be thankful for. I love you, and hope I made you proud.

TABLE OF CONTENTS

LIST OF FIGURES

LIST OF TABLES

Chapter 1: Introduction – Metabolism and the Epigenome: A Dynamic Relationship

Spencer A. Haws[1,2], Cassandra M. Leech[1,2], and John M. Denu[1,2]

[1]Wisconsin Institute for Discovery, University of Wisconsin-Madison
[2]Department of Biomolecular Chemistry, SMPH, University of Wisconsin-Madison

*This chapter was published in Trends in Biochemical Sciences. 2020 May 6; 45: 731-747.

1.1 Abstract

Many chromatin modifying enzymes require metabolic cofactors to support their catalytic activities, providing a direct path for fluctuations in metabolite availability to regulate the epigenome. Over the past decade, our knowledge of this link has grown significantly. What began with studies showing cofactor availability drives global abundances of chromatin modifications has transitioned to discoveries highlighting metabolic enzymes as loci-specific regulators of gene expression. Here, I cover our current understanding of mechanisms that facilitate the dynamic and complex relationship between metabolism and the epigenome, focusing on the roles of essential metabolic and chromatin associated enzymes. I also discuss physiological conditions where availability of these 'epi-metabolites' are dynamically altered, highlighting known links to the epigenome and proposing other plausible connections.

1.2 Introduction: Metabolic Links to the Epigenome

In eukaryotic organisms, the storage and accessibility of genomic DNA is regulated at the level of the nucleosome core particle. Along with DNA, each nucleosome particle contains an octamer of histone proteins that are small, positively charged, and globular with flexible N-terminal "tails" that protrude from the larger structure. Due to their accessibility and amino acid composition, the protruding "tails" act as a platform for reversible, chemical post-translational modifications (PTMs) that then alter chromatin structure and function. This post-translational regulation of chromatin occurs through two major mechanisms: 1.) PTMs change the intrinsic chemical properties of the amino acids (e.g., acetylation-dependent charge neutralization) and can induce structural changes to chromatin, and/or 2.) PTMs are recognized by "reader" proteins that function to recruit additional chromatin effectors. Similar to histones, DNA can also be chemically modified to regulate gene expression. Together, chemical modification of histones and DNA comprise the epigenome.

Metabolism is believed to be a principal regulator of the epigenome as nearly all chromatin modifying enzymes require central metabolites (Figure 1-1, Table 1-1) as cofactors to support their catalytic activities. However, this metabolism-epigenome link appears to be more interesting and complex than simply chromatin modifying enzymes siphoning off choice metabolites from canonical metabolic pathways. Recently, metabolic enzymes have also been shown to moonlight as context-dependent regulators of the epigenome, introducing an emerging aspect to this dynamic relationship.

In this review, I will cover our current understanding of how essential metabolic cofactors and enzymes are able to dynamically regulate the acetyl-, acyl-, and methyl-states of the epigenome. I will highlight the chromatin effector proteins that mediate and sense these

changes to the epigenome with a focus on the transcriptional consequences. Finally, I will cover physiological states (e.g., circadian cycles, aging, dietary perturbations, and diseases) associated with altered epigenetic cofactor metabolism, discussing known and potential links with the epigenome.

Figure 1-1: Central Metabolites are Essential Cofactors for Chromatin Modifying Enzymes. Central metabolites from diverse metabolic pathways are essential cofactors (in bold) for the chromatin modifying enzymes that regulate the epigenome. Abbreviations: α-KG, α-ketoglutarate; CoA, coenzyme A; DNMT, DNA methyltransferase; HAT, histone acetyltransferase; HDM, histone demethylase; HMT, histone methyltransferase; NAM, nicotinamide; OAA, oxaloacetic acid; SAH, S-adenosylhomocysteine; SAM, S-adenosylmethionine; TCA, tricarboxylic acid; TET, ten eleven translocation DNA demethylase.

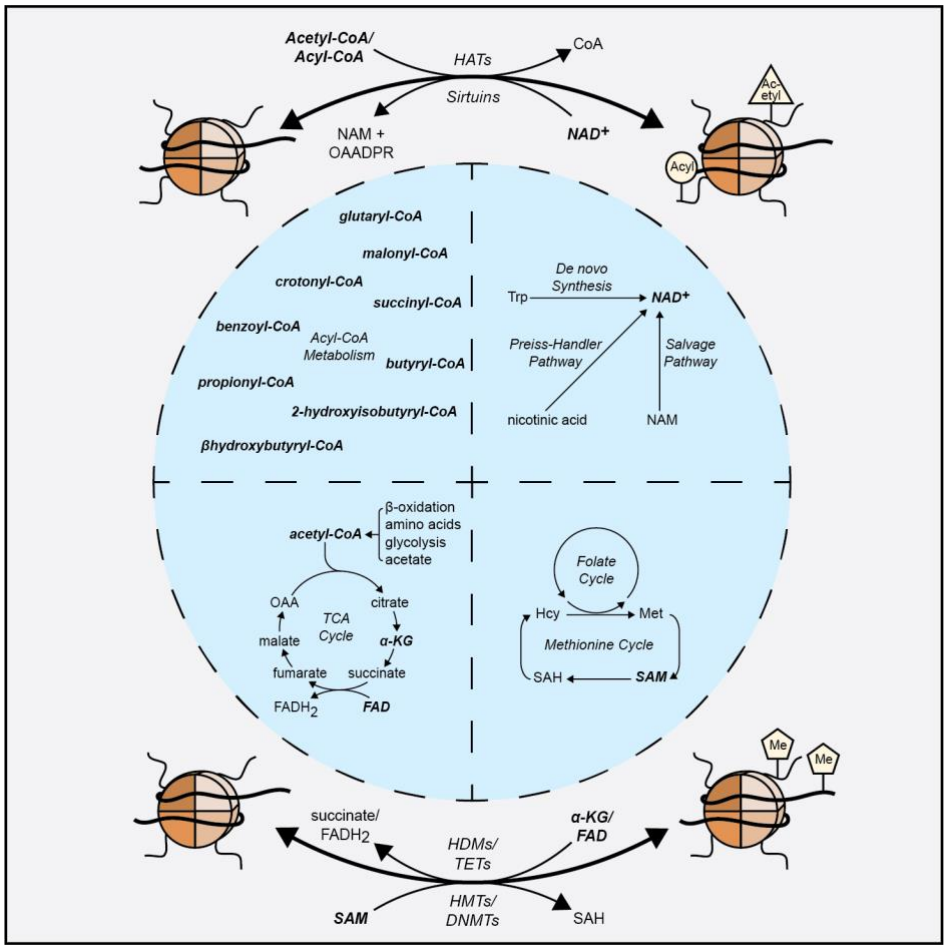

Table 1-1: Essential Cofactors for Chromatin Modifying Enzymes. Information on metabolite cofactors and the chromatin modifications that they support,

Cofactor	Structure	Associated Metabolic Pathways	Supported Chromatin Modifying Reaction(s)	Common "Reader" Domains of Effectors	Citations
Acetyl-CoA		Glycolysis; TCA Cycle; FA Oxidation; Amino Acid Catabolism; Acetate Metabolism	Histone Acetylation	Bromo; YEATS; DPF	1,9,11
Acyl-CoA		FA Oxidation; Ketogenesis; Amino Acid Catabolism	Histone Acylation	YEATs; DPF	1,8
SAM	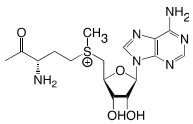	1C Metabolism; (Methionine and Folate Cycles); Phospholipid Synthesis	Histone Methylation; DNA Methylation	Chromo; PHD; Tudor, PWWP; TTD; MBD	56,64,68
NAD^+	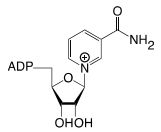	Amino Acid Catabolism; Preiss-Handler Pathway; NAM Salvage	Histone Deacetylation; Histone Deacylation; Histone ADP-Ribosylation	Bromo; YEATS; DPF; PBZ; WWE; Macro-	34,36,112
α-KG	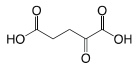	TCA Cycle; Amino Acid Metabolism	Histone Demethylation; DNA Demethylation	Chromo; PHD; Tudor, PWWP; TTD; MBD	81,83,86
FAD	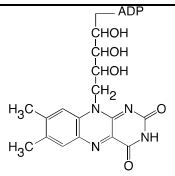	TCA Cycle; Oxidative Phosphorylation	Histone Demethylation	Chromo; PHD	81–83

1.3 Metabolite-Dependent Chromatin Modifying Reactions

1.3.1 Histone Acetylation

Acetylation of the histone lysine ε-amino group (K_{acetyl}) is catalyzed by histone acetyltransferases (HATs) (Figure 1-2A, 1-2B). Three primary families of HATs have been identified (GNAT, MYST, and p300/CBP), all requiring acetyl-CoA as the acetyl-donating cofactor [1]. Histone K_{acetyl} supports accessible, transcriptionally active chromatin environments through two distinct yet complementary mechanisms: 1.) neutralization of electrostatic interactions that contribute to higher-order chromatin structure and 2.) by acting as a ligand for K_{acetyl} "readers." For example, H4 Lys16 acetyl (H4K16ac) can disrupt electrostatic interactions *in vitro* between the H4 tail on one nucleosome particle and an acidic patch on the H2A:H2B dimer of the neighboring particle [2]. Disruption of these interactions is thought to support X-chromosome dosage compensation in *Drosophila* and lost transcriptional silencing in *S. cerevisiae* [3–5]. In addition, K_{acetyl} influences chromatin structure and function through its recognition by bromodomain-, YEATS domain-, and double PHD finger (DPF) domain-containing proteins [1]. By interacting with an acetyl-lysine residue, these epigenetic "readers" can recruit effectors (e.g. super elongation complex, transcription factors, ATP-dependent chromatin remodelers) that support transcriptional activation at specific genomic loci [6–8].

Several enzymes are capable of generating the acetyl-CoA needed to support HAT reactions (Figure 1-2C). In mitochondria, acetyl-CoA can be generated by the pyruvate dehydrogenase complex (PDC), as a product of fatty acid oxidation, via amino acid degradation, or synthesized from free acetate by acyl-CoA synthetase short-chain family members 1 and 3 (ACSS1/ACSS3) [9]. However, as there is no mitochondrial acetyl-CoA exporter, acetyl-CoA must first be combined with oxaloacetate (OAA) to form citrate, which escapes mitochondria via

the citrate shuttle. Once in the cytoplasm and/or nucleus, ATP-citrate synthase (ACLY) can convert the citrate back to acetyl-CoA and OAA [10]. In addition to ACLY, acyl-CoA synthetase short-chain family member 2 (ACSS2) and PDC have been implicated as nuclear acetyl-CoA synthesizing enzymes [11–13].

The catalytic activity of all three nuclear acetyl-CoA synthesizing enzymes (PDC, ACLY, and ACSS2) can maintain global histone K_{acetyl} levels [12–14]. However, ACLY and ACSS2 appear capable of supporting loci-specific histone K_{acetyl} under unique contexts. For example, ACLY-dependent K_{acetyl} drives the expression of key glycolytic genes during the differentiation of preadipocytes into mature adipocytes while ACSS2-dependent K_{acetyl} is a critical regulator of memory-related neuronal genes in the murine hippocampus [13–15]. These independent chromatin regulatory functions for ACLY and ACSS2 may be dictated, in part, by the production and/or flux of their respective substrates, citrate and acetate (Figure 1-2C). Such a mechanism would allow disparate metabolic states that affect acetyl-CoA precursor availability (e.g. hypoglycemia, ketosis, alcohol consumption, etc.) to initiate distinct chromatin responses.

Figure 1-2: Reversible Histone Acetylation/Acylation Reaction Diagrams and Acetyl-CoA Metabolism Schematic. (*A, B*) Enzyme reaction diagrams illustrating the reversibility of histone lysine acetylation/acylation for Class I, II, and IV histone deacetylases (HDACs) (*A*) as well as Class III HDACs (*B*). (*C*) Schematic detailing acetyl-CoA metabolism and enzymes implicated in regulating global and/or loci specific histone acetyltransferase (HAT) reactions.
Abbreviations: ACLY, ATP-citrate synthase; ACSS1–3, acyl-CoA synthetase short-chain family member 1–3; OAA, oxaloacetic acid; PDC, pyruvate dehydrogenase complex.

Figure 1-2: Reversible Histone Acetylation/Acylation Reaction Diagrams and Acetyl-CoA Metabolism Schematic.

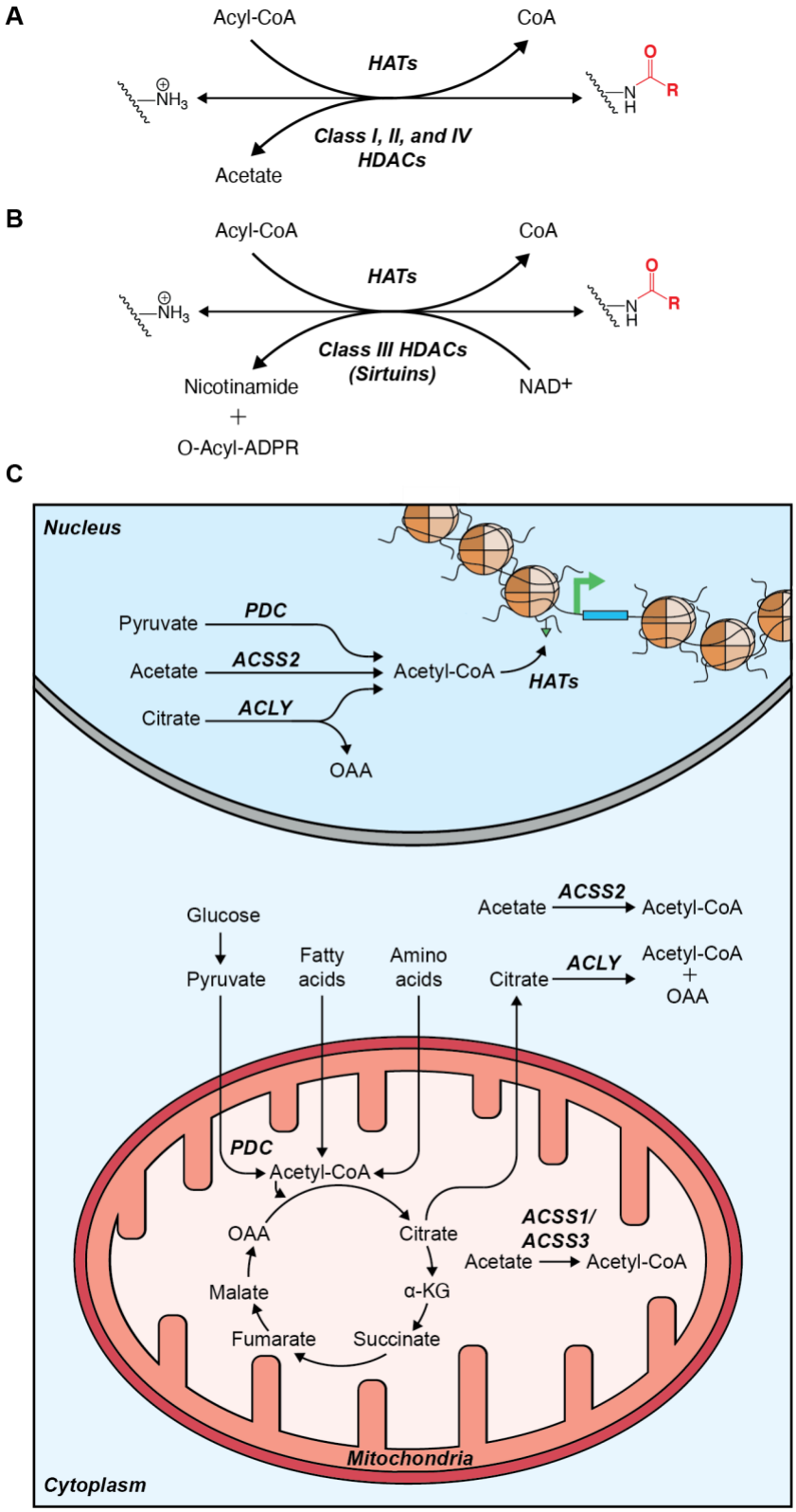

1.3.2 Histone Acylation

Non-acetyl histone acylations are an emerging classification of PTM and will be referred to as acylations for the remainder of this review. Currently, nine unique lysine acylations (K_{acyl}) have been identified on histones, many of which are added enzymatically by HATs (Figure 1-3A) [16–23]. Lysine malonylation and succinylation may occur in significant quantities through non-enzymatic mechanisms, given that the corresponding acyl-CoA precursors are more prone to intramolecular catalysis and anhydride formation relative to shorter-chain acyl-CoA molecules [24,25]. Acylation of the lysine ε-amino group can be recognized by proteins containing YEATs and DPF domains. These K_{acyl} "reader" domains possess substrate binding pockets with higher affinities for K_{acyl} over K_{acetyl} although this is accomplished through disparate mechanisms [26–30]. YEATs domains preferentially accommodate K_{acyl} PTMs through aromatic residue π-stacking (Figure 1-3B). DPF domains, like bromodomains, rely on polar contacts with the substrate but are more structurally accommodating to acyl chains and can also utilize π-stacking to improve specificity for K_{acyl} residues (Figure 1-3C, 1-3D). These specific binding capabilities facilitate the unique functions for K_{acyl} relative to K_{acetyl} PTMs in regulating gene expression. For example, in *S. cerevisiae*, the metabolic switch from oxidative to fatty acid metabolism correlates with decreased H3K9ac and a corresponding increase in H3 Lys9 crotonyl (H3K9cro) abundance [31]. H3K9cro is then recognized by the YEATs domain-containing protein Taf14, mediating reduced expression of pro-growth genes [31].

Unlike acetyl-CoA, the metabolic enzymes responsible for generating acyl-CoAs for chromatin acylation are not as well understood. Some acyl-CoAs are known to be generated within mitochondria (e.g. crotonyl-, malonyl-, succinyl-, and glutaryl-CoA), while others are present primarily as short chain fatty acids (SCFAs) or ketone bodies, requiring CoA-

conjugation to be used as a cofactor. Tracing experiments have shown cells possess the ability to incorporate such metabolites directly onto chromatin, which may be mediated by promiscuous activity of ACSS enzymes [1,20,32]. In addition to enzymes that synthesize acyl-CoA molecules, catabolic enzymes also influence acyl-CoA abundance. Propionyl-CoA carboxylase alpha subunit knockout mice ($PCAA^{-/-}$) accumulate propionyl-CoA, leading to increased global H3 Lys14 proprionyl (H3K14pro) [33]. Knockout of the butyryl-CoA catabolizing enzyme acyl-CoA dehydrogenase short-chain ($ACADS^{-/-}$) also stimulates liver butyryl-CoA accumulation, but unexpectedly, has no effect on H3 Lys14 butyryl (H3K14bu) abundance [33]. Together, these findings suggest increased acyl-CoA concentrations do not always drive increased *de novo* histone acylation. Such observations implicate acyl-CoA sub-cellular compartmentalization and/or HAT activity as a critical regulator of K_{acyl} patterns.

Figure 1-3: Lysine Acylations Are Chemically Diverse and Recognized by Unique Domains. (*A*) Chemical structures for all identified histone lysine acylations. (*B*) Crystal structure surface diagram of $K_{crotonyl}$ in the YEATs domain binding pocket of human AF9 (PDB: 5HJB). π stacking is facilitated by residues F59 and Y78. (*C*) Crystal structure surface diagram of $K_{crotonyl}$ in the DPF domain binding pocket of human MORF (PDB: 6OIE). S217 and S242 make polar contacts (mediated by a water molecule) with the crotonylated lysine. F218 improves specificity for $K_{crotonyl}$ over K_{acetyl} through π stacking. (*D*) Crystal structure surface diagram of K_{acetyl} in the bromodomain binding pocket of human BRPF1 (PDB: 5FFV). N708, a conserved residue in bromodomains, makes the sole polar contact with the acetylated lysine.

Figure 1-3: Lysine Acylations Are Chemically Diverse and Recognized by Unique Domains.

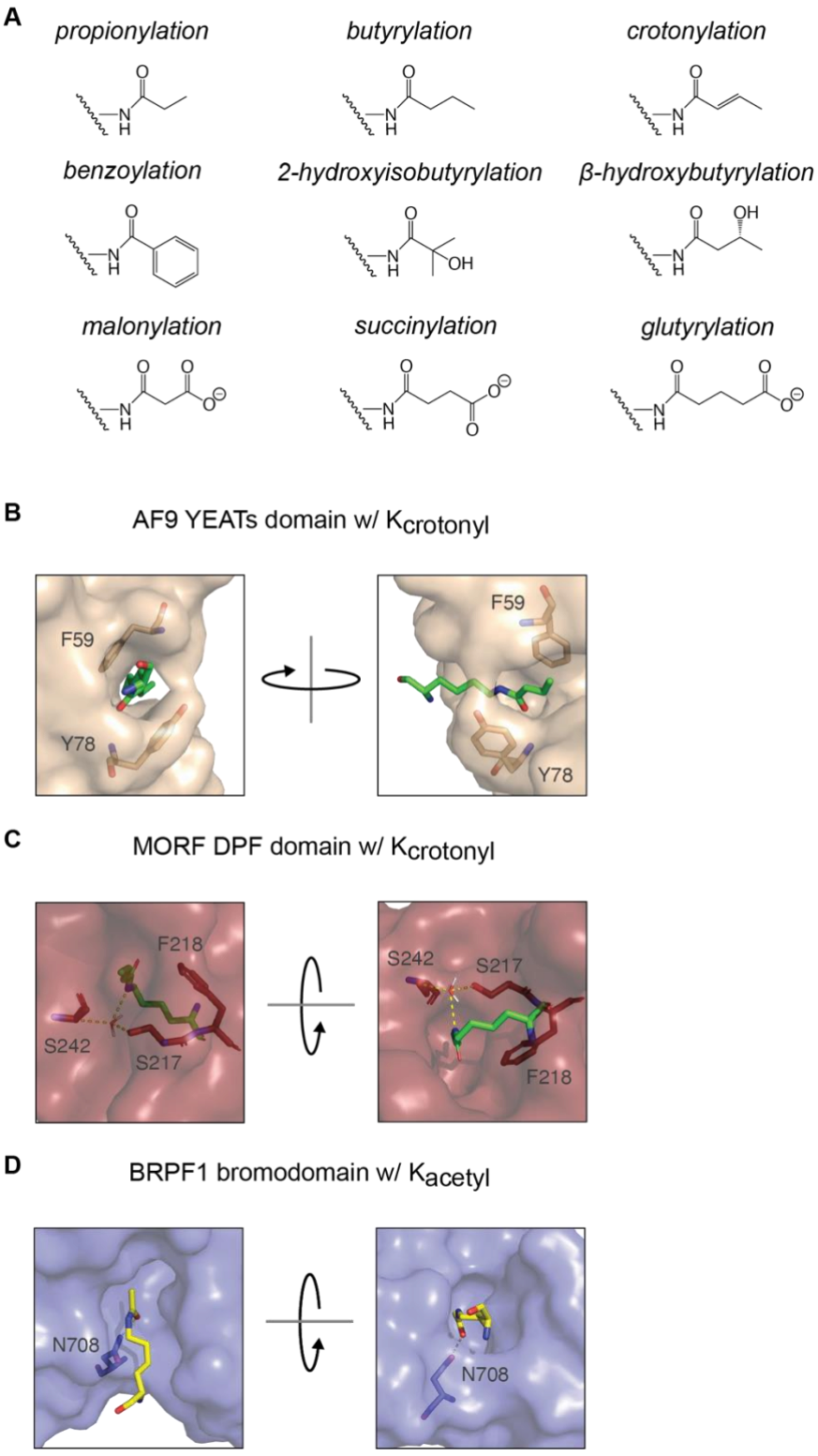

1.3.3 Histone Deacetylation/Deacylation

Four main classes of histone deacetylases (HDACs) have been defined in mammalian cells: Class I, II, III, and IV, although only Class III HDACs require a metabolic cofactor to support catalytic activity (Figure 2A and 2B). These class III HDACs, also known as sirtuins, utilize a nicotinamide adenine dinucleotide (NAD^+) molecule during catalysis. The reaction involves cleavage of the nicotinamide glycosidic bond and transfer of the acetyl-group from substrate to ADP-ribose, yielding nicotinamide (NAM) and *O*-acetyl-ADP-ribose (*O*AADPR) as additional products (Figure 1-2B) [34]. The seven mammalian sirtuins regulate diverse aspects of cell biology both in and outside the nucleus. Sirtuins 3-5 reside primarily within mitochondria, acting as protein deacetyl/deacylases, while SIRT1, SIRT2, SIRT6, and SIRT7 can target histones for nuclear deacetylation [34,35]. Given this family of enzymes' dependence on a single cofactor, adequate NAD^+ levels are critical for supporting sirtuin activity.

NAD^+ synthesis occurs through three primary mechanisms within the cell: 1.) *de novo* synthesis from tryptophan, 2.) the Preiss-Handler pathway, and 3.) the NAM salvage pathway [36]. The *de novo* NAD^+ synthesis and Preiss-Handler pathways are relatively minor generators of NAD^+ while the NAM salvage pathway is the major NAD^+ contributor [36,37]. NAD^+ molecules are the preferred cofactor for two-electron transfer redox reactions, resulting in reversible NADH formation. Unlike redox enzymes, sirtuin activity is not regulated by NAD^+:NADH ratios, but is instead thought to be regulated by NAD^+ abundance [38–41].

In addition to functioning as lysine deacetylases, sirtuins are capable of more general lysine deacylation. These distinct specificities are best described with sirtuins (SIRT3-5) found in mitochondria, where diverse acyl-modifications appear more prevalent. However, early evidence that sirtuins were capable of more than just deacetylation came from enzymology

studies with nuclear/cytoplasmic enzymes SIRT1 and SIRT2 [42,43], paving the way for a systematic biochemical investigation of the deacylation capabilities of SIRT1-6 [44]. Surprisingly, long-chain deacylase activity was a common activity among sirtuins [44]. However, unlike SIRT1 and SIRT2, SIRT6 deacetylation and short chain (≤ crotonyl) deacylation activity were almost non-detectable [44]. In that study, Feldman et al demonstrated that free fatty acids (FFAs) could stimulate the catalytic activity for deacetylation. Following reports indicated that non-fatty acid small molecules are also able to significantly improve SIRT6 deacetylation and deacylation kinetics [44–46]. Small molecule activators with varying degrees of *in vivo* efficacy have been identified for SIRT1 as well, reviewed in depth by Hubbard and Sinclair [47]. Together, these findings propose a mechanism by which metabolites distinct from NAD^+ can stimulate sirtuin-dependent deacetylation/deacylation to regulate gene expression. A recent study provided *in situ* evidence in support of this model, suggesting perilipin 5 acts as a carrier protein to deliver endogenous monounsaturated fatty acids (MUFAs) from lipid droplets to the nucleus [48]. Once in the nucleus, these MUFAs can stimulate SIRT1-dependent deacetylation and activation of the transcriptional co-regulator PGC-1α [48].

Although sirtuins are the only HDACs requiring metabolic cofactors to support catalytic activity, the short chain fatty acid (SCFA) metabolites butyrate and propionate are known catalytic inhibitors of Class I and II HDACs (Figure 1-2A). These SCFAs possess low- to mid-micromolar HDAC inhibitory IC_{50} values, falling in range of natural circulating concentrations [49–51]. Butyrate, having a lower IC_{50} value than propionate, is also the better studied *in vivo* HDAC inhibitor. For example, it has been shown that butyrate accumulation in cancerous colonocytes drives expression of pro-apoptotic genes through increased histone acetylation levels [52]. Interestingly, although these metabolites are known to be primarily generated via

microbiota-dependent fermentation of non-digestible carbohydrates in the gut, they have also been shown to influence the epigenetic states of proximal host tissues [53,54]. While this is an exciting discovery that suggests a general mechanism by which microbiota are capable of influencing systemic host physiology, more studies are needed to determine the functional consequences of this microbial metabolism:host-chromatin axis.

1.3.4 Histone Methylation

Histone methylation reactions are catalyzed in a site-specific manner by histone methyltransferases (HMTs), most commonly on the ε-amino group of lysine residues (Figure 1-4A). Histone arginine methylation also occurs in the nucleus; however, here I focus on the metabolic influences over lysine methylation (K_{me}). For more information on arginine methylation, please see the review by Guccione and Richard [55].

K_{me} provides the most chemical diversity to the epigenome. Although only eight residues (e.g. H3K4/9/18/23/27/36/79 and H4K20) are sites of significant K_{me}, each lysine can support three unique methylation states (i.e. mono-, di-, or tri-methylation), resulting in $4.3x10^9$ possible permutations of K_{me} for a given nucleosome. K_{me} is capable of supporting transcriptionally active or repressive chromatin environments, depending on the context [56]. This diverse functionality is facilitated by unique "reader" proteins that require specific methylation states *and* neighboring amino acids to interact with a given residue, enabling similar K_{me}-states to have drastically different effects on the chromatin environment. For example, H3K4me3 can be "read" by some PHD-containing transcription factors to facilitate chromatin remodeling and preinitiation complex formation at transcription start sites [57–59]. Opposingly, H3K9me2/3 can be "read" by the chromodomain-containing heterochromatin protein 1a which acts as a scaffold to recruit effector proteins that promote transcriptional silencing through the initiation and maintenance of constitutive heterochromatin [60].

All HMTs require S-adenosylmethionine (SAM) as the methyl-donor cofactor. In mammals, intracellular SAM is generated as a product of ATP-dependent methionine adenosyltransferase (MAT) reactions [61]. MAT reactions are catalyzed by only two known enzymes, MATIα and MATIIα. MATIα is expressed exclusively in the liver while MATIIα is

ubiquitously expressed across tissues [61]. A third MAT protein, MATIIβ, possesses no inherent catalytic activity. Instead, MATIIβ functions as a regulatory binding partner of MATIIα, decreasing the enzyme's $K_{m,\ MET}$ while also increasing MATIIα's susceptibility to product inhibition [62,63]. These MAT-dependent SAM synthesis reactions are found at the core of one carbon metabolism, where the folate and methionine cycles converge, providing numerous avenues by which metabolic perturbations can influence SAM synthesis (Figure 1-4C) [64].

Limiting SAM availability by disrupting the metabolism and availability of its precursors can directly influence histone K_{me} abundance. In mouse embryonic stem cells (mESCs), disrupting the catabolism of threonine to glycine, an upstream SAM precursor, significantly reduces SAM availability as well as H3K4me2/3 abundance [65]. Subsequent studies corroborated this seminal study, highlighting the susceptibility of higher state (i.e. di- and tri-) histone K_{me} to decreased SAM availability [64]. Altered SAM abundance as a consequence of impaired or enhanced phospholipid metabolism has also been shown to directly influence histone methylation abundance [66,67]. Together, these direct correlations between global SAM availability and histone K_{me} highlight histone methylation as one of the most metabolically sensitive PTMs.

Figure 1-4: Reversible Chromatin Methylation Reaction Diagrams and SAM Metabolism Schematic. Enzyme reaction diagrams illustrating reversibility of histone (*A*) and DNA (*B*) methylation. (*C*) Schematic highlighting position of SAM- synthesizing reactions at the crossroads of the folate and methionine cycles. Abbreviations: BER, base excision repair; DNMT, DNA methyltransferase; HDM, histone demethylase; HMT, histone methyltransferase; JmjC, jumonji C; α-KG, α-ketoglutarate; LSD, lysine-specific demethylase; MATI/IIα, methionine adenosyltransferase I/IIα; SAH, S-adenosyl homocysteine; SAM, S-adenosylmethionine; TDG, thymine DNA glycosylase; TET, ten eleven translocation DNA demethylase.

Figure 1-4: Reversible Chromatin Methylation Reaction Diagrams and SAM Metabolism Schematic.

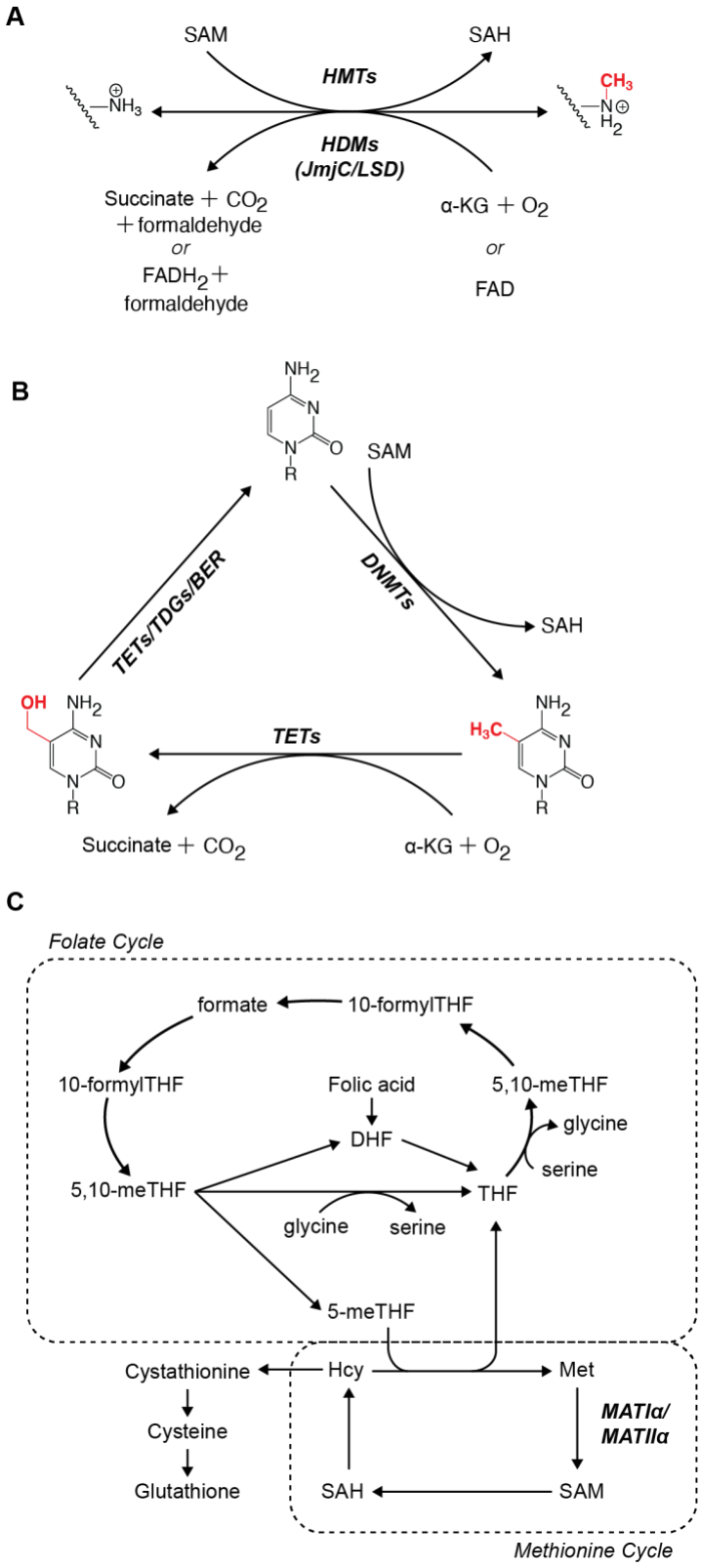

1.3.5 DNA Methylation

In addition to histones, individual DNA bases can be methylated. Methylation of cytosine at carbon 5 (5mC) is the most common and well-studied form of DNA methylation, typically occurring at CpG dinucleotides (Figure 1-4B). In mammals, these reactions are primarily catalyzed by DNA methyltransferases 3A and 3B (DNMT3A/B) at gene promoters, in the bodies of actively transcribed genes, and at repetitive DNA elements [68]. This review will focus on the links between metabolism and 5mC in gene promoters and regulatory elements. For more information on 5mC in gene bodies and at repetitive regions, please see the review by Greenberg and Bourc'his [68].

In promoters, 5mC is commonly found as part of broader CpG islands, which refer to DNA regions where CpG dinucleotides occur with a higher frequency relative to the rest of the genome [69]. Methylation of promoter CpG islands is normally associated with transcriptional repression. This gene-repressive function for 5mC can prevent transcription factor binding and/or recruitment of other chromatin modifying enzymes that support heterochromatic environments (e.g. H3K9 HMTs and HDACs) [70–76]. Contrary to common perception, 5mC can also facilitate transcriptional activation. However, unlike other epigenetic modifications associated with transcriptionally active genes (e.g. H3K9ac, H3K4me3, etc.), 5mC can act as a de-repressor through displacement of the transcriptional silencing complex PRC2 [77].

Like HMTs, DNMTs require SAM as an essential methyl-donor co-substrate, opening similar avenues for metabolic perturbations to influence 5mC profiles (Figure 1-4C). While mechanistic studies investigating direct links between SAM abundance and 5mC are limited, associations have been made under broader metabolic contexts [78,79]. For example, increased methionine cycle flux and glycine N-methyltransferase (GNMT) activity in the long-lived Ames-

Dwarf mouse correlates with suppressed age-associated methylation at regulatory transcriptional elements [80]. Cole et al hypothesize these effects may be driven by decreased SAM availability, which if correct, would provide a direct link between perturbed methyl-donor metabolism and 5mC profiles.

1.3.6 Histone Demethylation

Histone demethylases (HDMs) are responsible for the active removal of K_{me} from histones. Two classes of HDMs have been defined based on catalytic mechanisms: 1.) lysine-specific demethylase (LSD) and 2.) jumonji C (JmjC) domain-containing demethylases (Figure 1-4A) [81]. LSD demethylases utilize FAD-dependent oxidation of the methylated lysine ε-amine to facilitate methyl-group removal, producing $FADH_2$ [82,83]. As this reaction requires the lysine ε-amine to have a free electron pair, LSD demethylases may only catalyze the removal of mono- or di-methylation. JmjC demethylases initiate lysine and arginine demethylation using an Fe(II) and α-ketoglutarate (α-KG)-dependent dioxygenase mechanism, enabling this class of enzymes to target all forms of K_{me} for demethylation [83].

In addition to acting as histone demethylase substrates, FAD and α-KG support mitochondrial oxidative metabolism. FAD is an electron acceptor for the TCA cycle enzyme succinate dehydrogenase, producing $FADH_2$ which is used by Complex II of the electron transport chain to drive ATP synthesis. In addition to its direct role in supporting energy metabolism, FAD availability has also been shown regulate LSD1 repression of energy expenditure target-genes in 3T3-L1 pre-adipocytes [84]. α-KG is a TCA cycle intermediate that can be generated by the oxidative decarboxylation of isocitrate or through glutamate anaplerosis. Furthermore, the JmjC reaction product succinate, as well as the structurally similar TCA cycle intermediate fumarate, can inhibit JmjC catalysis [85]. As a result, changes in mitochondrial metabolism are capable of directly influencing histone methylation profiles and subsequent gene expression.

1.3.7 DNA Demethylation

DNA methylation, like histone methylation, is a reversible epigenetic modification. Removal of 5mC DNA methylation can occur passively via dilution during DNA replication and/or actively by Fe(II) and α-KG-dependent dioxygenase enzymes. This family of DNA demethylases, known as TETs, catalyze several rounds of 5mC oxidation before thymine DNA glycosylase (TDG) and the base excision repair (BER) pathway replace the base with an unmodified cytosine (Figure 1-4B) [86]. TETs and JmjC demethylases utilize a similar catalytic mechanism and therefore possess the same metabolic dependencies and susceptibilities. For example, in mESCs, glycolysis- and glutamine-dependent intracellular α-KG supports the activities of JmjC and TET demethylases to remove repressive methyl-modifications, driving the expression of pluripotency associated genes [87,88].

1.4 Physiologic States with Altered Chromatin Modifying Cofactors

1.4.1 Overview

Due to the requirement of metabolic cofactors by many chromatin modifying enzymes (as described above), the epigenome is susceptible to perturbations in central metabolism. Such fluctuations in cofactor abundance can occur frequently over an organism's lifespan, stemming from both natural cellular processes (e.g., circadian regulation and aging) as well as external factors (e.g., changing dietary patterns and disease onset). While these fluctuations may not be solely responsible for stimulating changes to the epigenome, there are a number of cases in which some degree of causality can be illustrated. Here, I describe a subset of specific conditions where altered levels of metabolites directly affect epigenetic states.

1.4.2 Circadian Regulation

Circadian rhythm, or the internally regulated 24-hour oscillations of life processes that occur within organisms, can elicit significant changes in metabolite availability. The abundance of nearly 50% of mouse liver metabolites are circadian regulated, with 28% of this subset also being controlled by circadian mechanisms in human cells [89]. These cyclically regulated metabolites include cofactors for chromatin modifying enzymes (e.g. SAM, NAD^+, and FAD), suggesting that the epigenome may be dynamically regulated in tune with circadian rhythms [89]. I propose that this mechanism requires a subset of epigenetic modifications to be sensitive to metabolic fluctuations, while the remaining fraction is largely unaffected (Figure 1-5A, 1-5B). This would enable the epigenome, and subsequent transcriptome, to have metabolic flexibility as needed while critical chromatin functions can continue unperturbed.

For example, oscillating regulation of NAD^+ biosynthesis and availability have been shown to directly influence sensitive sites of K_{acetyl} targeted by the core circadian machinery complex, CLOCK:BMAL1 (Figure 1-5A). The NAD^+ salvage pathway rate-limiting enzyme nicotinamide phosphoribosyltransferase (NAMPT) is regulated in a circadian manner at both the mRNA and protein level, creating similar fluctuations in NAD^+ levels [90,91]. NAD^+ is an essential cofactor for the deacetylase SIRT1, which was reported to antagonize H3K9ac and H3K14ac controlled by CLOCK:BMAL1, as well as BMAL1 acetylation [92,93]. An alternative mechanism by which fluctuating NAD^+ regulates circadian transcription involves SIRT1-dependent deacetylation of PER2, a CLOCK:BMAL1 inhibitor (Figure 1-5A) [94]. Regardless of the mechanism, there is compelling evidence suggesting SIRT1's dependency on intrinsic NAD^+ fluctuations leads to the oscillating repression of circadian-regulated genes.

Figure 1-5: Known and Proposed Effects of NAD^+, FAD, and SAM Availability on Chromatin Structure and Function. Circadian rhythm and dietary intake affect cellular availability of key metabolites that act as cofactors for chromatin modifying enzymes such as NAD^+, FAD, and SAM. (*A*) Fluctuations in NAD^+ levels enable SIRT1-dependent regulation of CLOCK target genes (e.g., NAMPT) through two independent yet nonexclusive mechanisms: (i) histone/ BMAL1 deacetylation and (ii) deacetylation of the CLOCK:BMAL1 negative regulator PER2. (*B*) Changes in SAM and FAD availability have been shown to directly influence chromatin methylation states, although the effect of circadian fluctuations in the abundances of these cofactors is unknown. The literature suggests methyl modifications at certain loci are more sensitive (highlighted in yellow) to altered SAM and FAD availability than other loci (highlighted in blue). This mechanism may allow for dynamic flexibility in chromatin structure and function by enabling cells to adapt to various perturbations, while still supporting critical chromatin functions. Abbreviations: NAMPT, nicotinamide phosphoribosyltransferase; SAM, S-adenosylmethionine; SIRT1, sirtuin 1.

Figure 1-5: Known and Proposed Effects of NAD^+, FAD, and SAM Availability on Chromatin Structure and Function.

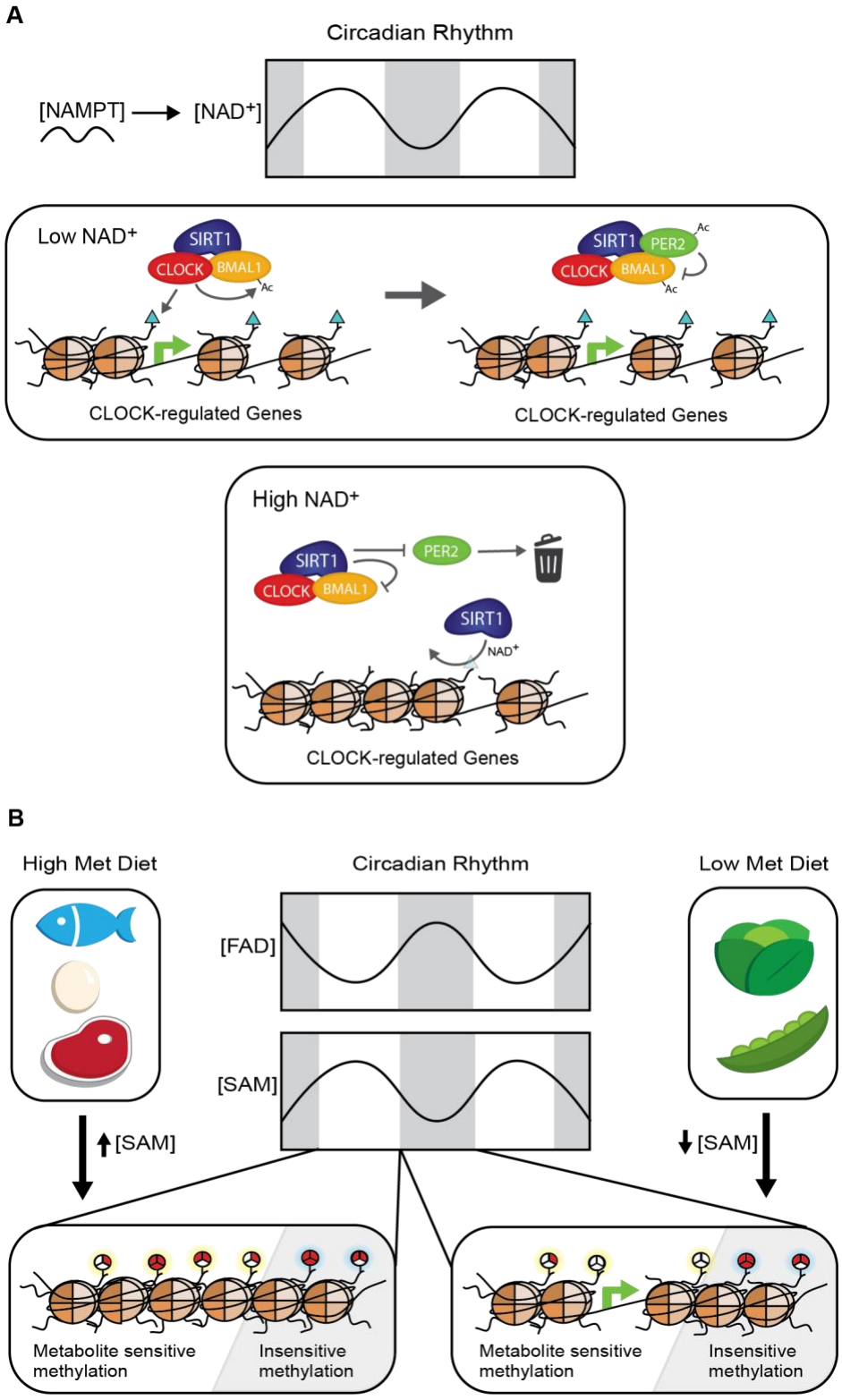

1.4.3 Aging

At the level of chromatin, aging is generally characterized as an increase in transcriptional noise as alterations to the patterns of epigenetic modifications leads to dysregulation of gene expression and chromatin structure [95]. While the mechanisms contributing to the loss of epigenetic information are still unknown, it is hypothesized that dysregulation of metabolic pathways may play a role in exacerbating aging phenotypes.

Acetyl-CoA levels have been shown to increase with age in *Drosophila*, caused by an increase in the activity of the acetyl-CoA-synthesizing enzyme, ATPCL. Rising levels of acetyl-CoA promote significant increases in H4K12ac, H3K9ac, H3K9acK14ac, and H3K23ac, provoking age-associated increases in aberrant gene transcription [96]. Additionally, age-dependent decreases in the histone deacetylase Sir2, the yeast homolog to mammalian SIRT1, and its essential cofactor NAD^+, further support loss of chromatin maintenance. Diminishing HDAC activity leads to global increases in H4K16ac levels, compromising heterochromatin stability in genomic regions such as telomeres, ribosomal DNA (rDNA), and silenced mating type loci [97].

One well-established dietary intervention to delay onset of age-related diseases and extend longevity is caloric restriction (CR), the method of limiting calorie intake without causing malnutrition. Interestingly, recent studies have associated CR with reduced “methylation drift”, a scenario where normally hypermethylated CpG islands become hypomethylated and vise-versa [98]. This loss of specific methylation patterns is a common epigenetic phenotype of aging and correlates with alterations in gene expression [98]. Some of these age-associated changes in CpG methylation are robust enough within mammalian populations that they can be used as predictors of chronological age [99]. In rhesus monkeys, CR by 30% for 7-14 years resulted in a “methylation

age" 7 years younger, on average, when compared to chronologically age-matched controls. In mice, an even more pronounced phenotype was observed in animals fed a 40% caloric restrictive diet, where on average, mice displayed a methylation age of 0.8 years compared to their actual chronological age of 2.8 years [98]. Although such alterations to DNA methylation have not been shown to be causal in slowing aging, the ability of CR to counteract aging and age-related diseases could be mediated at the epigenetic level through the alterations in epi-metabolites discussed in this review. In more general terms, it is plausible that the metabolic reprogramming of transcriptional states associated with CR is driven by chronic alterations in epi-metabolites, hormetic responses, and signaling pathways that sense and transmit metabolic restriction to chromatin.

1.4.4 Cancer

Reprogrammed energy metabolism is a trademark of tumor cells, highlighted by the presence of the Warburg effect. A hypothesized benefit of the Warburg effect is increased availability of glycolysis intermediates that can be shunted into various biosynthesis pathways that produce macromolecules required for proliferation and growth [100]. A secondary consequence of the Warburg effect is elevated intracellular concentrations of acetyl-CoA, providing a direct link between altered cancer metabolism and the epigenome [101].

In fact, alteration of histone acetylation patterns is a hallmark of many solid tumors. In cooperation with increased glycolytic flux, oncogenic AKT has been shown to drive increases in acetyl-CoA levels through phosphorylation and activation of ACLY. This AKT-dependent rise in acetyl-CoA is sufficient to increase global histone acetylation levels [102]. The citrate used by ACLY is supplied by increased glycolytic flux, highlighting the cooperativity of these oncogenic mechanisms [101]. More studies are needed to determine if ACLY-dependent hyperacetylation might promote cancer pathology through specific transcriptional states or through a more general mechanism involving global changes to chromatin and increased genomic instability.

In addition to histone acetylation, altered cancer metabolism is directly linked to changes in histone and DNA methylation abundance as well. Mutations in isocitrate dehydrogenase genes *IDH1* and *IDH2* (commonly found in gliomas, melanomas, and acute myeloid leukemias) encode a mutant enzyme that catalyzes the reduction of α-KG to 2-hydroxyglutarate (2-HG) [103]. 2-HG functions as a competitive inhibitor for JmjC and TET demethylases, binding to the same region as α-KG, causing genome wide alterations to histone and DNA methylation patterns. Loss of function mutations to succinate and fumarate dehydrogenase, TCA cycle enzymes downstream of IDH, are also associated with various cancers. Such mutations result in the accumulation of

succinate and fumarate, respectively, which are capable of inhibiting JmjC and TET demethylases through a similar mechanism as 2-HG [85,104,105]. Together, these metabolite-induced changes in epigenetic methylation status are believed to block differentiation and promote tumorigenesis, emphasizing the detrimental effects that oncometabolites, produced through altered cancer metabolism, can have on the epigenome.

1.4.5 Dietary Alterations

Many metabolic pathways depend on dietary intake of essential amino acids (EAAs) as organisms lack the ability for endogenous synthesis. EAAs are often precursors to cofactors used by chromatin modifying enzymes (Figure 1-1, Table 1-1), showcasing a potential regulatory link between diet and the epigenome. For instance, foods such as eggs, poultry, red-meat, and fish contain high levels of methionine, the obligatory precursor of the methyl-donor cofactor SAM. Consumption of plant-based diets that avoid such foods correlate with significantly lower plasma methionine levels, among other amino acids, which may impact an organism's methylation capacity (Figure 1-5B) [106]. While the relationship between dietary methionine restriction, as well as that of other EAAs, and the epigenome is documented, the phenotypes elicited by these diets are typically positive [64,107–109]. From a chromatin perspective this appears counterintuitive as the literature implies decreased availability of essential metabolic precursors and cofactors would result in dysregulation of the epigenome, promoting negative pathologies. Interestingly, data presented in Chapter 2 demonstrate cells/organisms possess the ability to adaptively regulate and preserve critical chromatin regions during fluctuations in methyl-metabolite availability [67]. These findings suggest fluctuations in the abundance of other EAAs or essential metabolic cofactor may stimulate similar responses, proposing a general mechanism by which regulation of essential genomic loci can be preserved during severe metabolic perturbations.

In addition to EAA restricted diets, high energy diets (high fat and simple sugars) can also impact the epigenome. Keleher et al. showed such diets stimulate altered DNA methylation profiles in SM/J mouse liver [110]. Interestingly, type 2 diabetes mellitus (T2DM), a common pathophysiological consequence of chronic high energy diet intake, is associated with altered DNA

methylation profiles in pancreatic β-cells as well. These changes include hypermethylation of promoters for genes which regulate cellular metabolism and β-cell function, correlating with glycolated hemoglobin A1c (HbA1c) plasma levels, a long-term readout of plasma glucose concentrations [111]. While the mechanisms that outline how high energy diet/T2DM alter DNA methylation require further investigation, these collections of studies highlight how metabolic perturbations are capable of affecting the epigenome.

1.5 Prospective

Susceptibility of the epigenome to altered metabolic cofactor availability provides a direct path for metabolism to regulate a cell's and/or organism's transcriptional environment. This allows chromatin to act as a signal integrator of diverse metabolic pathways, like those described here, to regulate both canonical (e.g. acetylation and methylation) and emerging (e.g. acylation, ADP-ribosylation, O-GlcNAcylation, and lactylation, etc.) epigenetic modifications [112–114]. Numerous studies have provided evidence in support of this general model, yet it remains largely unclear why certain regions of the epigenome are more or less susceptible to metabolic perturbations than others (see 1.6 Outstanding Questions). Recent insights into the capabilities of loci-specific regulation of the epigenome by metabolic enzymes introduces potential mechanisms for more directed regulation of chromatin modifications during fluctuations in cofactor availability. However, these metabolic enzymes cannot act in isolation as the PTMs they support will require coordinated regulation of relevant chromatin effectors to facilitate a functional transcriptional response. Broad experimental approaches (i.e., biochemical, genetic, physiological, etc.) will be needed to uncover such complex mechanisms as the metabolism-epigenome relationship paradigm continues to shift, opening exciting opportunities for the field moving forward.

1.6 Outstanding Questions Regarding Metabolism-Chromatin Relationships

I. Why are PTMs at certain genomic loci more susceptible to fluctuations in epigenetic cofactor availability than others?

II. Do adaptive mechanisms maintain regulation of critical chromatin regions during physiologic fluctuations in cofactor availability?

III. How do metabolic enzymes support loci-specific regulation of gene expression?

IV. What signal(s) determine whether metabolism-induced changes to the epigenome revert upon metabolic recovery or are instead retained permanently?

V. What are the functional consequences of altered epigenetic profiles during natural or induced fluctuations in epigenetic cofactor availability?

VI. How much does tissue and/or cell-type-specific expression of chromatin modifying enzymes impact the metabolic sensitivity of a cell's epigenome?

1.7 Acknowledgements

This work was supported through grants from the NIH (S.A.H. –T32 DK007665 and J.M.D. and C.M.L.– R37 GM059785). We apologize to our colleagues whose work was unable to be cited given strict limitations in reference number.

1.8 References

1. Sabari, B.R. et al. (2017) Metabolic regulation of gene expression through histone acylations. Nat. Rev. Mol. Cell Biol. 18, 90–101.
2. Zhang, R. et al. (2017) Histone Acetylation Regulates Chromatin Accessibility: Role of H4K16 in Inter-nucleosome Interaction. Biophys. J. 112, 450–459.
3. Copur, Ö. et al. (2018) Sex-specific phenotypes of histone H4 point mutants establish dosage compensation as the critical function of H4K16 acetylation in Drosophila. Proc. Natl. Acad. Sci. U.S.A. 115, 13336–13341.
4. Johnson, L.M. (1990) Genetic evidence for an interaction between SIR3 and histone H4 in the repression of the silent mating loci in Saccharomyces cerevisiae. Proc. Natl. Acad. Sci. U.S.A. 87, 6286–6290.
5. Park, E.C. and Szostak, J.W. (1990) Point mutations in the yeast histone H4 gene prevent silencing of the silent mating type locus HML. Mol Cell. Bio. 10, 4932–4934.
6. Fujisawa, T. and Filippakopoulos, P. (2017) Functions of bromodomain-containing proteins and their roles in homeostasis and cancer. Nat. Rev. Mol. Cell Biol 18, 246–262.
7. Gates, L.A. et al. (2017) Acetylation on histone H3 lysine 9 mediates a switch from transcription initiation to elongation. J. Biol. Chem. 292, 14456–14472.
8. Zhao, D. et al. (2017) YEATS Domain—A Histone Acylation Reader in Health and Disease. J. Mol. Bio. 429, 1994–2002.
9. Fan, J. et al. (2015) Metabolic regulation of histone post-translational modifications. ACS Chem. Biol. 10, 95–108.
10. Sivanand, S. et al. (2017) Nuclear Acetyl-CoA Production by ACLY Promotes Homologous Recombination. Mol. Cell. 67, 252-265.

11. Sivanand, S. et al. (2018) Spatiotemporal Control of Acetyl-CoA Metabolism in Chromatin Regulation. Trends Biochem. Sci. 43, 61–74.
12. Sutendra, G. et al. (2014) A Nuclear Pyruvate Dehydrogenase Complex Is Important for the Generation of Acetyl-CoA and Histone Acetylation. Cell. 158, 84–97.
13. Mews, P. et al. (2017) Acetyl-CoA synthetase regulates histone acetylation and hippocampal memory. Nature. 546, 381–386.
14. Wellen, K.E. et al. (2009) ATP-Citrate Lyase Links Cellular Metabolism to Histone Acetylation. Science. 324, 1076–1080.
15. Mews, P. et al. (2019) Alcohol metabolism contributes to brain histone acetylation. Nature. 574, 717–721.
16. Huang, H. et al. (2018) Lysine benzoylation is a histone mark regulated by SIRT2. Nat Commun. DOI: 10.1038/s41467-018-05567-w .
17. Simithy, J. et al. (2017) Characterization of histone acylations links chromatin modifications with metabolism. Nat Commun. DOI: 10.1038/s41467-017-01384-9.
18. Chen, Y. et al. (2007) Lysine Propionylation and Butyrylation Are Novel Post-translational Modifications in Histones. Mol. Cell. Proteomics. 6, 812–819.
19. Tan, M. et al. (2011) Identification of 67 Histone Marks and Histone Lysine Crotonylation as a New Type of Histone Modification. Cell. 146, 1016–1028.
20. Xie, Z. et al. (2016) Metabolic Regulation of Gene Expression by Histone Lysine β-Hydroxybutyrylation. Mol. Cell. 62, 194–206.
21. Dai, L. et al. (2014) Lysine 2-hydroxyisobutyrylation is a widely distributed active histone mark. Nat. Chem. Biol. 10, 365–370.

22. Xie, Z. et al. (2012) Lysine Succinylation and Lysine Malonylation in Histones. Mol. Cell. Proteomics. 11, 100–107.

23. Bao, X. et al. (2019) Glutarylation of Histone H4 Lysine 91 Regulates Chromatin Dynamics. Mol. Cell. 76, 660-675.

24. Wagner, G.R. et al. (2017) A Class of Reactive Acyl-CoA Species Reveals the Non-enzymatic Origins of Protein Acylation. Cell Metab. 25, 823-837.

25. Trub, A.G. and Hirschey, M.D. (2018) Reactive Acyl-CoA Species Modify Proteins and Induce Carbon Stress. Trends Biochem. Sci. 43, 369–379.

26. Li, Y. et al. (2016) Molecular Coupling of Histone Crotonylation and Active Transcription by AF9 YEATS Domain. Mol. Cel.l 62, 181–193.

27. Zhang, Q. et al. (2016) Structural Insights into Histone Crotonyl-Lysine Recognition by the AF9 YEATS Domain. Structure. 24, 1606–1612.

28. Wang, Y. et al. (2018) Identification of the YEATS domain of GAS41 as a pH-dependent reader of histone succinylation. Proc. Natl. Acad. Sci. U.S.A. 115, 2365–2370.

29. Klein, B.J. et al. (2019) Histone H3K23-specific acetylation by MORF is coupled to H3K14 acylation. Nat. Commun. DOI: 10.1038/s41467-019-12551-5.

30. Andrews, F.H. et al. (2016) The Taf14 YEATS domain is a reader of histone crotonylation. Nat. Chem. Biol. 12, 396–398.

31. Gowans, G.J. et al. (2019) Recognition of Histone Crotonylation by Taf14 Links Metabolic State to Gene Expression. Mol. Cell. 76, 909-921.

32. Sabari, B.R. et al. (2017) Intracellular Crotonyl-CoA Stimulates Transcription through p300-Catalyzed Histone Crotonylation. Mol. Cell. 58, 203–215.

33. Kebede, A.F. et al. (2017) Histone propionylation is a mark of active chromatin. Nat. Struct. Mol. Biol. 24, 1048–1056.

34. Feldman, J.L. et al. (2012). Sirtuin Catalysis and Regulation. J. Biol. Chem. 287, 42419–42427.

35. Jing, H. and Lin, H. (2015) Sirtuins in Epigenetic Regulation. Chem. Rev. 115, 2350–2375.

36. Verdin, E. (2015) NAD+ in aging, metabolism, and neurodegeneration. Science. 350, 1208–1213.

37. Revollo, J.R. et al. (2004) The NAD Biosynthesis Pathway Mediated by Nicotinamide Phosphoribosyltransferase Regulates Sir2 Activity in Mammalian Cells. J. Biol. Chem. 279, 50754–50763.

38. Mouchiroud, L. et al. (2013) The NAD+/Sirtuin Pathway Modulates Longevity through Activation of Mitochondrial UPR and FOXO Signaling. Cell. 154, 430–441.

39. Belenky, P. et al. (2007) Nicotinamide Riboside Promotes Sir2 Silencing and Extends Lifespan via Nrk and Urh1/Pnp1/Meu1 Pathways to NAD+. Cell. 129, 473–484.

40. Ho, C. et al. (2009) SIRT1 markedly extends replicative lifespan if the NAD+ salvage pathway is enhanced. FEBS Lett. 583, 3081–3085.

41. Brown, K.D. et al. (2014) Activation of SIRT3 by the NAD+ Precursor Nicotinamide Riboside Protects from Noise-Induced Hearing Loss. Cell Metab. 20, 1059–1068.

42. Cheng, Z. et al. (2009) Molecular Characterization of Propionyllysines in Non-histone Proteins. Mol. Cell. Proteomics. 8, 45–52.

43. Smith, B.C. and Denu, J.M. (2007) Acetyl-lysine Analog Peptides as Mechanistic Probes of Protein Deacetylases. J. Biol. Chem. 282, 37256–37265.

44. Feldman, J.L. et al. (2013) Activation of the Protein Deacetylase SIRT6 by Long-chain Fatty Acids and Widespread Deacylation by Mammalian Sirtuins. J. Biol. Chem. 288, 31350–31356.

45. Klein, M.A. et al. (2020) Mechanism of activation for the sirtuin 6 protein deacylase. J. Biol. Chem. 295, 1385–1399.

46. Rahnasto-Rilla, M. et al. (2018) Natural polyphenols as sirtuin 6 modulators. Sci. Rep. DOI: 10.1038/s41598-018-22388-5.

47. Hubbard, B.P. and Sinclair, D. A. (2014) Small molecule SIRT1 activators for the treatment of aging and age-related diseases. Trends Pharmacol. Sci. 35, 146–154.

48. Najt, C.P. et al. (2020) Lipid Droplet-Derived Monounsaturated Fatty Acids Traffic via PLIN5 to Allosterically Activate SIRT1. Mol. Cell. 77, 810-824.

49. Qin, Y. and Wade, P.A. (2018) Crosstalk between the microbiome and epigenome: messages from bugs. J. Biochem. 163, 105–112.

50. Sekhavat, A. et al. (2007) Competitive inhibition of histone deacetylase activity by trichostatin A and butyrate. Biochem. Cell Biol. 85, 751–758.

51. Waldecker, M. et al. (2008) Inhibition of histone-deacetylase activity by short-chain fatty acids and some polyphenol metabolites formed in the colon. J. Nutr. Biochem. 19, 587–593.

52. Donohoe, D.R. et al. (2012) The Warburg Effect Dictates the Mechanism of Butyrate-Mediated Histone Acetylation and Cell Proliferation. Mol. Cell. 48, 612–626.

53. den Besten, G. et al. (2013) The role of short-chain fatty acids in the interplay between diet, gut microbiota, and host energy metabolism. J. Lipid Res. 54, 2325–2340.

54. Krautkramer, K.A. et al. (2016) Diet-Microbiota Interactions Mediate Global Epigenetic Programming in Multiple Host Tissues. Mol. Cell 64, 982–992.

55. Guccione, E. and Richard, S. (2019) The regulation, functions and clinical relevance of arginine methylation. Nat. Rev. Mol. Cell. Biol. 20, 642–657.

56. Hyun, K. et al. (2017) Writing, erasing and reading histone lysine methylations. Exp. Mol. Med. DOI: 10.1038/emm.2017.11.

57. Li, H. et al. (2006) Molecular basis for site-specific read-out of histone H3K4me3 by the BPTF PHD finger of NURF. Nature. 442, 91–95.

58. Wysocka, J. et al. (2006) A PHD finger of NURF couples histone H3 lysine 4 trimethylation with chromatin remodelling. Nature. 442, 86–90.

59. Lauberth, S. M. et al. (2013) H3K4me3 Interactions with TAF3 Regulate Preinitiation Complex Assembly and Selective Gene Activation. Cell. 152, 1021–1036.

60. Eissenberg, J.C. and Elgin, S.C.R. (2014) HP1a: A Structural Chromosomal Protein Regulating Transcription. Trends Genet. 30, 103–110.

61. Markham, G.D. and Pajares, M.A. (2009) Structure-function relationships in methionine adenosyltransferases. Cell. Mol. Life Sci. 66, 636–648.

62. Halim, A.B. et al. (1999) Expression and Functional Interaction of the Catalytic and Regulatory Subunits of Human Methionine Adenosyltransferase in Mammalian Cells. J. Biol. Chem. 274, 29720–29725.

63. LeGros, H.L. et al. (2000) Cloning, Expression, and Functional Characterization of the β Regulatory Subunit of Human Methionine Adenosyltransferase (MAT II). J. Biol. Chem. 275, 2359–2366.

64. Sanderson, S.M. et al. (2019) Methionine metabolism in health and cancer: a nexus of diet and precision medicine. Nat. Rev. Cancer. 19, 625–637.

65. Shyh-Chang, N. et al. (2013) Influence of Threonine Metabolism on S-Adenosylmethionine and Histone Methylation. Science. 339, 222–226.

66. Ye, C. et al. (2017) A Metabolic Function for Phospholipid and Histone Methylation. Mol. Cell. 66, 180-193.

67. Haws, S. A. et al. (2020) Methyl-Metabolite Depletion Elicits Adaptive Responses to Support Heterochromatin Stability and Epigenetic Persistence. Mol. Cell. 78, 210-223.

68. Greenberg, M.V.C. and Bourc'his, D. (2019) The diverse roles of DNA methylation in mammalian development and disease. Nat. Rev. Mol. Cell. Biol. 20, 590–607.

69. Deaton, A.M. and Bird, A. (2011) CpG islands and the regulation of transcription. Genes Dev. 25, 1010–1022.

70. Yin, Y. et al. (2017) Impact of cytosine methylation on DNA binding specificities of human transcription factors. Science. 356.

71. Estève, P.O. et al. (2006) Direct interaction between DNMT1 and G9a coordinates DNA and histone methylation during replication. Genes Dev. 20, 3089–3103.

72. Myant, K. et al. (2011) LSH and G9a/GLP complex are required for developmentally programmed DNA methylation. Genome. Res. 21, 83–94.

73. Deplus, R. et al. (2002) Dnmt3L is a transcriptional repressor that recruits histone deacetylase. Nucleic Acids Res. 30, 3831–3838.

74. Fuks, F. et al. (2000) T. DNA methyltransferase Dnmt1 associates with histone deacetylase activity. Nat. Genet. 24, 88–91.

75. Hendrich, B. and Bird, A. (1998) Identification and Characterization of a Family of Mammalian Methyl-CpG Binding Proteins. Mol. Cell. Biol. 18, 6538–6547.

76. Meehan, R.R. et al. (1989) Identification of a mammalian protein that binds specifically to DNA containing methylated CpGs. Cell. 58, 499–507.

77. Holoch, D. and Margueron, R. (2017) Mechanisms Regulating PRC2 Recruitment and Enzymatic Activity. Trends Biochem. Sci. 42, 531–542.

78. Mattocks, D.A. et al. (2017) Short term methionine restriction increases hepatic global DNA methylation in adult but not young male C57BL/6J mice. Exp. Gerontol. DOI: 10.1016/j.exger.2016.12.003.

79. Maddocks, O.D. et al. (2016) Serine Metabolism Supports the Methionine Cycle and DNA/RNA Methylation through De Novo ATP Synthesis in Cancer Cells. Mol. Cell. 61, 210–221.

80. Cole, J.J. et al. (2017) Diverse interventions that extend mouse lifespan suppress shared age-associated epigenetic changes at critical gene regulatory regions. Genome Biol. DOI: 10.1186/s13059-017-1185-3.

81. Kooistra, S.M. and Helin, K. (2012) Molecular mechanisms and potential functions of histone demethylases. Nat. Rev. Mol. Cell. Biol. 13, 297–311.

82. Shi, Y. et al. (2004) Histone Demethylation Mediated by the Nuclear Amine Oxidase Homolog LSD1. Cell. 119, 941–953.

83. Anand, R. and Marmorstein, R. (2007) Structure and Mechanism of Lysine-specific Demethylase Enzymes. J. Biol. Chem. 282, 35425–35429.

84. Hino, S. et al. (2012) FAD-dependent lysine-specific demethylase-1 regulates cellular energy expenditure. Nat. Commun. DOI: 10.1038/ncomms1755.

85. Xiao, M. et al. (2012) Inhibition of α-KG-dependent histone and DNA demethylases by fumarate and succinate that are accumulated in mutations of FH and SDH tumor suppressors. Genes Dev. 26, 1326–1338.

86. Wu, X. and Zhang, Y. (2017) TET-mediated active DNA demethylation: mechanism, function and beyond. Nat. Rev. Genet. 18, 517–534.

87. Carey, B.W. et al. (2015) Intracellular α-ketoglutarate maintains the pluripotency of embryonic stem cells. Nature. 518, 413–416.

88. Hwang, I.Y. et al. (2016) Psat1-Dependent Fluctuations in α-Ketoglutarate Affect the Timing of ESC Differentiation. Cell Metab. 24, 494–501.

89. Krishnaiah, S.Y. et al. (2017) Clock Regulation of Metabolites Reveals Coupling between Transcription and Metabolism. Cell Metab. 25, 961-974.

90. Ramsey, K.M. et al. (2009) Circadian Clock Feedback Cycle Through NAMPT-Mediated NAD+ Biosynthesis. Science. 324, 651–654.

91. Nakahata, Y. et al. (2009) Circadian Control of the NAD+ Salvage Pathway by CLOCK-SIRT1. Science. 324, 654–657.

92. Nakahata, Y. et al. (2008) The NAD+-Dependent Deacetylase SIRT1 Modulates CLOCK-Mediated Chromatin Remodeling and Circadian Control. Cell. 134, 329–340.

93. Doi, M. et al. (2006) Circadian regulator CLOCK is a histone acetyltransferase. Cell. 125, 497–508.

94. Asher, G. et al. (2008) SIRT1 Regulates Circadian Clock Gene Expression through PER2 Deacetylation. Cell. 134, 317–328.

95. Peleg, S. et al. (2016) The Metabolic Impact on Histone Acetylation and Transcription in Ageing. Trends Biochem. Sci. 41, 700–711.

96. Peleg, S. et al. (2016) Life span extension by targeting a link between metabolism and histone acetylation in Drosophila. EMBO Rep. 17, 455–469.

97. Dang, W. et al. (2009) Histone H4 lysine 16 acetylation regulates cellular lifespan. Nature. 459, 802–807.

98. Maegawa, S. et al. (2017) Caloric restriction delays age-related methylation drift. Nat. Commun. DOI: 10.1038/s41467-017-00607-3.

99. Weidner, C.I. et al. (2014) Aging of blood can be tracked by DNA methylation changes at just three CpG sites. Genome Bio. DOI: 10.1186/gb-2014-15-2-r24.

100. Hanahan, D. and Weinberg, R.A. (2011) Hallmarks of cancer: the next generation. Cell. 144, 646–674.

101. Liberti, M.V. and Locasale, J.W. (2018) The Warburg Effect: How Does it Benefit Cancer Cells? Trends Biochem. Sci. 41, 211–218.

102. Lee, J.V. et al. (2014) Akt-dependent metabolic reprogramming regulates tumor cell histone acetylation. Cell Metab. 20, 306–319.

103. Xu, W. et al. (2011) Oncometabolite 2-hydroxyglutarate is a competitive inhibitor of α ketoglutarate-dependent dioxygenases. Cancer Cell. 19, 17–30.

104. Letouzé, E. et al. (2013) SDH Mutations Establish a Hypermethylator Phenotype in Paraganglioma. Cancer Cell. 23, 739–752.

105. Cervera, A.M. et al. (2009) Inhibition of succinate dehydrogenase dysregulates histone modification in mammalian cells. Mol. Cancer. DOI: doi: 10.1186/1476-4598-8-89.

106. Schmidt, J.A. et al. (2016) Plasma concentrations and intakes of amino acids in male meat eaters, fish-eaters, vegetarians and vegans: a cross-sectional analysis in the EPIC-Oxford cohort. Eur. J. Clin. Nutr. 70, 306–312.

107. Son, S.M. et al. (2019) Leucine Signals to mTORC1 via Its Metabolite Acetyl-Coenzyme A. Cell Metab. 29, 192-201.

108. Fontana, L. and Partridge, L. (2015) Promoting Health and Longevity through Diet: From Model Organisms to Humans. Cell. 161, 106–118.

109. Brown-Borg, H.M. (2016) Reduced growth hormone signaling and methionine restriction: interventions that improve metabolic health and extend life span. Ann. N.Y. Acad. Sci. 1363, 40–49.

110. Keleher, M.R. et al. (2018) A high-fat diet alters genome-wide DNA methylation and gene expression in SM/J mice. BMC Genomics. DOI: 10.1186/s12864-018-5327-0.

111. Davegårdh, C. et al. (2018) DNA methylation in the pathogenesis of type 2 diabetes in humans. Mol. Metabolism 14, 12–25.

112. Lüscher, B. et al. (2018) ADP-Ribosylation, a Multifaceted Posttranslational Modification Involved in the Control of Cell Physiology in Health and Disease. Chem. Rev. 118, 1092–1136.

113. Hart, G.W. (2019) Nutrient Regulation of Signaling and Transcription. J. Biol. Chem. 294, 2211–2231.

114. Zhang, D. et al. (2019) Metabolic regulation of gene expression by histone lactylation. Nature. 574, 575–580.

Chapter 2: Methyl-Metabolite Depletion Elicits Adaptive Responses to Support Heterochromatin Stability and Epigenetic Persistence

Spencer A. Haws[1,2], Deyang Yu[3,4,5], Cunqi Ye[6], Coral K. Wille[2], Long C. Nguyen[7], Kimberly A. Krautkramer[1,2], Jay L. Tomasiewicz[3], Shany E. Yang[3,4], Blake R. Miller[3,4], Wallace H. Liu[1,2], Kazuhiko Igarashi[7,8], Rupa Sridharan[2,9], Benjamin P. Tu[6], Vincent L. Cryns[4,5,10], Dudley W. Lamming[3,4,5,10], and John M. Denu[1,2]

[1]Department of Biomolecular Chemistry, SMPH, University of Wisconsin-Madison
[2]Wisconsin Institute for Discovery, University of Wisconsin-Madison
[3]William S. Middleton Memorial Veterans Hospital
[4]Department of Medicine, SMPH, University of Wisconsin-Madison
[5]Molecular & Environmental Toxicology Center, SMPH, University of Wisconsin-Madison
[6]Department of Biochemistry, University of Texas Southwestern Medical Center
[7]Department of Biochemistry, Tohoku University Graduate School of Medicine
[8]Center for Regulatory Epigenome and Diseases, Tohoku University Graduate School of Medicine
[9]Department of Cell and Regenerative Biology, University of Wisconsin-Madison
[10]University of Wisconsin Carbone Cancer Center

*This chapter was published in Molecular Cell. 2020 April 16; 78: 210-223.

2.1 Abstract

S-adenosylmethionine (SAM) is the methyl-donor substrate for DNA and histone methyltransferases that regulate epigenetic states and subsequent gene expression. This metabolism-epigenome link sensitizes chromatin methylation to altered SAM abundance, yet the mechanisms that allow organisms to adapt and protect epigenetic information during life-experienced fluctuations in SAM availability are unknown. We identified a robust response to SAM depletion that is highlighted by preferential cytoplasmic and nuclear mono-methylation of H3 Lys 9 (H3K9) at the expense of broad losses in histone di- and tri-methylation. Under SAM-depleted conditions, H3K9 mono-methylation preserves heterochromatin stability and supports global epigenetic persistence upon metabolic recovery. This unique chromatin response was robust across the mouse lifespan and correlated with improved metabolic health, supporting a significant role for epigenetic adaptation to SAM depletion *in vivo*. Together, these studies provide evidence for an adaptive response that enable epigenetic persistence to metabolic stress.

2.2 Introduction

Metabolism and the epigenome are connected by central metabolites that act as co-substrates for chromatin modifying enzymes, enabling fluctuations in metabolite availability to directly tune a cell's ability to 'write' and 'erase' chromatin post-translational modifications (PTMs) [1,2]. Chromatin methylation has been shown to be particularly susceptible to metabolic perturbations as methyltransferases require a single methyl-donor cofactor, S-adenosylmethionine (SAM) [3,4]. For example, accumulation of SAM in *S. cerevisiae* results in global increases in histone methylation levels while reduced SAM availability has been linked with site-specific losses in histone methylation as well as global depression of DNA methylation in several organisms [5–14].

Intracellular SAM abundance is dependent on the catalysis of its obligatory precursor metabolite, the essential amino acid methionine (Met). Consumption of diets containing low quantities of Met (e.g. vegan diets) have been shown to significantly correlate with decreased plasma Met concentrations [15,16]. This link provides an opportunity for diet to directly influence intracellular SAM availability. Intracellular Met and SAM concentrations have also been shown to fluctuate naturally in tune with circadian rhythms [17]. Therefore, individuals consuming adequate amounts of dietary Met likely experience transient periods of decreased methyl-metabolite availability. It is currently unknown whether adaptive mechanisms exist that allow cells to actively respond to – and recover their functional epigenomes from – such metabolic perturbations. Here, we define the ability of a cell and/or organism to re-establish the epigenome that was present prior to onset of an environmental perturbation or metabolic stress as *epigenetic persistence*.

Adaptive mechanisms that respond to methyl-metabolite depletion may support critical cellular functions under these conditions. Interestingly, dietary Met-restriction is associated with beneficial metabolic reprogramming and lifespan extension in mammals [18–23]. These phenotypes run counter to negative pathologies associated with dysregulated chromatin methylation (e.g., intellectual disability syndromes, cancers, and premature as well as natural aging [24]), suggesting cells possess responsive mechanisms capable of maintaining regulation of site specific and/or global chromatin methylation events during SAM depletion. The goal of this study is to identify and characterize such mechanisms to better understand how organisms adapt and protect their epigenomes in response to fluctuations in central metabolite availability.

Here, we identify a robust, conserved chromatin response to metabolically depleted SAM levels. This response is characterized by broad decreases in higher-state histone methylation (di- and tri-methyl) and simultaneous preferential H3K9 mono-methylation involving newly synthesized and chromatin-bound histone H3. Under extreme conditions of both reduced SAM levels and inhibited H3K9 mono-methylation, heterochromatin instability and de-repression of constitutively silenced DNA elements are exacerbated. Acute inhibition of H3K9 mono-methylation also leads to the dysregulation of global histone PTM states upon metabolic recovery, disrupting epigenetic persistence to decreased SAM availability. Importantly, chronic metabolic depletion of SAM in both young and old mice recapitulates these *in vitro* findings, revealing a conserved, age-independent chromatin response. These results implicate adaptive H3K9 mono-methylation as an indispensable mechanism to support heterochromatin stability and global epigenetic persistence in response to SAM depletion.

2.3 Results

2.3.1 Methionine Restriction Stimulates Global, Dynamic Histone PTM Response

To comprehensively investigate how disruption of methyl-donor metabolism affects chromatin methylation states, global histone proteomics and DNA methylation (5mC) analyses were performed on two distinct *in vitro* and *in vivo* systems. These included Met-restricted HCT116 human colorectal cancer cells and C57BL/6J mouse liver. Methionine metabolism was severely repressed in both systems, highlighted by significant reductions in Met and SAM abundance (Figure 2-1A, 2-2A through 2-2D). Reduced methyl-metabolite availability did not affect global DNA 5mC abundance in either system (Figure 2-1B, 2-1C). However, LC-MS/MS analysis of more than 40 unique histone H3 peptide proteoforms revealed dynamic PTM responses to Met-restriction in both HCT116 cells and C57BL/6J liver (Figure 2-1D, 2-1E). In HCT116 cells, Met-restriction stimulated distinct biphasic changes in global PTM profiles (Figure 2-1D). Phase I (0 hr-45 min) was rapid and marked by a trending upregulation of H3K4me2/3, PTMs known to mark transcriptionally active promoters. Phase II (90 min-24 hrs) was characterized by broad decreases in di- and tri- histone methylation. Decreased levels of di- and tri-methylated peptides were accompanied by increases in acetylated and unmodified peptide species. Similarly, in C57BL/6J mice, histone PTM responses were marked by significant decreases in histone di- and tri-methylation that essentially matched the patterns found in HCT116 cells during the prolonged Phase II response (Figure 2-1E, 2-3E through 2-3J). Decreased higher-state (di- and tri-) histone methylation both *in vitro* and *in vivo* highlight a decreased methylation capacity resulting from prolonged Met and/or SAM depletion. Together, these observations suggest histone methylation is more dynamically regulated by methyl-metabolite availability than global 5mC DNA methylation. Furthermore, similarities between the

metabolic and epigenetic responses to Met-restriction across both systems support the use of *in vitro* Met-restriction as a model for mechanistic follow-up studies.

Figure 2-1: Methionine (Met) Restriction Stimulates Global, Dynamic Histone PTM Response. (*A*) Metabolic pathway diagram illustrating changes in Met-cycle metabolite abundance after 24 h and 5 weeks of Met restriction in HCT116 cells and C57BL/6J liver, respectively. n = 5; error bars represent SD; *p < 0.05 (Welch's t-Test). (*B* and *C*) Plots illustrating global, relative 5mC DNA methylation levels during Met restriction in HCT116 cells and C57BL/6J liver, respectively. n ≥ 3; error bars represent SD, *p < 0.05 (Welch's t test). (*D* and *E*) Hierarchical clustered heatmaps of LC-MS/MS-generated $\log_2$ fold-change stoichiometric histone H3 peptide proteoform values relative to 0 h or chow diet controls in HCT116 cells and C57BL/6J liver, respectively. n ≥ 3; *p < 0.05, **p < 0.01 (Welch's t test).

Figure 2-1: Methionine (Met) Restriction Stimulates Global, Dynamic Histone PTM Response.

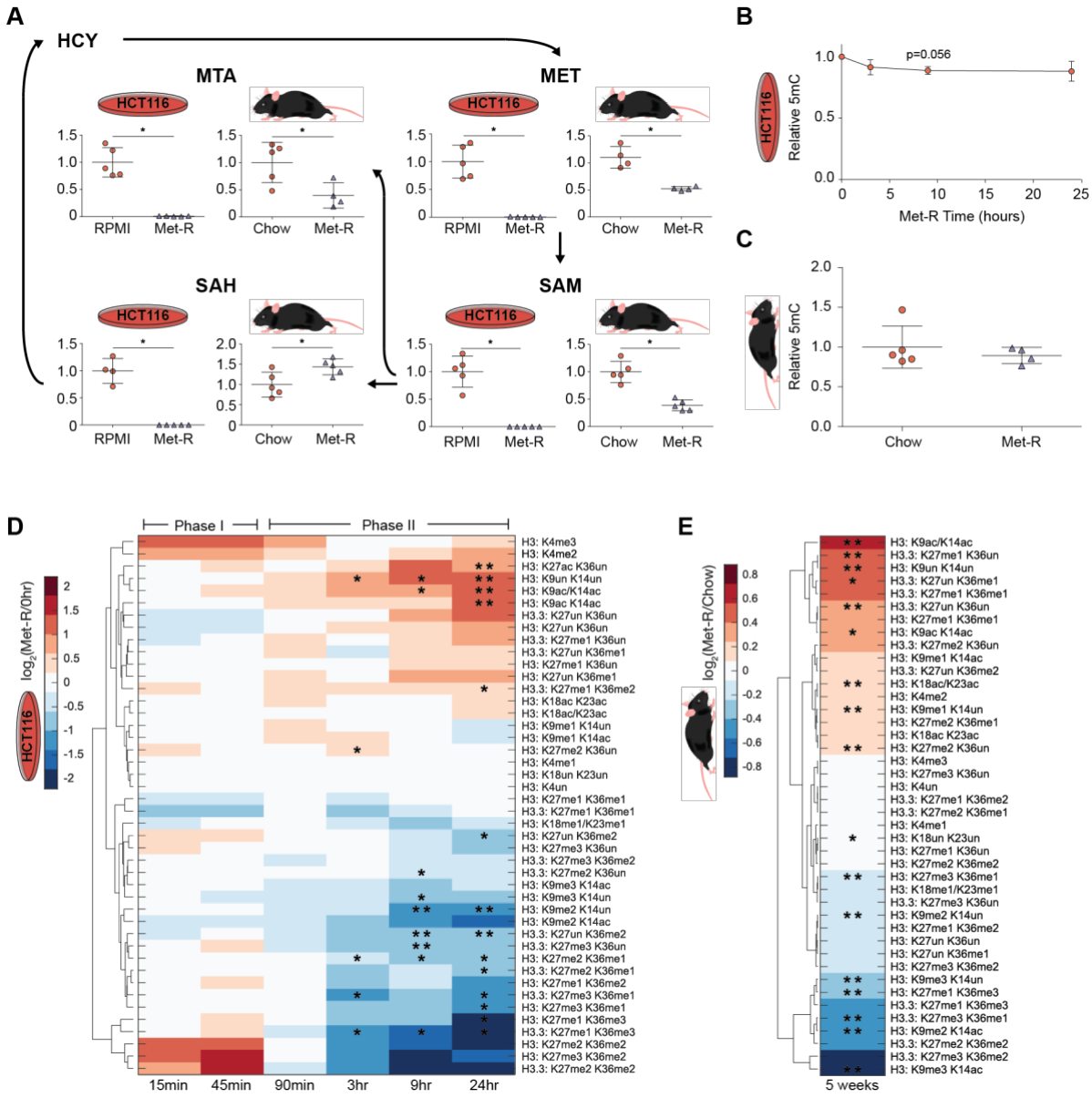

Figure 2-2: Supporting Data Related to Figure 2-1. (*A-D*) Scatter plots of relative abundance values for key Met-cycle metabolites in HCT116 cells as measured by LC-MS. n=5, error bars represent SD, *p<0.05 (Welch's t-Test). (*E-J*) Correlation plots of LC-MS/MS generated $\log_2$ fold-change stoichiometric values for individual histone H3 peptide proteoforms. n ≥ 3.

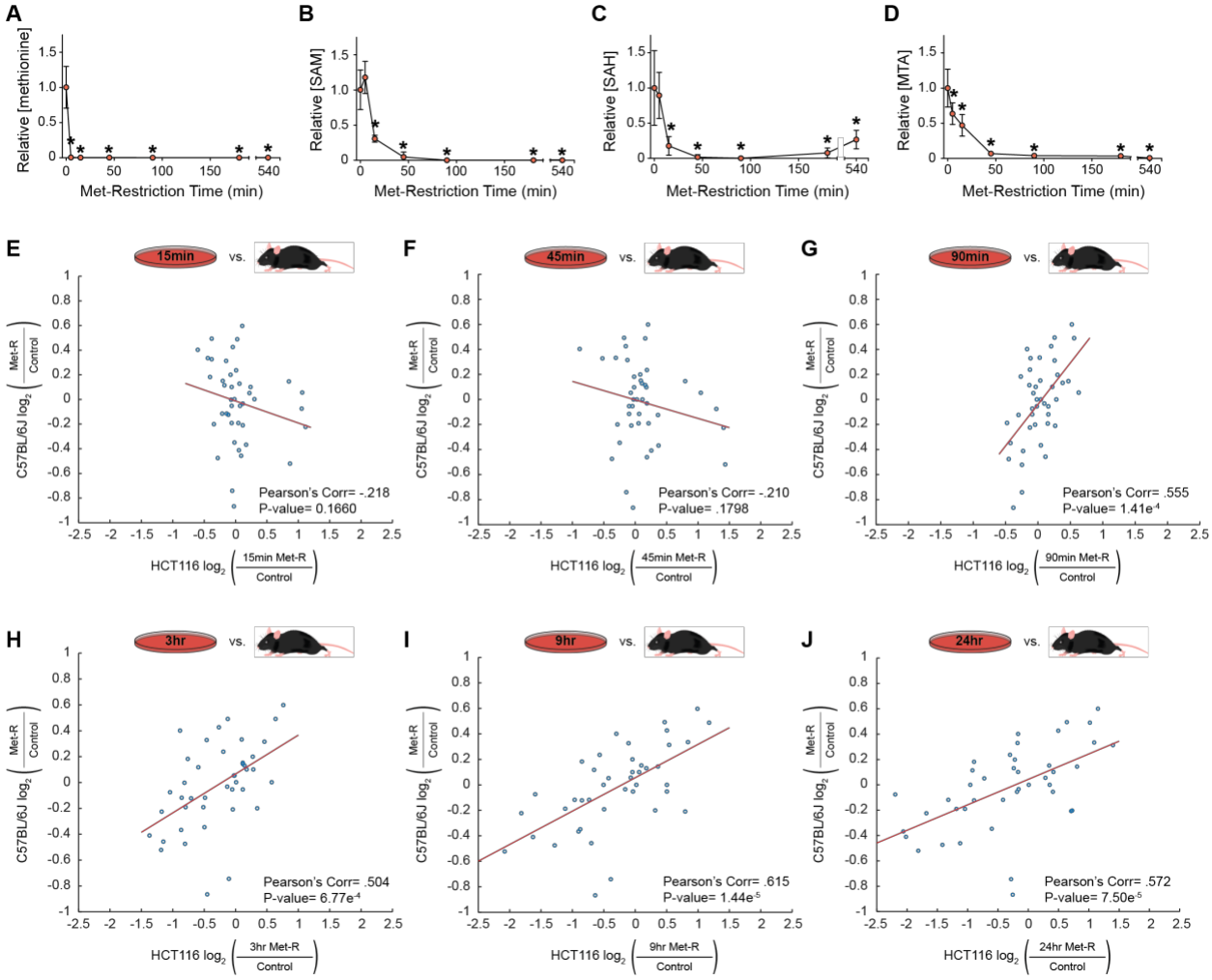

2.3.2 SAM Availability Drives a Robust Histone Methylation Response

Dramatic reduction of intracellular Met and SAM correlated with onset of the *in vitro* Phase I and II histone PTM changes, respectively (Figure 2-1D, 2-2A, 2-2B). This implies depletion of individual methyl-metabolites may be capable of stimulating distinct histone modifying pathways. To determine if the global losses in di- and tri- histone methylation *in vitro* are driven specifically by SAM depletion, two alternative approaches were employed to deplete cellular SAM independent of Met (Figure 2-3A). The first approach utilized RNAi knockdown of the mammalian SAM synthetase MATIIα (methionine adenosyltransferase II alpha). Knockdown via MATIIα-RNAi treatment decreased MATIIα transcript abundance by greater than 97%, resulting in a near complete deprivation of SAM availability with no effect on Met levels (Figure 2-3B through 2-3D). Histone proteomics analysis of MATIIα-RNAi treated cells identified site-specific histone PTM changes that mirrored those identified in HCT116 cells under Phase II Met-restriction conditions ($r=0.778$, $p=8.59e^{-10}$) (Figure 2-3E). Using a complementary approach, SAM levels were depleted by overexpression of a major SAM consumer, PEMT (phosphatidylethanolamine N-methyltransferase). Ye et al., 2017 have previously shown PEMT overexpression significantly reduces SAM availability in HEK293T human embryonic kidney cells. Histone proteomics analysis of PEMT overexpressing HEK293T cells identified site-specific PTM changes that paralleled those of Met-restricted controls ($r=0.803$, $p=3.30e^{-8}$) (Figure 2-3F). Together, two separate means of reducing SAM levels demonstrate SAM reduction alone is sufficient to inhibit the methylation capacity of a cell and induce subsequent changes in histone PTM abundance. Furthermore, these findings support the use of prolonged Met-restriction as a model of SAM depletion.

The similar changes in global histone PTM abundance across four SAM depletion systems were analyzed for the presence of methyl PTMs whose abundances either increased or were unaffected by this metabolic perturbation. Such PTMs would be candidate mediators of an adaptive response to SAM depletion. Unexpectedly, all four SAM depletion systems exhibited identical changes in H3K9 methylation (Figure 2-3G through 2-3J). SAM depletion stimulated a decrease in H3K9me2/3 with a corresponding increase in H3K9ac/14ac and unmodified peptides while net H3K9me1 abundance was unchanged. Preservation of net H3K9me1 levels in response to SAM depletion was reproducible in Met-restricted MCF7, HEK-293, Panc1, and HepG2 cell lines, as well as in MATIIα-RNAi treated HepA1 cells (Figure 2-4A through 2-4F). Therefore, in diverse systems marked by reduced methylation capacity, a robust and consistent maintenance of net H3K9me1 levels suggest adaptive epigenetic mechanisms may support the abundance of this PTM.

Figure 2-3: SAM Availability Drives Robust Histone Methylation Response. (*A*) Pathway diagram illustrating experimental approaches to depleting intracellular SAM availability. (*B*) Bar graph of relative MATIIα mRNA abundance in HCT116 cells as measured by qRT-PCR. n ≥ 2; error bars represent SD; *p < 0.05 (Welch's t test). (*C* and *D*) Dot plots of relative Met (*C*) and SAM (*D*) levels in HCT116 cells. n ≥ 4; *p < 0.05 (Welch's t test). (*E* and *F*) Correlation plot of LC-MS/MS-generated $\log_2$ fold-change stoichiometric values for individual histone H3 peptide proteoforms. n = 3. (*G*–*J*) Bar graphs illustrating LC-MS/MS-generated $\log_2$ fold-changes for individual H3K9 PTMs. n ≥ 2; *p < 0.05 (Welch's t test).

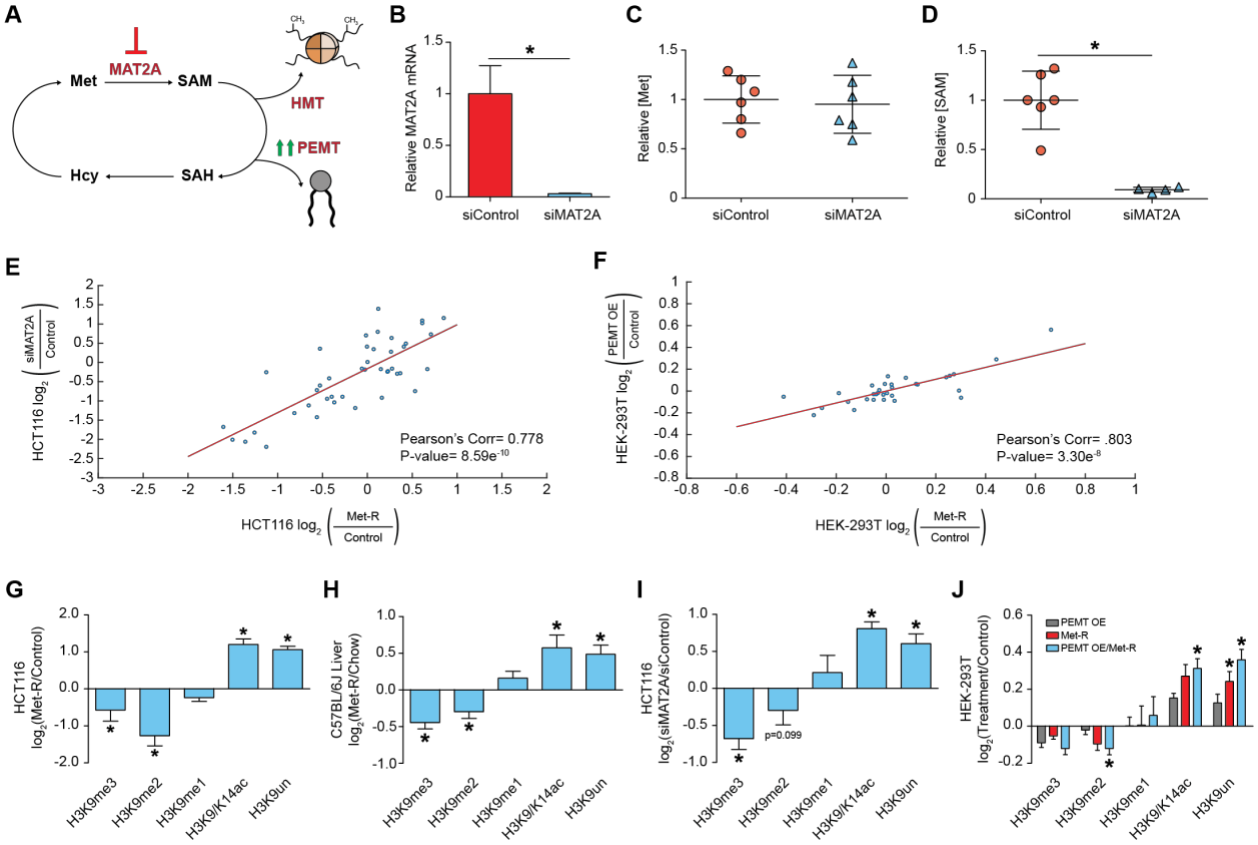

Figure 2-4: Supporting Data Related to Figure 2-3. (*A*) Diagram illustrating the experimental design for determining the conservation of H3K9 regulation in response to SAM depletion across various biological systems. (*B-F*) Bar graphs illustrating log_2 fold-changes for individual H3K9 in response to in vitro SAM depletion. n=3, error bars represent SD, *p<0.05 (Welch's t-Test).

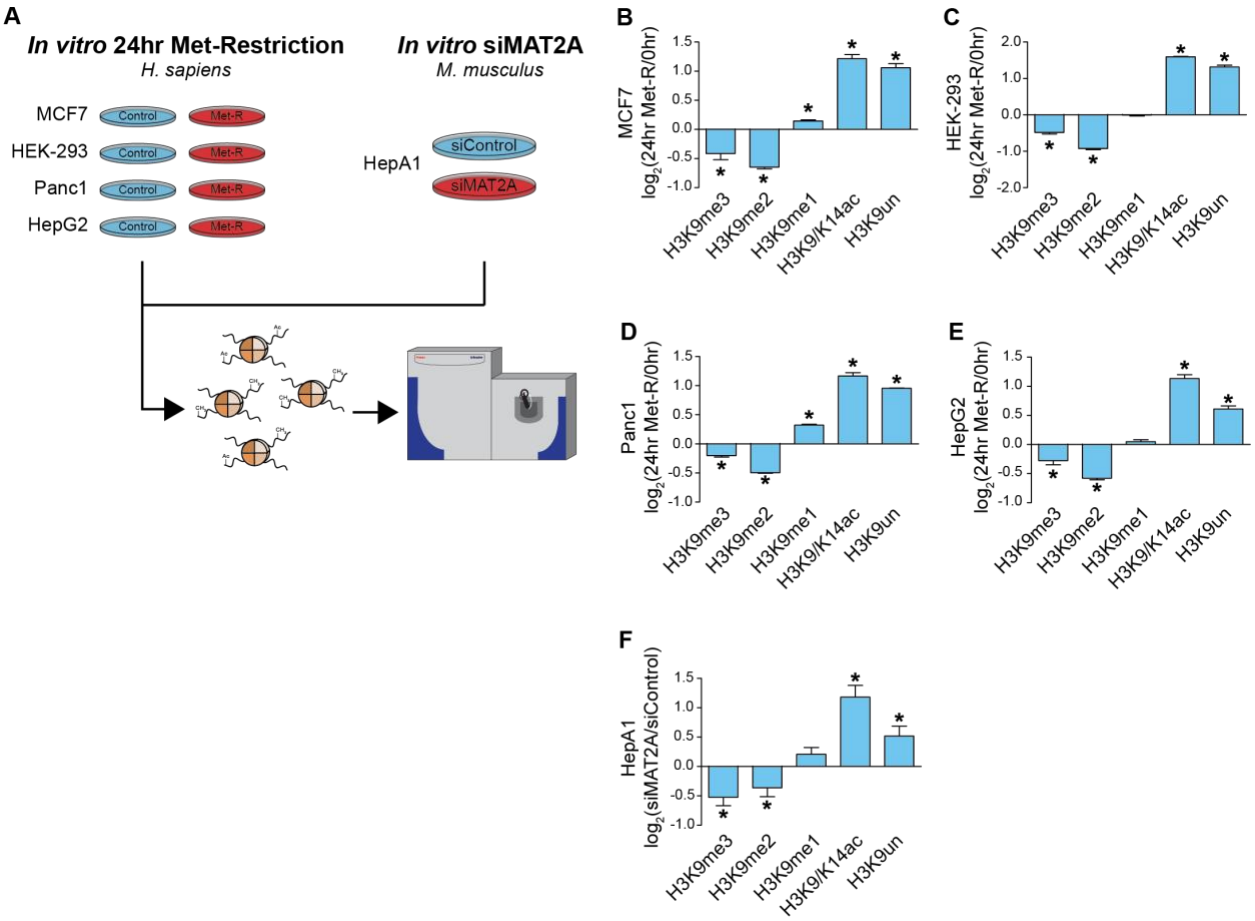

2.3.3 Preferential Methylation Supports Global H3K9me1 under SAM Depletion

Global levels of H3K9me1 could be maintained through three distinct mechanisms during SAM depletion: *1.)* protection from PTM turnover, *2.)* de-methylation of H3K9me2/3, and/or *3.)* methylation of unmodified H3K9. The decrease in H3K9me2/3 and increase in unmodified H3K9 peptide levels across SAM depletion systems suggest H3K9 is subjected to demethylation while new methylation events appear enzymatically unfavorable. However, preferential H3K9 mono-methylation activity could constitute an adaptive response to this metabolic stress that is capable of supporting critical chromatin functions.

To investigate the contribution of HMT activity to global H3K9me1 levels, RNAi-mediated repression of five H3K9 HMTs was performed in Met-replete conditions to determine which enzymes catalyzed a majority of H3K9 mono-methylation reactions in HCT116 cells. Repression of HMT expression had significant yet restricted effects, given technical limitations, on H3K9 PTM abundance and suggested EHMT1/EHMT2 were the primary H3K9 mono-methyltransferases in this system (Figure 2-6A through 2-6D). Because repression of HMT expression was intended to be coupled with Met-restriction, RNAi treatment could not be extended to elicit larger changes in PTM abundance as HCT116 cells no longer proliferate beyond 24 hours of Met-restriction (Figure 2-6E). Therefore, small molecule (UNC0642) inhibition of H3K9 HMTs EHMT1/EHMT2 was used as the best approach to acutely block nuclear H3K9 mono-methylation [25]. UNC0642 treatment of Met-replete cells reduced H3K9me1 abundance to a greater extent than RNAi repression of EHMT1/EHMT2 (Figure 2-5A, 2-6D). Coupling UNC0642 treatment with Met-restriction also stimulated a significant decrease in H3K9me1 levels (Figure 2-5B, 2-6F). Comparatively, these data suggest EHMT1/EHMT2 retain nearly 60% of their H3K9 mono-methylation activity during severe *in*

situ SAM deprivation and that this activity is critical for preserving global H3K9me1 abundance (Figure 2-5C). Furthermore, H3K9me2 abundance decreased significantly in Met-replete cells upon UNC0642 treatment but was unaffected when UNC0642 was coupled with Met-restriction (Figure 2-5A, 2-5B). This indicates only the mono-methylation activity of EHMT1 and EHMT2 is preferentially supported during SAM depletion.

In addition to methylation of H3K9 by nuclear enzymes, mono-methylation is known to be enzymatically added on cytoplasmic histones prior to nuclear import and deposition onto chromatin [26,27]. Subcellular fractionation of Met-restricted HCT116 cells coupled with western blot analyses indicated that cytoplasmic H3K9me1 levels increase 3-fold after 24 hours of Met-restriction, with a similar increase in total H3 protein levels (Figure 2-5D, 2-5E). To determine the contribution of cytoplasmic H3K9me1 to the chromatin-bound nuclear pool after 24 hours of Met-restriction, a pulse-chase, SILAC experiment was performed (Figure 2-5F). L-Arg^{+10} isotope incorporation prior to Met-restriction was nearly complete with average incorporation for H3K9 peptides greater than 98% (Figure 2-6H). After 24 hours of Met-restriction, newly synthesized H3 was calculated to comprise 24% of the chromatin bound histone pool and contributed 18% of the global H3K9me1 signal (Figure 2-5G, 2-5H). UNC0642 treatment did not significantly lessen the contribution of cytoplasmic H3K9me1 to the total pool, suggesting cytoplasmic H3K9me1 may be largely protected from enzyme catalyzed turnover once deposited onto chromatin under these conditions (Figure 2-5G). Modest, insignificant decreases in L-Arg^{+0} H3K9me1 signal after UNC0642 treatment can be attributed to a slower cell growth rate and subsequent reduction in the incorporation of newly synthesized H3 onto chromatin (Figure 2-5G, 2-6E, 2-6I). Together, these results suggest ~40% of global H3K9me1 abundance is driven by preferential activity of H3K9 mono-methyltransferases during Met-

restriction with nearly equal contributions from both the cytoplasm and nucleus. The remaining ~60% of H3K9me1 levels are likely protected from turnover and/or are generated via H3K9me2/3 de-methylation during SAM depletion (Figure 2-5I).

The significant upregulation of cytoplasmic H3K9me1 and total H3, coupled with their incorporation onto chromatin during SAM depletion, were unexpected. These findings suggest cells adapt to this metabolic stress by utilizing scarcely available Met and SAM to support increased histone abundance and H3K9 methylation. Shotgun proteomics was performed on cytoplasmic protein fractions of the previously described SILAC experiment to determine if histone protein abundance is uniquely responsive to SAM depletion. Of the more than 2,400 identified proteins, only 8 possessed significant incorporation of the light L-Arg^{+0} isotope and also increased in absolute abundance by a $\log_2$ fold-change value greater than 2.0 (Figure 2-5I). Frequency of Met residues in the primary amino acid sequence did not affect L-Arg^{+0} isotope incorporation (Figure 2-5J). Remarkably, all four core histones, MATIIα, and the methionine importer SLC3A2 [28] were among the 8 proteins (Figure 2-5J). These results suggest cells respond to metabolically induced SAM depletion by upregulating the abundance of proteins critical for chromatin stability and methyl-donor metabolism. To our knowledge, this is also the first example of a metabolic stress stimulating increased histone protein abundance, highlighting the importance of chromatin regulation under these conditions.

Figure 2-5: Preferential Methylation Supports Global H3K9me1 under SAM Depletion. (*A* and *B*) Bar graphs illustrating LC-MS/MS-generated $\log_2$ fold-changes for individual H3K9 PTMs in HCT116 cells treated with UNC0642 inhibitor or DMSO (mock treatment control) while cultured for 24 h in methionine replete (*A*) or restricted (*B*) media. $n \geq 2$; error bars represent SD; *$p < 0.05$ (Welch's t test) within PTM; #$p < 0.05$ (Welch's t test) across peptides. (*C*) Bar graph illustrating percent loss in global H3K9me1, as measured by LC-MS/MS, in response to 5 mm UNC0642 treatment. $n \geq 2$; error bars represent SD; *$p < 0.05$ (Welch's t test). (*D*) Plot of relative, total H3, and H3K9me1 cytoplasmic protein abundance in HCT116 cells as measured by western blot. Error bars represent SD; $n = 3$; *$p < 0.05$ (Welch's t test). (*E*) Representative western blot images of those used for the quantification presented in Figure 2-5D. Alpha-tubulin is used as a cytoplasm marker to confirm efficient subcellular fractionation. See Figure 2-15 for REVERT total protein stain images used for normalization. (*F*) Diagram illustrating the SILAC experimental design. (*G*) Bar graph illustrating ratio of light/heavy L-Arg isotope presence in H3K9me1-containing peptides after 24 h of Met restriction in HCT116 cells as measured by LC-MS/MS. $n \geq 3$; error bars represent SD. (*H*) Pie chart depicting sources of H3K9me1 during SAM depletion. (*I*) Scatterplot of 373 cytoplasmic proteins identified by LC-MS/MS with significant incorporation of L-Arg $^{+0}$ that were also significantly upregulated after 24 h of Met restriction in 0.1%-DMSO-treated HCT116 cells. $n = 4$; statistical significance of $p < 0.05$ (Welch's t test).

Figure 2-5: Preferential Methylation Supports Global H3K9me1 under SAM Depletion.

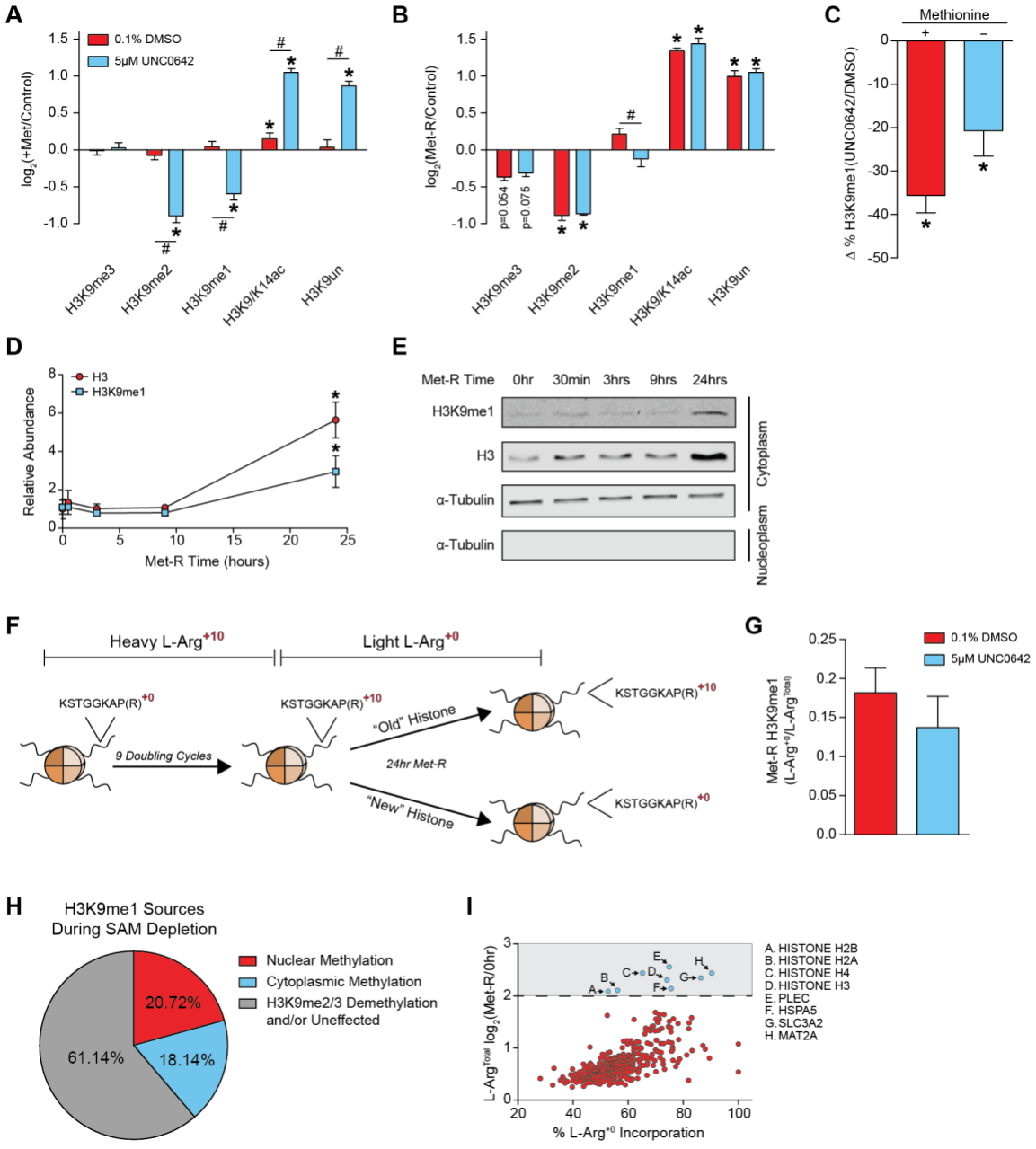

Figure 2-6: Supporting Data Related to Figure 2-5. (*A*-*C*) Scatter plots of relative HMT mRNA abundance in HCT116 cells as measured by RT-qPCR. n=4, error bars represent SD, *p<0.05 (Welch's t-Test). (*D*) Heatmap of log_2 fold-change stoichiometric values for unique histone H3K9 peptide proteoforms in HCT116 cells. n=4, *p<0.05 (Welch's t-Test). (*E*) Scatter plot of relative cell counts for attached HCT116 cells. n=4, error bars represent SD, *p<0.05 (Welch's t-Test). (*F*) Bar graph of relative H3K9me1 abun- dance in HCT116 cells as measured by western blot with accompanied representative blot image. See Figure 2-15 for REVERT Total Protein Stain image used for normalization. Error bars represent SD, n ≥ 3, *p<0.05 (Welch's t-Test). (*G*) Bar graphs illustrating log_2 fold-changes for individual H3K9 PTMs. n ≥ 3, *p<0.05 (Welch's t-Test) within PTM, #p<0.05 (Welch's t-Test) across PTMs. (*H*) Bar graph showing average incorporation of L-Arg^{+10} in H3K9 peptide proteoforms. n=4, error bars represent SD. (*I*) Bar graph illustrating contribution of newly synthesized histone H3 to the total chromatin bound pool after 24 hours of Met-restriction in HCT116 cells as measured by LC-MS/MS. n ≥ 3, error bars represent SD, *p<0.05 (Welch's t-test). (*J*) Density plot illustrating the percentage of Met residue frequency in the primary amino acid sequence of all identified cytoplasmic proteins as well as those determined to be preferentially translated.

Figure 2-6: Supporting Data Related to Figure 2-5.

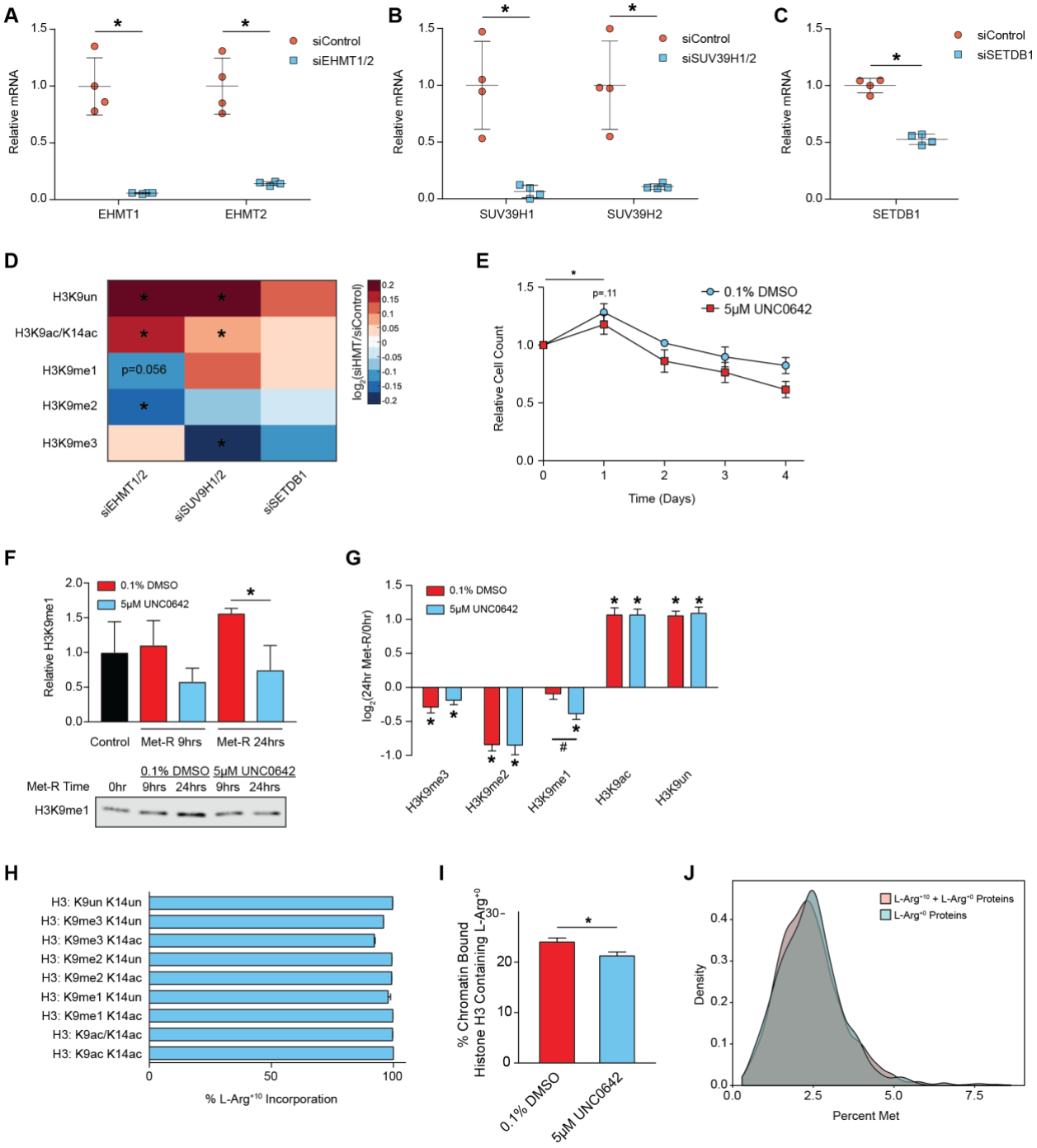

2.3.4 SAM Depletion Stimulates Remodeling of H3K9me1 Over Repetitive and Transposable Elements

Multiple, non-redundant mechanisms for H3K9me1 maintenance suggest strong biological pressure exists to retain this PTM under SAM depleted conditions. One critical function for H3K9me1 is to serve as a primer for H3K9me2/3 methylation as methyltransferases that yield these higher methylation states require a mono-methyl substrate [26,29,30]. Accordingly, installment of H3K9me2/3 for constitutive heterochromatin-mediated repression of telomeric, pericentromeric, and centromeric repetitive/transposable elements requires readily available H3K9me1 [31–33].

To determine if H3K9me1 is being maintained globally or remodeled over regions of susceptible heterochromatin during SAM depletion, ChIP-sequencing was performed. Met-restriction stimulated a 35**%** loss in total H3K9me3 peak number (Figure 2-7A). A higher percentage of H3K9me3 peaks were lost at LTR, intergenic, and intron annotated loci relative to the total, while H3K9me3 peaks at satellite, simple repeat, and SINE annotated loci were slightly less sensitive to SAM depletion (Figure 2-7A). Interestingly, H3K9me1 enrichment at repetitive and transposable loci was either largely unaffected by SAM depletion or increased (Figure 2-7B). Only intergenic and intron annotated H3K9me1 peaks were lost to a greater extent than the total peak number, suggesting H3K9me1 is more susceptible to de-methylation at these genomic loci.

Maintained or increased H3K9me1 peaks at constitutively repressed regions during SAM depletion could result from the replacement of bulk losses in higher-state H3K9 methylation with H3K9me1 at these loci. To investigate this possibility, H3K9me1 ChIP-sequencing reads were mapped to nearly $16e^4$ loci determined to lose H3K9me3 peak enrichment upon SAM depletion.

This analysis determined H3K9me1 enrichment increased at 66.4% of these sites, with a preference for LINE, LTR, simple repeat, and satellite element annotated loci (Figure 2-7C through 2-7E). Figure 2-7F provides a representative image of H3K9me3 replacement by H3K9me1 at a pericentric, repetitive element. Together, these ChIP-sequencing analyses suggest SAM depletion stimulates the remodeling of H3K9me1 methylation over repetitive and transposable genomic loci which are susceptible to higher-state H3K9 demethylation.

Figure 2-7: SAM Depletion Stimulates Remodeling of H3K9me1 Over Repetitive and Transposable Elements. (*A* and *B*) Bar graphs illustrating percent changes in H3K9me3 (*A*) and H3K9me1 (*B*) peak number at various annotated loci after 24 h of Met restriction in HCT116 cells. (*C* and *D*) Plots depicting changes in normalized H3K9me3 (*C*) and H3K9me1 (*D*) ChIP-sequencing reads to loci of lost H3K9me3 peaks after 24 h of Met restriction in HCT116 cells. (*E*) Bar graphs illustrating percent changes in loci annotation for regions of lost H3K9me3 experiencing increased relative to decreased H3K9me1 ChIP sequencing read enrichment after 24 h of Met restriction in HCT116 cells. (*F*) Representative ChIP-sequencing track image.

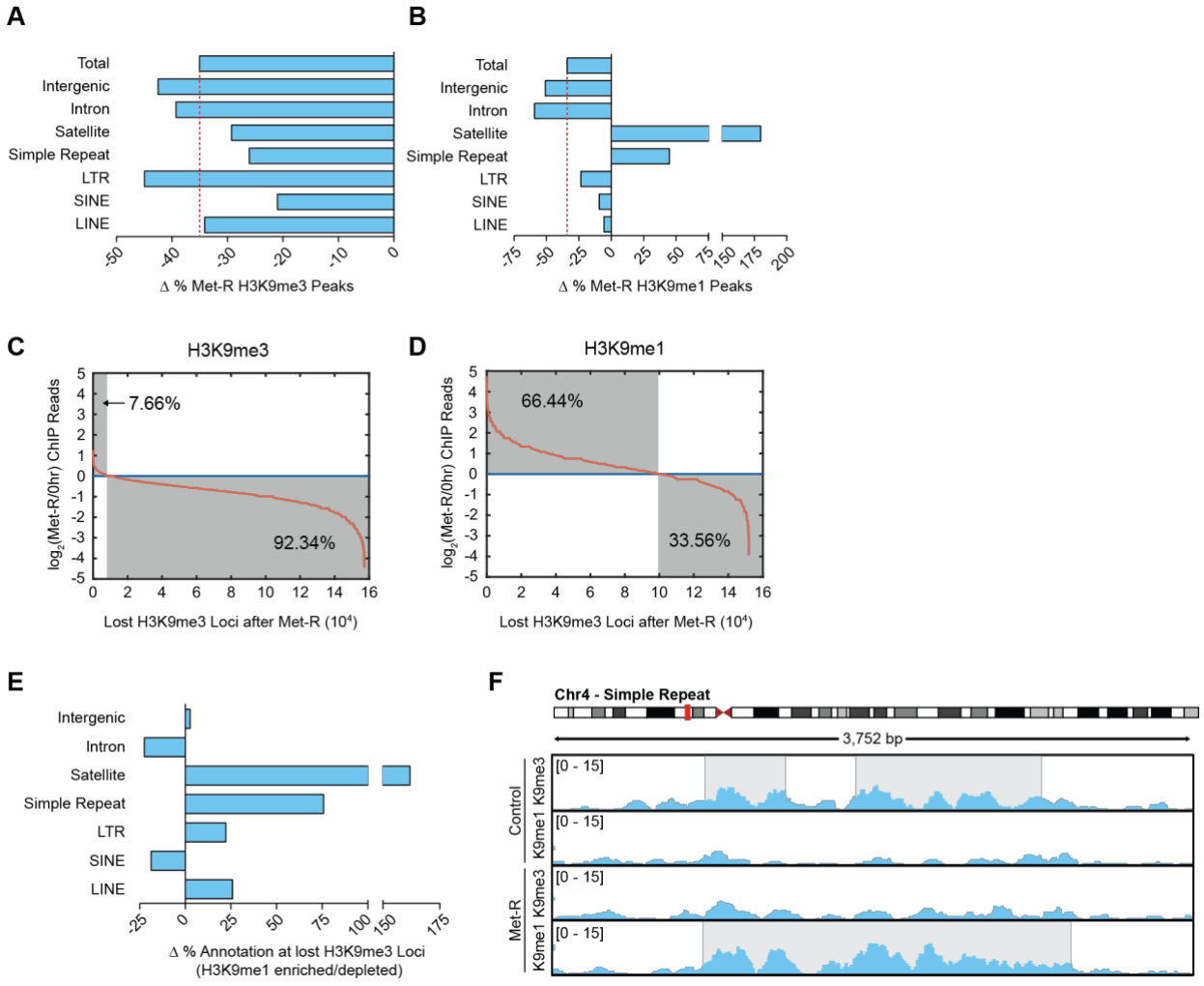

2.3.5 Preferential H3K9 Mono-methylation Preserves Heterochromatin Stability

Replacement of H3K9me3 by H3K9me1 may function to preserve heterochromatin stability and pericentric chromatin repression during SAM depletion by providing the primer for site-specific H3K9me2/3 methylation and/or by preventing H3K9 acetylation. An MNase accessibility assay was used to evaluate global heterochromatin stability under SAM depleted conditions as MNase can more readily digest euchromatic DNA compared to heterochromatic DNA. Coupling Met-restriction with UNC0642 treatment resulted in a significantly greater loss and accumulation of di- and mono-nucleosome species, respectively, compared to Met-restriction alone (Figure 2-8A, 2-8B). This indicates inhibition of H3K9 mono-methylation during SAM depletion has a more detrimental effect on global heterochromatin stability than SAM depletion in isolation. To determine if global decreases in heterochromatin stability resulted in de-repression of transposable DNA elements, RT-qPCR was employed. Transcript abundance of LINE1, HERV-K, and HERV-R were all significantly elevated after SAM depletion. Coupling SAM depletion with UNC0642 treatment resulted in the further elevation of LINE1 and HERV-K transcript abundance while HERV-R expression was unaffected (Figure 2-8C through 2-8E). Because SAM depletion-induced losses in heterochromatin stability and retrotransposon repression are exacerbated with inhibition of nuclear EHMT1/EHMT2 activity, these data suggest adaptive H3K9 methylation functions, in part, to preserve heterochromatin stability.

Figure 2-8: Preferential H3K9 Mono-Methylation Preserves Heterochromatin Stability. (*A*) Bar graph illustrating the percent abundances of 5 distinct nucleosome species following MNase digestion of HCT116 cells. Met restriction coupled with mock (DMSO) or UNC0642 treatment was performed for 24 h. n ≥ 3; error bars represent SD; *p < 0.05 (Welch's t test). (*B*) Representative DNA agarose gel image of those used for the quantification presented in Figure 2-8A. (*C–E*) Bar graphs illustrating relative mRNA abundances of LINE1 (*C*), HERV-K (*D*), and HERV-R (*E*) in HCT116 cells as measured by qRT-PCR. Met restriction coupled with mock (DMSO) or UNC0642 treatment was performed for 24 h. Recovery in Met replete media from either treatment occurred for 24 h before harvest. n ≥ 4; error bars represent SD; *p < 0.05 (Welch's t test).

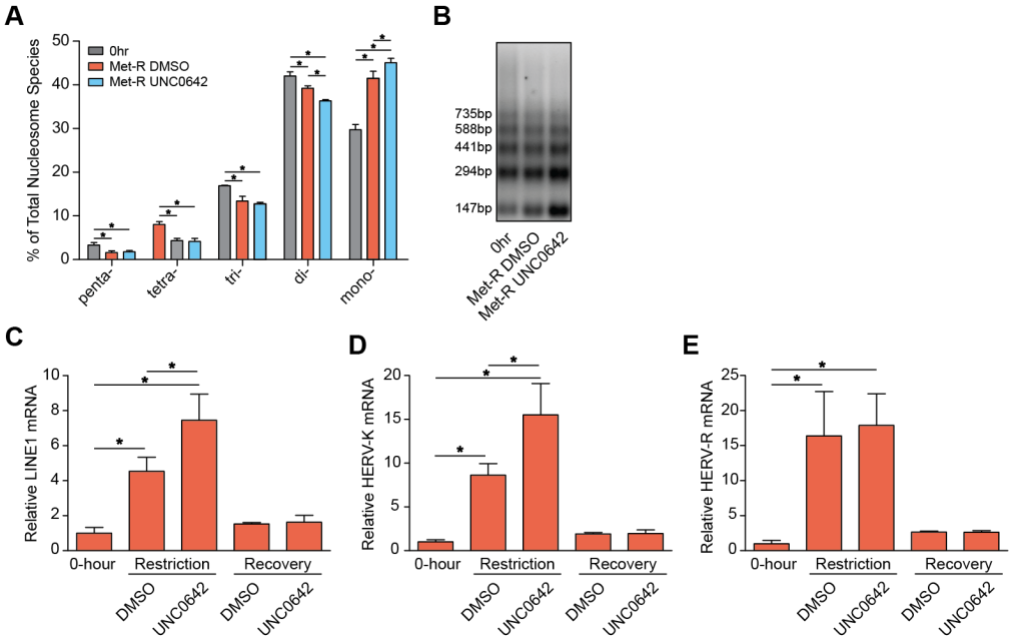

2.3.6 Acute Adaptation of H3K9 Methylation Supports Epigenetic Persistence upon Metabolic Recovery

Dysregulation of cellular response mechanisms under SAM depletion may produce aberrant changes in histone PTMs that compromise long-term epigenetic persistence upon metabolic recovery. To determine if adaptive regulation of H3K9 methylation is required for epigenetic persistence to SAM depletion, HCT116 cells were allowed to recover in Met-replete media after being subjected to Met-restriction coupled with acute mock (DMSO) or UNC0642 treatment (Figure 2-9A). Histone proteomics analysis confirmed that inhibition of EHMT1/EHMT2 activity during SAM depletion results in a significant loss of H3K9me1 abundance (Figure 2-9B, 2-9C). Upon 5 and 24 hours of Met-repletion, mock-treated cells largely regained the original histone PTM state (Figure 2-9B). However, histone PTM states of cells acutely treated with UNC0642 only during Met-restriction remained dysregulated after both 5 and 24 hours of Met-repletion (Figure 2-9B). Although significant global dysregulation was apparent, the H3K9 peptide proteoforms displayed the most dynamic differences in abundance (Figure 2-9D, 2-9E). Interestingly, the signature H3K9 PTM response to SAM depletion described in Figure 2-3 was largely retained upon Met-repletion in cells acutely treated with UNC0642 (Figure 2-9D, 2-9E). H3K9me3 abundance was an exception, recovering to levels consistent with regained LINE1, HERV-K, and HERV-R repression (Figure 2-8C through 2-8E). This suggests a subset of H3K9me1 that is unaffected by acute UNC0642 treatment may mark critical genomic loci (e.g., transposable DNA elements) for higher-state methylation once SAM availability is restored.

Met-replete cells allowed to recover from acute UNC0642 treatment also experienced prolonged changes in H3K9 PTM abundance after inhibitor removal (Figure 2-10A). Because

inhibition of recombinant EHMT1/EHMT2 catalytic activity by UNC0642 is transient (Figure 2-10B), disrupted epigenetic persistence – in either isolation from or conjunction with SAM depletion – is likely a direct consequence of acute losses in EHMT1/EHMT2 H3K9 mono-methylation activity.

To assess whether there were broad transcriptional changes indicative of lost epigenetic persistence, RNA-sequencing was performed on pre-Met-restriction cells as well as those allowed to recover in Met-replete media after acute mock or UNC0642 treatment coupled with Met-Restriction. Principle Component Analysis (PCA) of normalized Transcripts Per Million (TPM) values produced 3 distinct clusters (Figure 2-9F), suggesting the global perturbations in epigenomes (Figure 2-9B) correlate with altered transcript profiles in these cells. A multiple condition comparison analysis was used to determine which transcripts distinguished the clusters from one another. Gene Set Enrichment Analysis (GSEA) of transcripts specific to UNC0642-relative to mock-treated recovery cells revealed 71 significantly enriched gene ontology (GO) terms possessing an FDR q-value less than 0.25 (Figure 2-9G). GO terms covered a wide range of biological processes including “Nucleic Acid Binding Transcription Factor Activity” and “Negative Regulation of Protein Metabolic Processes" among others (Figure 2-11A, 2-11B, Figure 2-12A, 2-12B). An identical analysis of mock- relative to UNC0642-treated recovery genes did not identify any significantly enriched GO terms (Figure 2-9H).

Residually dysregulated gene-expression patterns in UNC0642-treated recovery cells further suggest adaptation of H3K9 methylation to SAM depletion is essential for genome-wide epigenetic persistence upon metabolic recovery. Thus, blocking H3K9 mono-methylation – a critical component of the cellular responses under this condition – has two significant

consequences for the cell: *1.)* exacerbated heterochromatin instability and *2.)* global loss of epigenetic persistence.

Figure 2-9: Acute Adaptation of H3K9 Methylation Supports Epigenetic Persistence upon Metabolic Recovery. (*A*) Diagram illustrating the experimental design for replenishing Met and SAM availability after 24 h of Met restriction coupled with acute 5 mM UNC0642 or 0.1% DMSO treatment in HCT116 cells. (*B*) Heatmap of $\log_2$ fold-change stoichiometric values for histone H3 and H4 peptides as measured by LC-MS/MS. n = 4; *p < 0.05, **p < 0.01 (Welch's t test). (*C–E*) Bar graphs illustrating $\log_2$ fold changes for individual H3K9 PTMs in HCT116 cells as measured by LC-MS/MS. n = 4; error bars represent SD; *p < 0.05 (Welch's t test) within PTM; #p < 0.05 (Welch's t test) across PTMs. (*F*) PCA diagram of TPM values. Cells allowed to recover for 24 h from Met restriction coupled with acute DMSO or UNC0642 treatment were used for this analysis. n = 4. (*G* and *H*) Plots illustrating NES and FDR q-values for GSEA identified GO terms when comparing UNC0642 to mock recovery transcripts and mock to UNC0642 recovery transcripts, respectively.

Figure 2-9: Acute Adaptation of H3K9 Methylation Supports Epigenetic Persistence upon Metabolic Recovery.

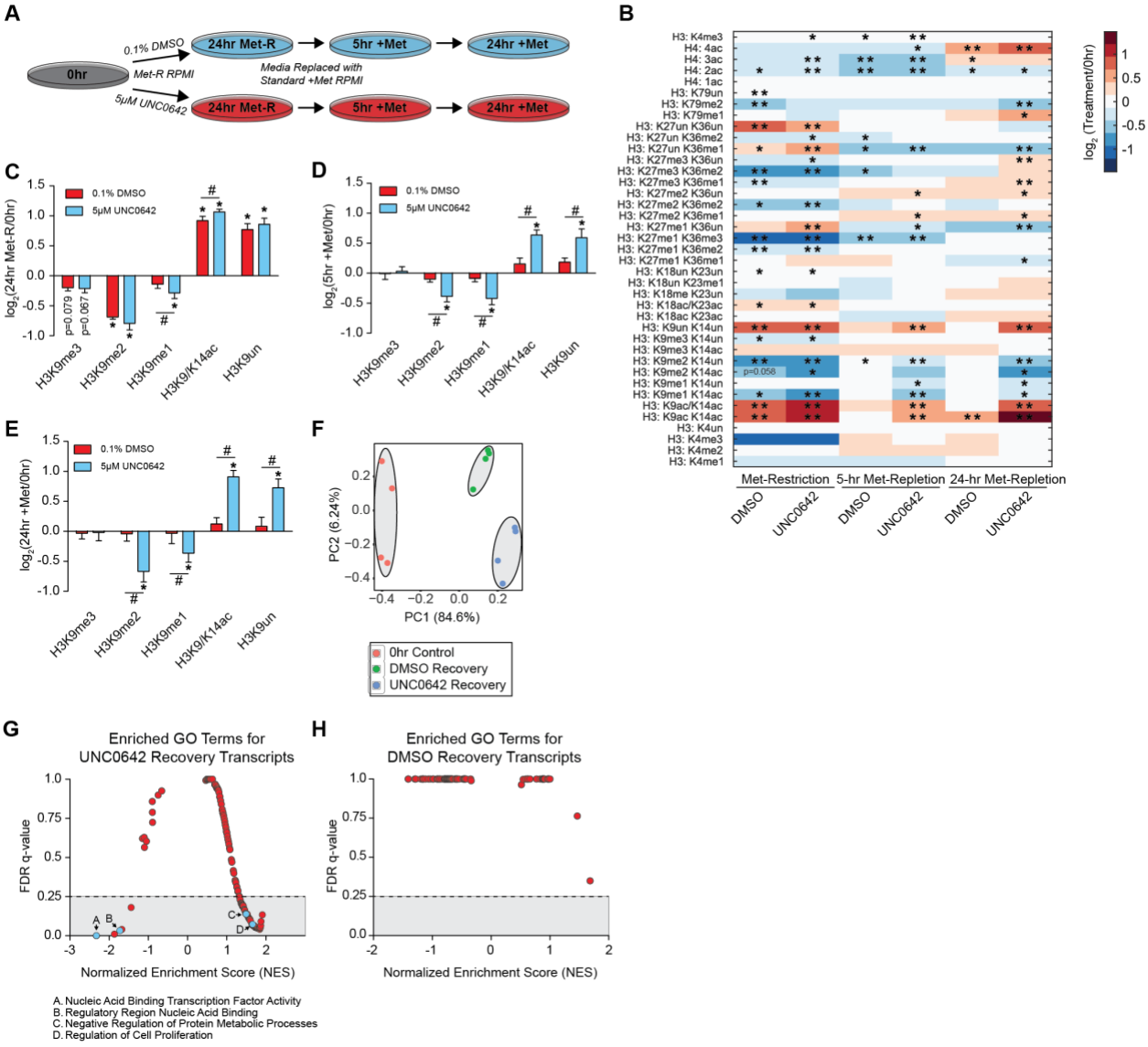

Figure 2-10: Supporting Data Related to Figure 2-9. (*A*) Bar graphs illustrating log_2 fold-changes for individual H3K9 PTMs 24 hours following UNC0642 removal. n=4, error bars represent SD, *p<0.05 (Welch's t-Test) within PTM, #p<0.05 (Welch's t-Test) across PTMs. (*B*) Bar graphs illustrating relative recombinant enzyme activity in the presence of saturating amounts UNC0642 and following 1000x or 10,000x overnight dialysis. n=4, error bars represent SD, *p<0.05 (Welch's t-Test).

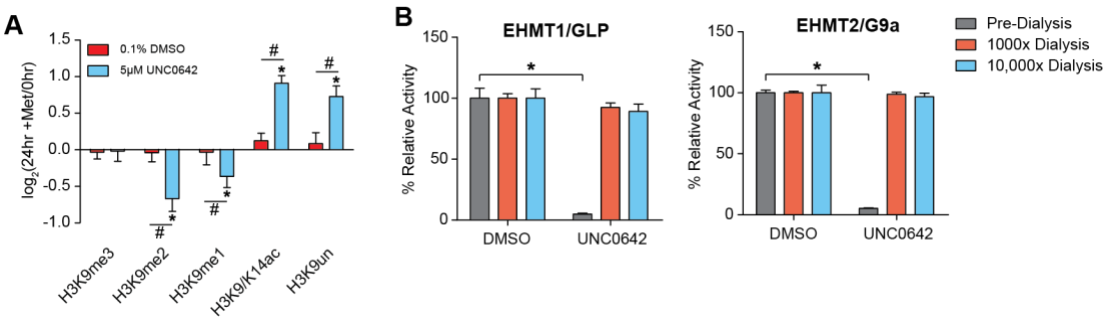

Figure 2-11: Supporting Data Related to Figure 2-9. (*A*) GSEA heatmap of relative gene expression across positive NES GO terms identified when comparing UNC0642- to mock-recovery transcripts. (*B*) GSEA set-to-set heatmap illustrating gene enrichment overlap across positive NES GO listed in panel A.

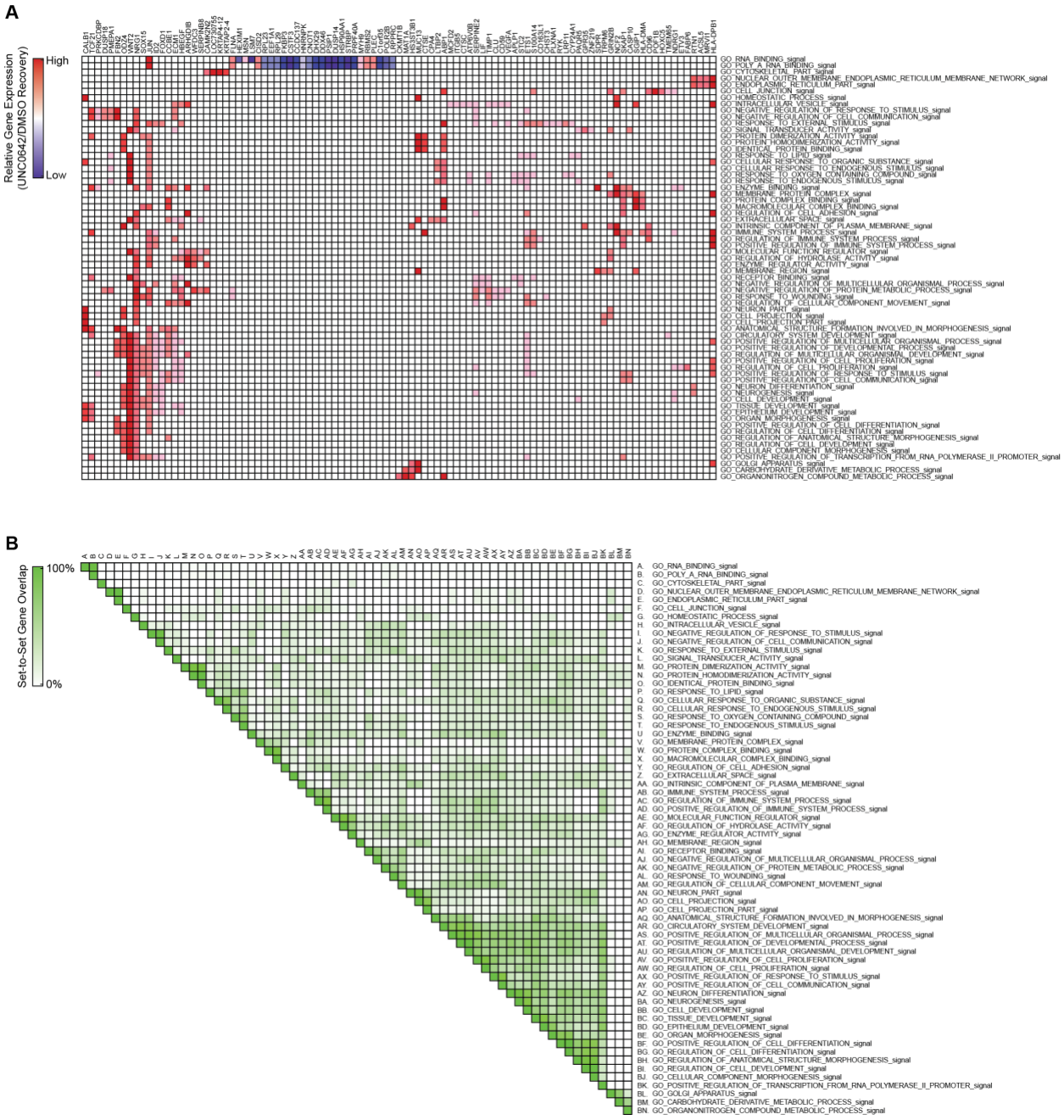

Figure 2-12: Supporting Data Related to Figure 2-9. (*A*) GSEA heatmap of relative gene expression across negative NES GO terms identified when comparing UNC0642- to mock-recovery transcripts. (*B*) GSEA set-to-set heatmap illustrating gene enrichment overlap across negative NES GO terms listed in panel A.

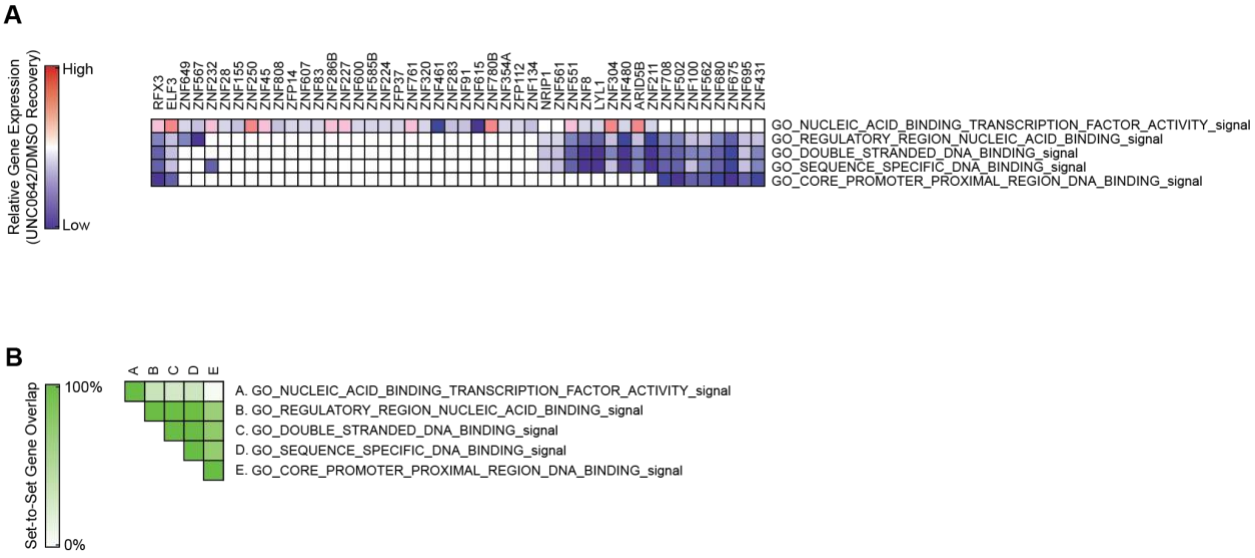

2.3.7 Responses to Ensure Epigenetic Persistence under SAM Depletion are Robust In Vivo, Independent of Age

To determine if robust responses to SAM depletion exist *in vivo* and are age-independent, 6- and 22-month C57BL/6J mice were subjected to 3 weeks of Met-restriction followed by 5 weeks of Met-repletion (Figure 2-13A). Several previous reports have correlated decreased H3K9me2/3 abundance with aging in numerous organisms [34–38]. Age-dependent dysregulation of heterochromatin has also been associated with de-repression of repetitive DNA and transposable elements, as well as DNA damage, which may contribute to disease progression [39–43]. Therefore, conservation of the SAM depletion responses that enable epigenetic persistence across the lifespan would further support the functional importance of these mechanisms as an "older" chromatin environment is thought to be inherently dysregulated.

Remarkably, histone proteomics analysis of liver tissue revealed H3K9 was the only residue on which PTMs responded similarly to SAM depletion in both 6- and 22-month mice relative to age-matched controls (Figure 2-13B). This PTM response at H3K9 phenocopied those in the previously described *in vitro* and whole-organism SAM depletion studies, further highlighting the robust regulation of this residue (Figure 2-13C). Significant age-dependent responses to SAM depletion were identified on all remaining histone residues (Figure 2-13B, 2-14A through 2-14E). Furthermore, significantly elevated LINE1, SINE B1, and SINE B2 transcript abundance in both 6- and 22-month mice suggest the chromatin instability phenotype characterized in Figure 2-8 also occurs during metabolic depletion of SAM *in vivo* (Figure 2-13D, 2-13E). After 5 weeks of dietary Met-reintroduction, both young and old mice displayed the ability to re-establish an epigenome similar to that possessed by age-matched controls (Figure 2-13B). Interestingly, 22-month mice appeared to more rapidly adopt the control histone

PTM state, while the 6-month mice still exhibited residual losses in H3K9me3 and increases in H3K9me1 after 5 weeks of recovery (Figure 2-13F). Consistent with the general recovery of chromatin states, both age groups largely re-established repression of LINE1, SINE B1, and SINE B2 expression (Figure 2-13G, 2-13H).

Metabolic changes in young and old mice tracked with H3K9 methylation patterns. Both 6- and 22-month mice in the Met-restriction group experienced significant losses in total body weight relative to age matched controls (Figure 2-14F). Decreases in overall body weight were comprised of significant losses in both lean and fat mass (Figure 2-14F). Altered body-weight and compositions were accompanied by significantly improved glucose tolerance in both young and old mice (Figure 2-14G). Upon Met-repletion, mice re-acquired their initial metabolic state in an age-independent manner. All animals experienced significant increases in total body weight, comprised of elevated lean and fat mass, as well normalized glucose tolerance relative to age-matched controls (Figure 2-14H, 2-14I).

Together, strong association of the H3K9 chromatin response to SAM depletion with metabolic reprogramming in young and old mice suggest H3K9 adaptation mechanisms are not only robust across lifespan but may facilitate these metabolic phenotypes. Further studies will be needed to determine whether the molecular events described here in response to SAM depletion are directly responsible for metabolic remodeling. Most importantly, these data show the ability of epigenetic states to persist upon recovery from a metabolic challenge is an inherent property of both isolated cells and complex mammals.

Figure 2-13: Responses to Ensure Epigenetic Persistence under SAM Depletion Are Robust *In Vivo*, Independent of Age. (*A*) Diagram depicting the experimental design for in vivo Met restriction of 6- and 22-month-old C57BL/6J mice followed by dietary Met reintroduction. (*B*) Heatmap of log_2 fold-change stoichiometric values for histone H3 and H4 peptides in C57BL/6J liver relative to age-matched controls as measured by LC-MS/ MS. n R 5; *p < 0.05, **p < 0.01 (Welch's t test). (*C*) Bar graph illustrating log_2 fold changes for individual H3K9 PTMs in liver from Met-restricted C57BL/6J mice relative to age-matched controls as measured by LC-MS/MS. n ≥ 5; error bars represent SD; *p < 0.05 (Welch's t test) within PTM; #p < 0.05 (Welch's t test) across PTMs. (*D* and *E*) Bar graphs illustrating relative mRNA abundances of LINE1, SINE B1, and SINE B2 in liver from 6-month (*D*) and 22-month (*E*) old methionine restricted C57BL/6J mice as measured by qRT-PCR. n ≥ 5; error bars represent SD; *p < 0.05 (Student's t test). (*F*) Bar graph illustrating log2 fold changes for individual H3K9 PTMs in liver from C57BL/6J relative to age-matched controls as measured by LC-MS/MS. n ≥ 5; error bars represent SD; *p < 0.05 (Welch's t test). (*G* and *H*) Bar graphs illustrating relative mRNA abundances of LINE1, SINE B1, and SINE B2 in liver from 6-month (*G*) and 22-month (*H*) old C57BL/6J mice following dietary methionine reintroduction as measured by qRT-PCR. n ≥ 5; error bars represent SD; *p < 0.05 (Student's t test).

Figure 2-13: Responses to Ensure Epigenetic Persistence under SAM Depletion Are Robust *In Vivo*, Independent of Age.

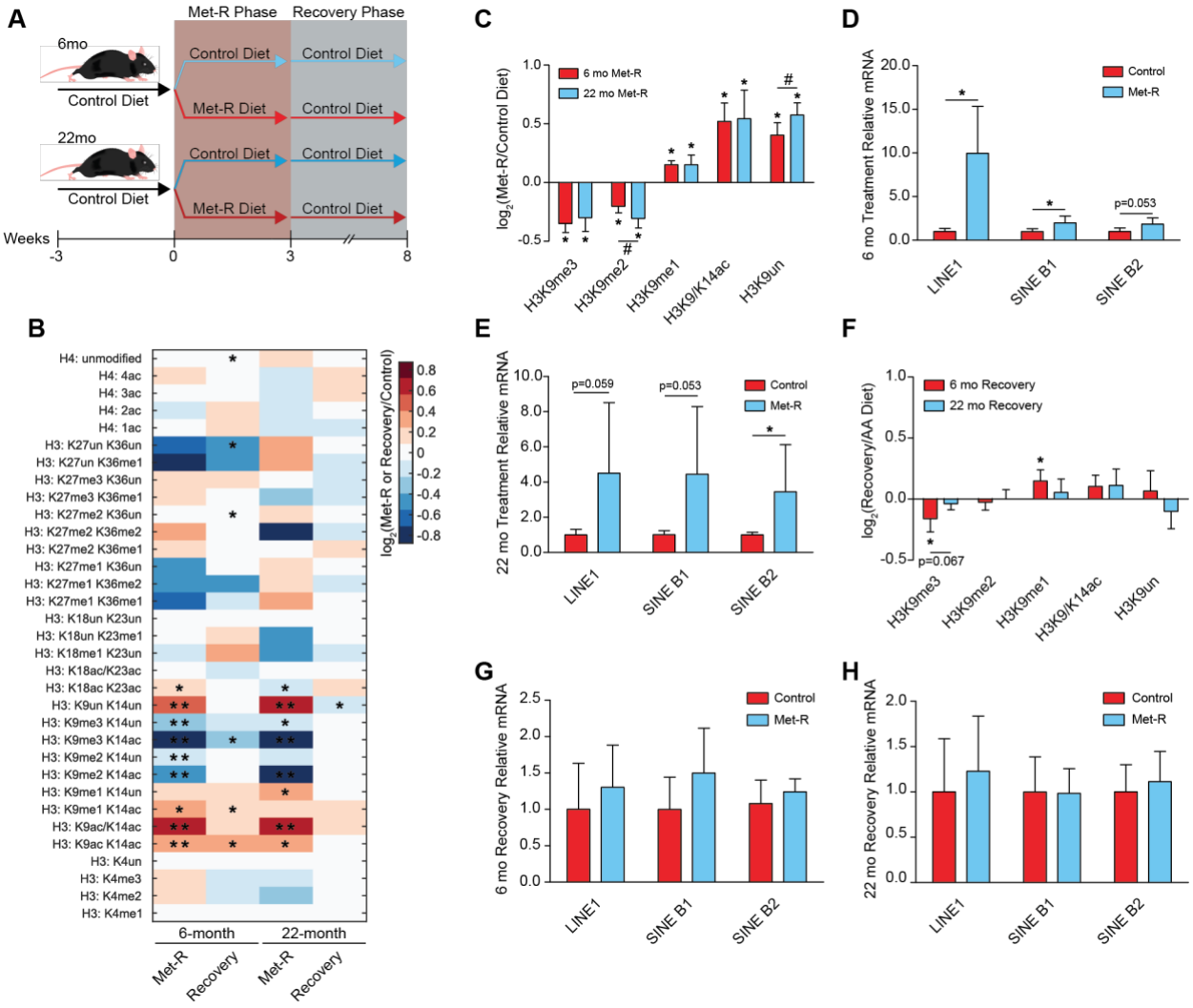

Figure 2-14: Supporting Data Related to Figure 2-13. (*A-E*) Bar graphs illustrating log2 fold-changes for individual H3K4, H3K18/K23, H3K27, H3K36, and H4 PTMs in liver from Met-restricted C57BL/6J mice relative to age-matched controls as measured by LC-MS/MS. $n \geq 5$, error bars represent SD, *$p<0.05$ (Welch's t-Test) within PTM, #$p<0.05$ (Welch's t-Test) across PTMs. (*F*) Bar graph illustrating changes in fat, lean mass, and total body mass (BW) after 3 weeks of control or Met-restricted diet feeding. n=14, error bars represent SEM, *$p<0.05$ (two-way ANOVA). (*G*) Glucose tolerance test in 6- and 22-month C57BL/6J mice after 2 weeks of control or Met-restricted diet feeding. n=14, error bars represent SEM, *$p<0.05$ (two-way ANOVA). (*H*) Bar graph illustrating changes in fat, lean mass, and total body mass (BW) after 5 weeks of control diet feeding following either 3 weeks of control or Met-restricted diet feeding. $n \geq 6$, error bars represent SEM, *$p<0.05$ (two-way ANOVA). (*I*) Glucose tolerance test in 6- and 22-month C57BL/6J mice after 4 weeks of control diet feeding following either 3 weeks of control or Met-restricted diet feeding. $n \geq 7$, error bars represent SEM, *$p<0.05$ (two-way ANOVA).

Figure 2-14: Supporting Data Related to Figure 2-13.

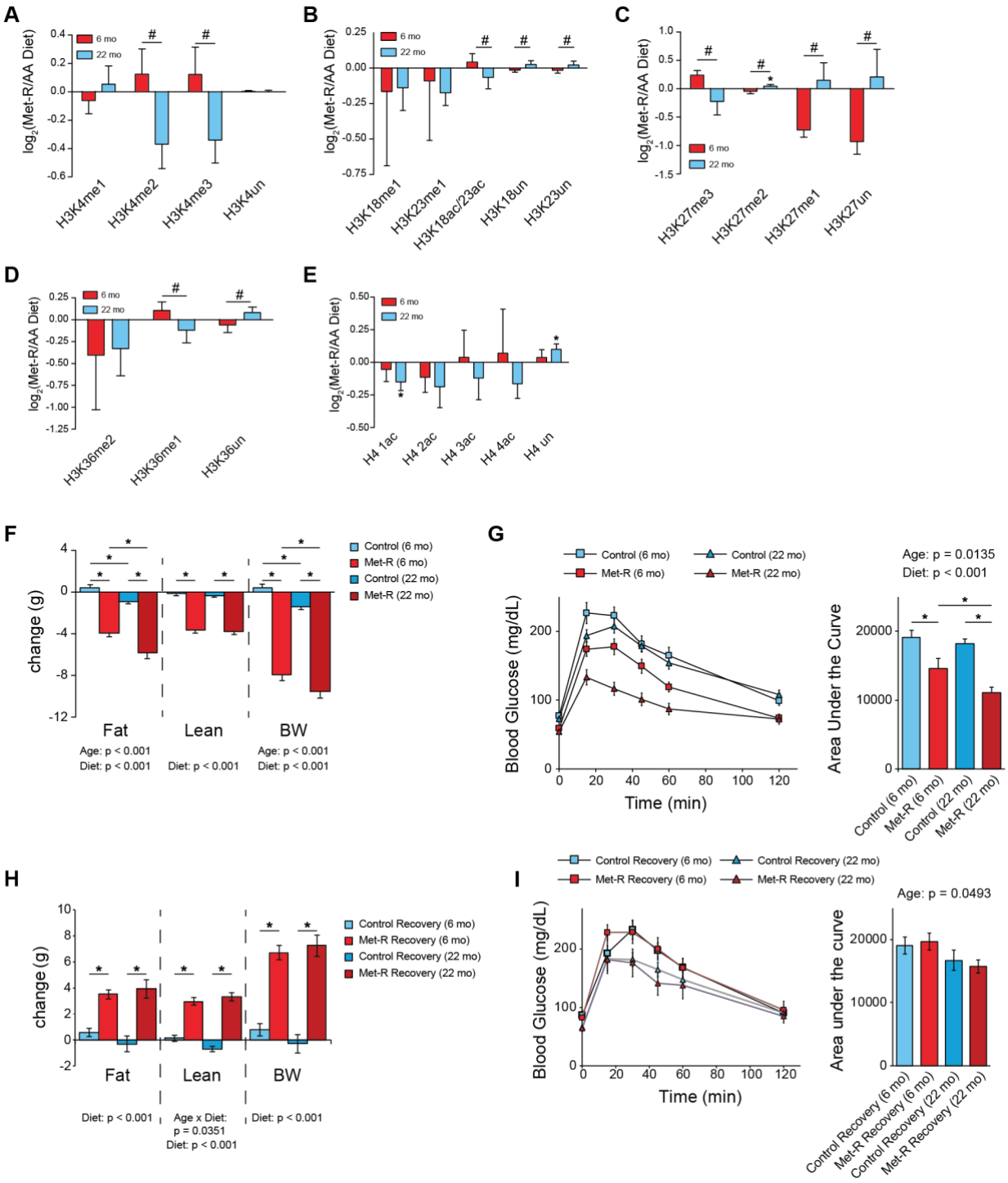

Figure 2-15: Immunoblot and REVERT Total Protein Stain Membrane Images. (*A*) Cytoplasm anti-H3K9me1 (Figure 2-5E). (*B*) REVERT Total Protein Stain for cytoplasm anti-H3K9me1 (Figure 2-5E). (*C*) Cytoplasm anti-H3 (Figure 2-5E). (*D*) REVERT Total Protein Stain for cytoplasm anti-H3 (Figure 2-5E). (*E*) Cytoplasm anti-α Tubulin (Figure 2-5E). (*F*) REVERT Total Protein Stain for cytoplasm anti-αTubulin (Figure 2-5E). (*G*) Nucleoplasm anti-α Tubulin (Figure 2-5E). (*H*) REVERT Total Protein Stain for nucleoplasm anti-αTubulin (Figure 2-5E). (*I*) Purified histone anti-H3K9me1 (Figure 2-6F). (*J*) REVERT Total Protein Stain for purified histone anti-H3K9me1 (Figure 2-6F).

Figure 2-15: Immunoblot and REVERT Total Protein Stain Membrane Images.

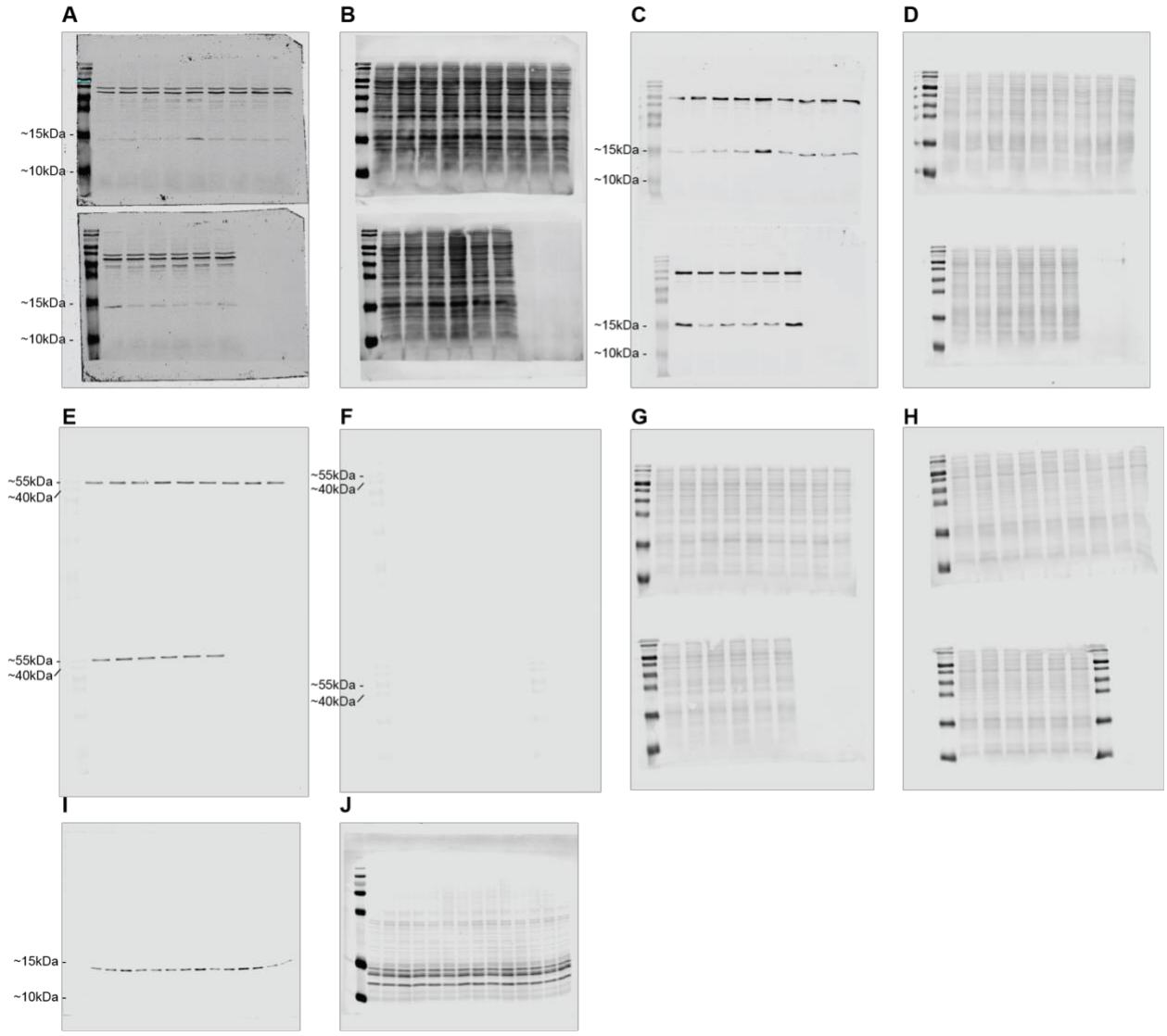

2.4 Discussion

Here, we provide a comprehensive investigation into the regulation of chromatin during a metabolic stress. A highly conserved, robust histone methylation response to SAM depletion was discovered, characterized by broad losses in histone H3 di- and tri-methylation while H3K9me1 is maintained to safeguard against exacerbated heterochromatin instability and support epigenetic persistence upon metabolic recovery. Preferential maintenance of H3K9me1 abundance is facilitated by nuclear and cytoplasmic H3K9 mono-methylation events. Moreover, the highly selective upregulation of all four core histone proteins, the SAM synthetase MATIIα, and the methionine importer SLC3A2 provide compelling evidence that cells mount a coordinated, adaptive response to preserve chromatin states. To our knowledge, this is the first identified mechanism in which scarce, diet-derived nutrients are funneled toward the preservation of specific chromatin PTM states.

It has previously been determined H3K9me1 has the shortest half-life of 17 measured PTMs [44], highlighting the importance of adaptive, preferential methylation for supporting global H3K9me1 abundance in a SAM depleted environment. Here, epigenetic adaptation was found to be critical for more than simply sustaining global H3K9me1 levels under these conditions. ChIP-sequencing analyses determined H3K9me1 patterns experience a significant remodeling across heterochromatin that results in H3K9me1 enrichment at repetitive and transposable DNA elements, particularly in regions where H3K9me3 is lost. Targeting of H3K9me1 to these regions is likely critical for preserving heterochromatin as inhibition of nuclear H3K9 mono-methylation resulted in global losses in heterochromatin stability and site-specific retrotransposon de-repression. We hypothesize H3K9me1 facilitates repression of retrotransposons during SAM depletion through two simultaneous mechanisms: *1.*) acting as the

primed substrate for HMTs which deposit di- and tri-methyl PTMs onto H3K9 and *2.*) preventing the acetylation of newly demethylated H3K9 residues. Increased H3K9 acetylation through impaired H3K9 deacetylation pathways is associated with global genomic instability as well as de-repression of LINE1, providing support for the second mechanism [45–47].

Ensuring sufficient amounts of H3K9me1 are available to facilitate heterochromatin stability is not limited to nuclear derived H3K9me1. Pinheiro et al., 2012 have previously shown inhibition of cytoplasmic H3K9 mono-methylation through shRNA knockdown of *Prdm3* and *Prdm16* stimulates pericentric heterochromatin loss and disruption of the nuclear lamina [27]. Our study demonstrates cytoplasmic derived H3K9me1 comprises a significant portion (18%) of the total chromatin bound pool after 24 hours of Met-restriction *in vitro.* Adaptive regulation of H3K9me1 during SAM depletion is also critical for long-term epigenetic persistence to this metabolic stress. Inhibition of nuclear H3K9 mono-methylation under this condition resulted in sustained dysregulation of global histone PTMs upon metabolic recovery, significantly influencing global gene expression patterns. This requirement for an adaptive histone PTM response to support epigenetic persistence upon metabolic recovery is the first identified mechanism of its kind.

Replication of *in vitro* results *in vivo*, independent of age, strongly supports the discovery of a universal response to SAM depletion. Here, we demonstrate that the acute mechanisms required to support H3K9me1-mediated heterochromatin stability are inducible in both 6- and 22-month mice after dietary Met-restriction. Furthermore, H3K9me1 maintenance under SAM depleted conditions uniquely correlated with beneficial metabolic reprogramming (i.e., reduced fat mass and improved glucose tolerance) in both young and old mice. This suggests the robust regulation of H3K9 PTMs in response to SAM depletion may be required to support the

metabolic reprogramming stimulated by dietary Met-restriction. Future studies will be needed to determine if the chromatin-directed responses upon acute SAM depletion are directly responsible for this metabolic reprogramming. Global epigenetic persistence to metabolic SAM depletion was observed in both 6- and 22-month mice. Validation of this phenomenon *in vivo*, independent of age, suggests similar mechanisms critical for maintaining proper regulation of the epigenome during life-experienced fluctuations in the availability of other metabolic cofactors may exist as well. Such fluctuations could be stimulated by periods of prolonged fasts, chronic intake of foods lacking essential cofactors, and circadian regulated changes in metabolite availability [15–17].

Notably, we did not observe an age-associated decrease in H3K9 methylation between 6- and 22-month control diet mice. Similar regulation of H3K9 PTMs and mirrored metabolic responses to SAM depletion across age groups suggest our 22-month mice, the equivalent to a 60-70 year old human, have not yet experienced a decline in health-span [48]. It will be interesting to determine if the acute responses to ensure epigenetic persistence revealed here are functional in very old animals (i.e., >30 months) where H3K9 methylation is thought to be inherently dysregulated. Disruption of these mechanisms later in an organism's lifespan could support age-associated de-repression of transposable elements [39,41–43], contributing to negative phenotypes that accelerate the aging process [40,46].

Future studies will be needed to determine how H3K9 mono-methyltransferases are able to maintain their catalytic activity under SAM depleted environments. One interesting possibility is that H3K9 mono-methyltransferases have evolved to possess inherent kinetic properties, such as an extremely high affinity for SAM, that allow these enzymes to function at very low SAM levels. The existing literature on H3K9 HMT enzymology is incomplete, making such a conclusion only possible after a comprehensive *in vitro* analysis is performed. Direct shuttling of

SAM to H3K9me1 HMTs by MATIIα could also support H3K9me1 HMT catalytic activity. As SAM is energetically expensive to produce, due to the 1:1 requirement of Met and ATP molecules for its synthesis, in addition to being highly unstable [49], it would be advantageous for the cell to possess mechanisms which permit preferential shuttling of SAM during methyl-metabolite depletion. Directed SAM production and utilization have been proposed in other metabolic contexts [7,50,51].

2.5 Experimental Procedures

2.5.1 Animals and Diets

All experiments involving animals were approved by the Institutional Animal Care and Use Committee of the William S. Middleton Memorial Veterans Hospital, Madison WI. To test the effect of Met deprivation in the context of young mice, 9-week-old male C57BL/6J mice were purchased from The Jackson Laboratory (Bar Harbor, ME, USA) and placed on either an amino acid defined Control diet (TD.01084, Envigo, Madison, WI, USA) or a Met-deficient diet (TD.140119, Envigo, Madison, WI, USA) their respective diets at 14 weeks of age; full diet compositions for these diets have been previously described [23]. After 5 weeks on the diet, mice were sacrificed following an overnight fast and liver was flash frozen for analysis as described.

To compare the effect of Met restriction on young and old mice, C57BL/6J. NIA male mice were obtained from the National Institute on Aging Aged Rodent Colony, and housed in our animal facility for 3-4 months until reaching 5 and 21 months of age. All animals were then placed on the Control diet (TD.01084) for 4 weeks, until the mice were 6 and 22 months of age. Mice were then randomized to either remain on the Control diet, or were placed on the Met-deficient diet (TD.140119) for three weeks. Liver was collected and flash-frozen in liquid nitrogen harvested from mice euthanized after an approximately 16-hour fast.

2.5.2 Cell Lines

HCT116, HEK-293, HEK-293T, HMCF7, Panc1, HepG2, and HepA1 cell lines were cultured at 37^{o}C with 5.0% CO_2.

2.5.3 Metabolite Extraction

For HCT116 cells, ~1.5x10^6 cells were quickly rinsed 3 times with 1.5 ml ice-cold PBS pH 7.4 before the addition of 1.5 ml of -80ºC 80:20 MeOH:H_2O extraction solvent. Cells were incubated with extraction solvent at -80ºC for 15 minutes. Next, cells were scraped off their dish and transferred into a 2 ml microcentrifuge Eppendorf tube which was followed by a 5-minute, maximum speed centrifugation at 4ºC. The supernatant was transferred to a new 2 ml microcentrifuge Eppendorf tube. Next, 0.5 ml extraction solvent was added to the remaining pellet, vortexed, and again centrifugated at maximum speed for 5 minutes at 4ºC. The 2 supernatants from each extraction were pooled and dried completely using a Thermo Fisher Savant ISS110 SpeedVac. Dried metabolite extracts were resuspended in 80 µl of 85% acetonitrile following microcentrifugation for 5 minutes at maximum speed at 4ºC to pellet any remaining insoluble debris. The supernatant was then transferred to a glass vial for LC-MS analysis.

For *M. musculus* liver tissue, an average tissue weight of 75 mg was powdered in liquid nitrogen using a mortar and pestle. Powdered tissue was transferred to an individual 1.5 ml microcentrifuge Eppendorf tube and incubated with 1 ml -80ºC 80:20 MeOH:H_2O extraction solvent on dry ice for 5 minutes post-vortexing. Tissue homogenate was centrifugated at maximum speed for 5 minutes at 4ºC. Supernatant was transferred to a 15 ml tube after which the remaining pellet was resuspended in 0.8 ml -20ºC 40:40:20 ACN:MeOH:H_2O extraction solvent and incubated on ice for 5 minutes. Tissue homogenate was again centrifugated at maximum speed for 5 minutes at 4ºC after which the supernatant was pooled with the previously isolated metabolite fraction. The 40:40:20 ACN:MeOH:H_2O extraction was then repeated as previously described. Next, 550 µl of pooled metabolite extract for each sample was transferred

to a 1.5 ml microcentrifuge Eppendorf tube and completely dried using a Thermo Fisher Savant ISS110 SpeedVac. Dried metabolite extracts were resuspended in 450 µl of 85% ACN following microcentrifugation for 5 minutes at maximum speed at 4°C to pellet any remaining insoluble debris. Supernatant was then transferred to a glass vial for LC-MS analysis.

2.5.4 LC-MS Metabolite Analysis

Each prepared metabolite sample was injected onto a Thermo Fisher Scientific Vanquish UHPLC with a Waters XBridge BEH Amide column (100 mm x 2.1 mm, 3.5 µm) coupled to a Thermo Fisher Q-Exactive mass spectrometer. Mobile phase (A) consisted of 97% H_2O, 3% ACN, 20 mM ammonium acetate, and 15 mM ammonium hydroxide pH 9.6. Organic phase (B) consisted of 100% ACN. Metabolites were resolved using the following linear gradient: 0 min, 85% B, 0.15 ml/min; 1.5 min, 85% B, 0.15 ml/min; 5.5 min, 40% B, 0.15 ml/min; 10 min, 40% B, 0.15 ml/min; 10.5 min, 40% B, 0.3 ml/min; 14.5 min, 40% B, 0.3 ml/min; 15 min, 85% B, 0.15 ml/min; 20 min, 85% B, 0.15 ml/min. The mass spectrometer was operated in positive ionization mode with a MS1 scan at resolution = 70,000, automatic gain control target = 3×10^6, and scan range = 60-186 m/z and 187-900 m/z. This protocol was adapted from Mentch et al., 2015. Individual metabolite data were called using MAVEN [52,53] with retention times empirically determined in-house. Peak Area Top values were analyzed to determine metabolite expression.

2.5.5 LC-MS DNA Methylation Assay

500 ng of cytosine, 5mC, and 5hmC double-stranded DNA standards from Zymo Research were incubated with Zymo Research DNA Degradase Plus for 3 hours at 37°C

following enzyme inactivation at 70°C for 20 minutes. 75 µl of ACN was added to each standard reaction to bring the final volume to 100 µl. DNA standards were centrifugated at 21,100xg for 5 minutes at 4°C after which 75 µl of supernatant was transferred to a glass vial for LC-MS analysis. A range of 0.1 to 100 ng of digested DNA was analyzed via LC-MS to determine each nucleoside's linear range of detection.

Genomic DNA extracted using a Promega Wizard Genomic DNA Purification Kit after which 1 µg was incubated with Zymo Research DNA Degradase Plus at 37°C following enzyme inactivation at 70°C for 20 minutes. 175 µl of ACN was added to each reaction to bring the final volume to 200 µl. DNA samples were centrifugated at 21,100xg for 5 minutes at 4°C after which 150 µl of supernatant was transferred to a glass vial for LC-MS analysis.

Each prepared nucleoside sample was injected onto a Thermo Fisher Scientific Vanquish UHPLC with a Waters XBridge BEH Amide column (100 m x 2.1 mm, 3.5 µm) coupled to a Thermo Fisher Q-Exactive mass spectrometer run in positive ionization mode. Mobile phase (B) consisted of H_2O, 3% ACN, 20 mM ammonium acetate, and 15 mM ammonium hydroxide pH 9.6. Organic phase (B) consisted of 100% ACN. Nucleosides were resolved using the following linear gradient: 0 min, 85% B, 0.15 ml/min; 1.5 min, 85% B, 0.15 ml/min; 5.5 min, 40% B, 0.15 ml/min; 10 min, 40% B, 0.15 ml/min; 10.5 min, 40% B, 0.3 ml/min; 14.5 min, 40% B, 0.3 ml/min; 15 min, 85% B, 0.15 ml/min; 20 min, 85% B, 0.15 ml/min. The mass spectrometer was operated in positive ionization mode with a MS1 scan at resolution = 70,000, automatic gain control target = 3×10^6, and scan range = 200-300 m/z, followed by a DDA scan with a loop count of 5. DDA settings were as follows: window size = 2.0 m/z, resolution = 17,500, automatic gain control target = 1×10^5, DDA maximum fill time = 50 ms, and normalized collision energy = 30. This protocol was adapted from Mentch et al., 2015. Individual metabolite data were called

using MAVEN [52,53] with retention times empirically determined in-house. Peak Area Top values were analyzed to determine metabolite expression with dAdenosine being utilized for internal normalization (m/z dCytosine: 228.0978, m/z d5mC: 242.1135, m/z d5hmC: 258.108, m/z dAdenosine: 252.109).

2.5.6 Histone Isolation and Chemical Derivatization

Tissue culture cell pellets were resuspended in 800 µl of ice-cold Buffer A (10 mM Tris-HCl pH 7.4, 10 mM NaCl, and 3 mM $MgCl_2$) supplied with protease and histone deacetylase inhibitors (10 µg/ml leupeptin, 10 µg/ml aprotinin, 100 µM phenylmethylsulfonyl fluoride, 10 mM nicotinamide, 1 mM sodium-butyrate, and 4 µM trichostatin A) followed by 80 strokes of light pestle homogenization in a 1 ml Wheaton dounce homogenizer. Cell homogenate was then transferred to a 1.5 ml microcentrifuge Eppendorf tube and centrifugated at 800xg for 10 minutes at 4°C to pellet nuclei. The supernatant was either transferred to a fresh 1.5 ml Eppendorf tube or discarded. The nuclei pellet was resuspended in 500 µl ice-cold PBS pH 7.4 followed by centrifugation at 800xg for 10 minutes at 4°C. The supernatant was discarded and nuclei were again washed with 500 µl ice-cold PBS pH 7.4. Pelleted nuclei were then resuspended in 500 µl of 0.4N H_2SO_4 and rotated at 4°C for 4 hours. Samples were centrifugated at 3,400xg for 5 minutes at 4°C to pellet nuclear debris and precipitated non-histone proteins. The supernatant was transferred to a new 1.5 ml Eppendorf tube after which 125 µl of 100% trichloroacetic acid was added and incubated overnight on ice at 4°C. Samples were centrifugated at 3,400xg for 5 minutes at 4°C to pellet precipitated histone proteins. The supernatant was discarded, after which the precipitant was washed with 1 ml ice-cold acetone +0.1% HCl. Samples were centrifugated at 3,400xg for 2 minutes at 4°C and the supernatant was discarded. This process was repeated

except precipitant was washed with 100% ice-cold acetone. Residual acetone was allowed to evaporate at room temperature for 10 minutes after which the dried precipitant was dissolved in 125 µl H_2O. Samples were then centrifugated at 21,100xg for 5 minutes at 4°C to pellet any remaining insoluble debris. Supernatant containing purified histone was then transferred to a new 1.5 ml Eppendorf tube and stored at -20°C until needed for future analyses.

For *M. musculus* liver tissue, an average tissue weight of 50 mg was homogenized in 800µl ice-cold Buffer supplemented with protease and HDAC inhibitors (listed above) using a 1 ml Wheaton dounce homogenizer (20 strokes of the loose pestle followed by 20 strokes of the tight pestle) and strained through a 100 µM filter before being transferred to a new 1.5 ml Eppendorf tube. All remaining steps for completing the histone isolation were performed as described previously in the tissue culture isolation protocol.

To prepare purified histone proteins for LC-MS/MS analysis, 5 µg of histone was diluted with H_2O to a final volume of 9 µl. 1 µl of 1 M triethylammonium bicarbonate was added to each sample to buffer the solution to a final pH of 7-9. Next, 1 µl of 1:100 propionic anhydride:H_2O was added to each sample and allowed to incubate for 2 minutes at room temperature. The propionylation reaction was then quenched via the addition of 1 µl 80 mM hydroxylamine which was allowed to incubate for 20 minutes at room temperature. Next, propionylated histones were digested with 0.1 µg trypsin for 4 hours at 37°C. Upon completion of trypsin digestion, 5 µl of .02 M NaOH was added to bring the final pH between 9-10. Propionylated, trypsin digested histone peptides were then N-terminally modified with 1 µl 1:50 phenyl isocyanate:ACN for 1-hour at 37°C. Modified peptides were desalted and eluted-off of Empore™C18 extraction membrane. Eluted samples were dried completely using a Thermo

Fisher Scientific Savant ISS110 SpeedVac, resuspended in 40 µl sample diluent (94.9% H_2O, 5% ACN, .1% TFA), and transferred into glass vials for LC-MS/MS analysis.

2.5.7 Histone Proteomics Analysis

Derivatized histone peptides were injected onto a Dionex Ultimate3000 nanoflow HPLC with a Waters nanoEase UPLC C18 column (100 m x 150 mm, 3µm) coupled to a Thermo Fisher Q-Exactive mass spectrometer at 700 nL/ min. Aqueous phase (A) consisted of H_2O + 0.1% formic acid while the mobile phase (B) consisted of acetonitrile + 0.1% formic acid (B). Histone peptides were resolved using the following linear gradient: 0 min, 2.0% B; 5 min, 2.0% B; 65 min, 35% B; 67 min, 95% B; 77 min, 95% B; 79 min, 2.0% B; 89 min, 2.0% B. Data was acquired using data-independent acquisition (DIA) mode. The mass spectrometer was operated with a MS1 scan at resolution = 35,000, automatic gain control target = 1×10^6, and scan range = 390-910 m/z, followed by a DIA scan with a loop count of 10. DIA settings were as follows: window size = 10 m/z, resolution = 17,500, automatic gain control target = 1×10^6, DIA maximum fill time = AUTO, and normalized collision energy = 30.

DIA Thermo .raw files were imported into Skyline open source proteomics software [54] and matched against a pre-constructed peptide database containing unique peptide proteoforms from H3 and H4. The identity of each individually called peak was verified by hand after which total MS1 peak area values were exported for downstream analyses. To control for differences in ionization efficiencies across histone peptides, all peptides possessing an identical primary sequence were analyzed as a peptide family which enabled the calculation of stoichiometric values for each unique peptide proteoform within the family. Stoichiometric values were compared across conditions to identify altered histone peptide abundances. Furthermore,

combinatorial peptide stoichiometry values were deconvoluted by totaling the stoichiometry values for all peptides possessing a given PTM independent of any other PTMs that may be present on other residues of the same primary peptide. A Welch's T-Test with a p-value cutoff of 0.05 was used to determine statistical significance.

Hierarchical clustering was performed in MATLAB R2016a using the 'clustergram' command. Pearson's Correlation Coefficients were calculated in MATLAB R2016a using the 'corr' command.

2.5.8 RNAi Mediated Inhibition of MATIIα and H3K9 HMT Expression

For 35 mm tissue culture dishes, $1.5x10^5$ HCT116 cells were reverse transfected with 30 pmol of targeted or control RNAi using 5 µl of Lipofectamine RNAiMAX in addition to 500 µl Opti-MEM and 2.5 ml RPMI-1640 +10% FBS. MATIIα -RNAi treated HCT116 cells used for LC-MS metabolite analysis were cultured using dialyzed FBS. MATIIα-RNAi and H3K9 HMT-RNAi treatments were performed for 48 and 24 hours, respectively.

For 100 mm tissue culture dishes, $2.0x10^6$ HCT116 cells were reverse transfected with 180 pmol of targeted or control RNAi using 30 µl of Lipofectamine RNAiMAX in addition to 2 ml Opti-MEM and 8 ml RPMI-1640 +10% FBS. MATIIα-RNAi and H3K9 HMT-RNAi treatments were performed for 48 and 24 hours, respectively.

RNAi mediated knockdown of MATIIα in HepA1 cells was performed as described in Katoh et al., 2011.

2.5.9 Methionine Restriction of Tissue Culture Cells

HCT116, HEK-293, MCF7, Panc1, and HepG2 culture cells were initially cultured in RPMI-1640 +10% FBS at 37°C, 5% CO_2. One day before Met-restriction, $3.5x10^6$ cells were seeded into 100 mm tissue culture dishes. One-hour before the restriction began, RPMI-1640 was replaced with fresh, Met-replete media. At the time of Met-restriction, cells were rinsed 2x with 3 ml of sterile PBS pH 7.4 followed by addition of RPMI-1640 void of Met. Any small molecule inhibitors or vehicle controls would be added at this time.

For experiments in which Met-restriction was followed by Met repletion, HCT116 cells were washed with 3 ml of sterile PBS pH 7.4 2x to maximize small molecule inhibitor and DMSO removal before reintroduction of Met replete RPMI-1640.

HCT116 cells cultured for LC-MS metabolite analysis were cultured in RPMI-1640 containing 10% dialyzed FBS beginning 1-hour prior to beginning Met-restriction.

Methionine restriction of HEK-293T cells (data presented in Figure 2-3) was performed as previously described by Ye et al., 2017.

2.5.10 SILAC in Tissue Culture

197 ml of SILAC RPMI-1640 +10% DFBS void of L-Arg and L-Lys was supplemented with 50mg isotopically heavy $^{3}C_{6}$ $^{15}N_{4}$ L-Arg HCl and 9.43mg isotopically light L-Lys to obtain final concentrations of 1.149 mM and 0.219 mM, respectively. HCT116 cells were cultured in the SILAC media for 7 days (or 9 doubling cycles at a reported doubling time of 21 hours) after which cells were washed 3x with 5 ml PBS pH 7.4 before replacing the SILAC media with isotopically light L-Arg and L-Lys RPMI-1640 +10% DFBS void of Met. Half of the cells were treated with 5 μM UNC0642 or 0.1% DMSO at this time. Furthermore, 0-hour control HCT116

cells which were never exposed to isotopically light L-Arg, Met-restricted RPMI-1640 were harvested. HCT116 cells cultured in the Met-restricted media were harvested after 24 hours.

2.5.11 SILAC Shotgun Proteomics Analysis

50 μg of cytoplasmic protein extract from the previously described SILAC Met-restriction experiment were diluted with H_2O into a final volume of 75 μl. Next, dithiothreitol was added to each sample at a final concentration of 10 mM, followed by a 15-minute incubation at 95°C. A sonication water bath was used to resolubilize precipitated proteins post-heat denaturation. Iodoacetamide was then added to a final concentration of 20 mM, followed by a 20-minute incubation at room temperature protected from light. Alkylated proteins were precipitated with 337 μl ice-cold acetone for 20 minutes at -20°C. Samples were centrifugated at 21,000xg for 15 minutes at 4°C, the supernatant was discarded, and precipitated protein was resuspended in 400 μl of urea buffer (2 M urea and 100 mM ammonium bicarbonate pH 8). Precipitated proteins were again solubilized using a sonication water bath. Solubilized proteins were digested into peptides using 0.8 μg trypsin at 37°C overnight. Upon digest completion, samples were desalted and eluted-off Empore™C18 extraction membrane. Eluted samples were dried completely using a Thermo Fisher Scientific Savant ISS110 SpeedVac, after which being resuspended in 50 μl sample diluent (94.9% H_2O, 5% ACN, .1% TFA) and transferred to glass vials for LC-MS/MS analysis.

Each prepared cytoplasmic peptide sample was injected onto a Dionex Ultimate3000 nanoflow HPLC with a Waters nanoEase UPLC C18 column (100 m x 150 mm, 3μm) coupled to a Thermo Fisher Q-Exactive mass spectrometer at 800 nL/ min. Aqueous phase (A) consisted of H_2O + 0.1% formic acid while the mobile phase (B) consisted of acetonitrile + 0.1% formic acid

(B). Histone peptides were resolved using the following linear gradient: 0 min, 5.0% B; 5 min, 5.0% B; 120 min, 30% B; 122 min, 95% B; 127 min, 95% B; 129 min, 5.0% B; 145 min, 5.0% B. Data was acquired using data-dependent acquisition (DDA) mode. The mass spectrometer was operated with a MS1 scan at resolution = 70,000, automatic gain control target = 1×10^6, and scan range = 400-1000 m/z, followed by a DDA scan with a loop count of 20. DDA settings were as follows: window size = 2.0 m/z, resolution = 17,500, automatic gain control target = 2×10^5, DDA maximum fill time = 150 ms, and normalized collision energy = 28.

2.5.12 MaxQuant Proteomics Analysis

Thermo .raw DDA files were analyzed using MaxQuant v1.6.2.6 [55] using the default settings with the following exceptions: Labels: 1, Arg10; Instrument: Orbitrap; LFQ: LFQ min. ratio count: 2, LFQ min. number of neighbors: 3, LFQ average number of neighbors: 6; FASTQ File: Proteome: *H. Sapiens* Proteome ID UP000005640.

Identified proteins with a Q-value of 0.01 or above were removed. For the remaining proteins, LFQ light (L-Arg^{+0}) and heavy (L-Arg^{+10}) values were summed to generate LFQ total protein abundance values. LFQ light values were divided by the corresponding LFQ total value to generate a percent abundance of LFQ light species for each identified protein. Welch's t-Tests with a p-value cut off of 0.05 were used to determine significant accumulation of LFQ light species in Met-restricted HCT116 samples relative to 0-hour controls. For proteins determined to have significant LFQ light species abundance after Met-restriction, LFQ total values were used to determine the corresponding change in overall protein abundance. Up to 2 null-values were removed from replicates of an experimental group to account for missed identifications. If 3 of the 4 replicates for a single experimental group contained null-values, that protein was removed

from all experiment groups and therefore excluded from any downstream analyses. A Welch's t-Test with a p-value cut off of 0.05 was used to determine if an identified protein was significantly more abundant after Met-restriction relative to 0-hour controls.

2.5.13 *SILAC Histone Proteomics Analysis*

Histones were isolated, chemically derivatized, and analyzed by LC-MS/MS as described in "Histone Isolation and Chemical Derivatization" and "Histone Proteomics Analysis." DDA Thermo .raw files of histone proteins with incorporated isotopically heavy $3C_6$ $15N_4$ L-Arg were used to construct an H3K9/K14 peptide library using Skyline opensource proteomics software [54]. DIA files were then matched against both isotopically heavy and light L-Arg peptide libraries after which peptide identities were confirmed by hand. MS1 intensity values for both isotopically heavy and light L-Arg peptides were summed to generate total MS1 peptide proteoform intensity values which were then used to calculate the percent of total MS1 peptide proteoform signal which was contributed by isotopically heavy peptide proteoforms. Welch's T-Tests with a p-value cutoff of 0.05 were used to determine significant differences in total MS1 peptide proteoform stoichiometric values as well as the percent contribution of isotopically heavy peptide proteoforms to total peptide proteoform intensity values.

2.5.14 Chromatin Immunoprecipitation and Sequencing

$30x10^6$ HCT116 cells were resuspended in 1 ml MNase digestion buffer (50 mM Tris-HCl pH 7.6, 1 mM $CaCl_2$, and 0.2% Triton X-100) after which 330 µl of the cell suspension was aliquoted into individual 1.5 ml tubes. Each tube was treated with either 45, 52.5, or 60 units of Worthington MNase for 5 minutes at 37°C shaking at 400 rpm to generate mono-nucleosomes.

MNase digestions were stopped via the addition of EDTA to a final concentration of 5mM. Digested cells were then pooled and lysed at 4°C using a Covaris S220 Focused-ultrasonicator with the following settings: Peak Power = 75, Duty Factor = 5, Cycles/Burst = 100, Duration = 30" on/30" off x2. Insoluble debris was centrifugated at 10,000 rpm for 10 minutes at 4°C after which the supernatant containing prepared nucleosomes was transferred to a new tube. Glycerol was added to a final concentration of 5% prior to -80°C storage. For input controls, 43 µl of prepared nucleosomes were aliquoted and saved for further processing at -80°C.

Next, 860 µl of prepared nucleosomes was incubated with 5 µg of the desired antibody, rotating overnight at 4°C. The nucleosome/antibody solution was added to 50 µl of prepared M-280 Sheep Anti-Rabbit IgG superparamagnetic Dynabeads™ and allowed to rotate at 4°C for 4 hours. Conjugated beads were then washed for 10 minutes, rotating at 4°C under the following conditions: 3x 1 ml RIPA (10 mM Tris pH 7.6, 1 mM EDTA, 0.1% SDS, 0.1% Na-deoxycholate, 1% Triton X-100) buffer, 2x 1 ml RIPA buffer +0.3 M NaCl, 2x 1 ml LiCl buffer (0.25 M LiCl, 0.5% NP-40, 0.5% Na-deoxycholate), 1x with 1 ml 1xTE +50 mM NaCl. Following the final wash, beads were centrifugated at 4°C for 3 minutes at 960xg after which the supernatant was carefully removed and discarded.

To elute immunoprecipitated nucleosome species, beads were resuspended in 210 µl of elution buffer (50 mM Tris-HCl pH 8.0, 10 mM EDTA, 1% SDS) and incubated at 65°C for 30 minutes shaking at 400 rpm. Beads were resuspended every 2 minutes via brief vortexing. Next samples were centrifugated at 16,000xg for 1 minute at room temperature after which 200 µl of supernatant was transferred to a new 1.5 ml Eppendorf tube. Eluted nucleosome species were then treated with 2 µl Thermo Fisher Scientific Proteinase K for 2 hours at 55°C. DNA was recovered from the Proteinase K digestion using the QIAquick PCR Purification Kit.

DNA libraries were prepared by the University of Wisconsin-Madison Biotechnology Center using the Illumina TruSeq DNA Nano kit and then sequenced across 4 lanes of an Illumina 1x100 HiSeq2500 High Throughput flowcell.

FASTQ files were aligned unpaired using bowtie2-2.1.0 [56] against human genome 19. Bowtie2 output SAM files were converted to BAM files, sorted and indexed using samtools 1.5 [57]. Broad peaks were called from sorted BAM files using MACS2-2.1.1.20160309 [58] with a Q-value cutoff of 0.1. Input DNA was used as the control file. All identified peaks possessing a $\log_2$ fold-change below 1.75 were discarded prior to downstream analyses. Bedtools v2.25.0 [59] was used to identify unique and overlapping across samples and also used to assign raw mapped reads to pre-specified genomic loci. Genomic loci were annotated using HOMERv4.9 [60].

2.5.15 Quantitative PCR

RNA was extracted from HCT116 cells using Thermo Fisher Scientific TRIzol and from liver tissue using Sigma TRI Reagent, both by following the manufacturer's instructions. The concentration and purity of RNA were determined by absorbance at 260/280 nm.

cDNA was prepared from 1 μg of RNA using RevertAid Reverse Transcriptase for HCT116 RNA and Superscipt III for liver RNA. Oligo dT primers were used in both cDNA synthesizing reactions. For Primer sequences see Table 2-1.

HCT116 cDNA was analyzed on a Roche 480 Light Cycler System with PerfeCTa SYBR Green SuperMix while cDNA generated from liver was analyzed on an Applied Biosystems StepOne Plus instrument with Sybr Green PCR Master Mix. HCT116 cDNA qPCR reactions were normalized internally using GAPDH while liver cDNA qPCR reactions were normalized internally using actin.

2.5.16 RNA Sequencing

RNA libraries were prepared by Novogene using NEBNext adaptors followed by paired end 2x150 sequencing on their Illumina Platform. FASTQ files were trimmed using Trimmomatic v0.39 [61] and aligned using RSEM v1.2.4 [62] against the human genome 18 reference transcriptome. RSEM .genes output files were used for Ebseq EBMultiTest multiple comparison analysis [63]. Gene lists associated with individual EBMultiTest patterns were further analyzed with GSEA 2 [64,65].

2.5.17 MNase Accessibility Assay

$6x10^6$ HCT116 cells were resuspended in 1 ml of digestion buffer (50 mM Tris-HCl pH 7.6, 1 mM $CaCl_2$, and 0.2% Triton X-100) in addition to 15 unites of Worthington MNase. MNase treated cell suspensions were incubated for 5 minutes at 37^{o}C shaking at 400 rpm. MNase digestions were stopped via the addition of EDTA to a final concentration of 5 mM. Digested cells were then pooled and lysed at 4^{o}C using a Covaris® S220 Focused-ultrasonicator with the following settings: Peak Power = 75, Duty Factor = 5, Cycles/Burst = 100, Duration = 30” on/30” off x2. Insoluble debris was pelleted via centrifugation at 10,000 rpm for 10 minutes at 4^{o}C after which the supernatant was transferred to a new tube. 150 μl of digested chromatin was treated with 2 μl of Thermo Fisher Scientific Proteinase K for 90 minutes at 55^{o}C. DNA was then purified using the QIAquick PCR Purification Kit. Next, 1 μg of purified DNA was separated on a 2% agarose gel and quantified using GelAnalyzer 2010a.

2.5.18 Immunoblotting and Image Quantification

Protein separated on SDS-PAGE gels were transferred onto 0.2 μm nitrocellulose membrane and stained with 5 ml of LI-COR REVERT Total Protein Stain for 5 minutes at room temperature before being blocked in 0.1% fat-free milk PBS pH 7.4 for 1 hour. Primary antibodies were diluted 1:1000 in 5% fat-free milk PBST pH 7.4 and incubated with the membrane overnight at 4^{o}C. LI-COR secondary antibodies were used at a 1:15,000 dilution in 5% fat-free milk PBST pH 7.4 and incubated with the membrane for 1 hour at room temperature. Membranes were imaged using an Odyssey Infrared Imager (model no. 9120). Densitometry was performed using Image Studio™ Lite software. All data was normalized to REVERT™ Total Protein Stain.

2.5.19 In vivo Tests

For glucose tolerance tests, mice were fasted overnight for 16 hours and then injected with glucose (1 g/kg) intraperitoneally as previously described [66]. Glucose measurements were taken using a Bayer Contour blood glucose meter and test strips. Mouse body composition was determined using an EchoMRI Body Composition Analyzer (EchoMRI^{TM}, Houston, TX, USA) according to the manufacturer's procedures.

2.5.20 Recombinant Protein Purification

The *H. sapiens* EHMT1 catalytic subunit *E. coli* expression plasmid used in this study (Addgene plasmid # 51314) was acquired from addgene, made possible through a gift by Cheryl Arrowsmith. The *H. sapiens* EHMT2 catalytic subunit *E. coli* expression plasmid used in this study was provided by the laboratory of Peter W. Lewis at the University of Wisconsin-Madison.

Transformed Rosetta™ *E. coli* competent cells were cultured in 1L of 2XYT media at 37°C to an O.D. 600 of 0.8. IPTG was then added to each culture at a final concentration of 1mM. Cultures were allowed to grow for 16 hours at 18°C before being harvested and stored at -80°C. Pellets were resuspended in 30ml Buffer A (50 mM NaPi, 250 mM NaCl, 10mM imidazole, pH 7.8) and sonicated on ice in the presence of lysozyme. Lysate was centrifugated at 45,000xg for 45 min and the supernatant was collected. The supernatant was then loaded onto a HisTrap FF nickel column in line with a GE AKTA FPLC. Protein was eluted off the column using a linear gradient ending in 100% Buffer B (50 mM NaPi, 250 mM NaCl, 250 mM imidazole, pH 7.8) and collected into time-dependent fractions. Fractions were analyzed by coomassie staining of SDS-PAGE gels to assess purity.

Fractions determined to contain the protein of interest were pooled and dialyzed overnight at 4°C in 4 L of HMT dialysis buffer (20 mM HEPES pH 7.5, 300 mM NaCl, 1 mM TCEP, 10% Glycerol). Following dialysis, precipitated protein was pelleted via centrifugation at 4°C for 10 min at 18,000xg and the supernatant was collected. Protein concentration determined via A280 absorbance values and extinction coefficient correction. Final protein samples were aliquoted into single-use 0.2 ml PCR tubes and flash frozen in liquid nitrogen prior to long-term storage at -80°C.

2.5.21 Histone Methyltransferase Activity Assay

The methyltransferase activity of recombinantly purified EHMT1 and EHMT2 catalytic subunits was assessed using Promega Corporation's MTase-Glo™ Methyltransferase Assay. Assays were performed using 12.5 nM enzyme in the presence of saturating concentrations of SAM (30 μM) and unmodified H3K9 peptide (30 μM, WARTKQTARKSTGGKAPR – 3') as

well as either saturating levels of UNC0642 (5 μM) or 0.1% DMSO. Reactions proceeded for 1 hour at 30°C before addition of MTase-Glo™ reagent following the Promega protocol. Luminescence was detected using a Biotek Synergy H4 Hybrid plate reader. All values detected were determined to be within the instrument's linear range of detection via the use of a SAH standard curve. To test for reversibility of enzyme inhibition by small molecule, 1 μM EHMT1 and EHMT2 were incubated with saturating concentrations of UNC0642 (5 μM) or 0.1% DMSO followed overnight 1,000x or 10,000x dialysis with a molecular weight cutoff of 10,000 Da against 1x Reaction Buffer without BSA (20mM Tris, pH 8.0, 50mM NaCl, 1mM EDTA, 3mM $MgCl_2$, 1mM DTT). Following dialysis, enzyme and reaction components were diluted using the appropriate dialysis buffers to the working concentrations described above. The MTase-Glo™ assay was then repeated using identical conditions as described above.

2.5.22 Quantification and Statistical Analysis

Explanations of statistical analyses and parameters are present in figure legends as well as in 'Experimental Procedures" where appropriate. Dixon's Q test for statistical outliers was used as exclusion criteria.

2.5.23 Data and Software Availability

RNA-sequencing as well as H3K9me1 and H3K9me3 ChIP-sequencing data have been uploaded to Gene Expression Omnibus (GEO). GEO accession numbers are available in section 2.5.24.

2.5.24 Key Resources

REAGENT or RESOURCE	SOURCE	IDENTIFIER
Antibodies		
Rabbit polyclonal anti-H3K9me1	Abcam	Cat#ab176880; RRID#AB_2751009
Rabbit polyclonal anti-H3K9me3	Abcam	Cat#ab8898; RRID#AB_306848
Rabbit polyclonal anti-Histone H3	Abcam	Cat#ab46765; RRID#AB_880439
Rabbit monoclonal anti-alpha Tubulin	Cell Signaling Technologies	Cat#cst2125; RRID#AB_2619646
IRDye® 800CW Goat anti-Rabbit	LI-COR Biosciences	Cat#925-32211; RRID#AB_2651127
Chemicals, Peptides, and Recombinant Proteins		
UNC0642 G9a/GLP Inhibitor	R&D Systems	Cat#5132/10
DNA Degradase Plus	Zymo Research	Cat#E2020
Lipofectamine RNAiMax	Thermo Fisher	Cat#13778030
L-Lysine-2HCl	Thermo Fisher Scientific	Cat#PI89987
L-Arginine-HCl 13C6 15N4	Thermo Fisher	Cat#PI89990
Dimethyl Sulfoxide (DMSO)	Sant Cruz Biotechnology	Cat#sc-358801

Sequencing Grade Modified Trypsin	Promega	Cat#V5113
Propionic Anhydride	Sigma-Aldrich	Cat#240311
Phenyl Isocyanate	Sigma-Aldrich	Cat#78750-25ML
Leupeptin Hemisulfate	Thermo Fisher	Cat#AAJ61188MC
Aprotinin	Gold Biotechnology	Cat#A-655-100
Phenylmethylsulfonyl Fluoride (PMSF)	Gold Biotechnology	Cat#P-470-50
Trichostatin A	Thermo Fisher	Cat#501012404
Sodium Butyrate	Sigma-Aldrich	Cat#303410-100G
Nicotinamide	Sigma-Aldrich	Cat#N3376-500G
Urea	Acros Organics	Cat#197460050
Dithiothreitol (DTT)	Gold Biotechnology	Cat#DTT100
Iodoacetamide	Sigma-Aldrich	Cat#I1149-5G
Ammonium Bicarbonate	Sigma-Aldrich	Cat#09830-500G
Micrococcal Nuclease (MNase)	Worthington Biochemical	Cat#LS004798
Proteinase K	Thermo Fisher	Cat#EO0491
TRIzol™	Thermo Fisher	Cat#15596018
TRI Reagent	Sigma-Aldrich	Cat#T9424-25ML

3M Empore C18 47mm extraction disks	Empore	Cat#2215
Atlantis dC18 NanoEase Column (3 μM, 100 μM, 150 mm)	Waters	Cat#186002209
XBridge BEH Amide Column (3.5 μM, 2.1 mm, 150mm)	Waters	Cat#186004860
Superscript III Reverse Transcriptase	Thermo Fisher	Cat#18080044
RPMI-1640	Thermo Fisher	Cat#11875119
RPMI-1640 for SILAC	Thermo Fisher	Cat#88365
RPMI-1640, no methionine	Thermo Fisher	Cat#A1451701
Fetal Bovine Serum (FBS)	Thermo Fisher	Cat#16000044
Dialyzed Fetal Bovine Serum (DFBS)	Thermo Fisher	Cat#88212
H3K9 unmodified peptide	This paper	N/A
pET28a-LIC-4H4H	Addgene	Plasmid # 51314; RRID#Addgene_51314
pET28a-LIC-EHMT2-913-1193	Peter W. Lewis Laboratory	N/A
Critical Commercial Assays		
PerfeCTa SYBR® Green SuperMix	Quanta Bio	Cat#95054-02K
SYBR Green PCR Master Mix	Thermo Fisher	Cat#4309155
REVERT Total Protein Stain	LI-COR Biosciences	Cat#926-11011

RevertAid First Strand cDNA Synthesis Kit	Thermo Fisher	Cat#K1621
Wizard® Genomic DNA Purification Kit	Promega	Cat#A1120
Dynabeads™ M-280 Sheep Anti Rabbit IgG	Thermo Fisher	Cat#11203D
QIAquick PCR Purification Kit	QIAGEN	Cat#28104
TruSeq DNA Nano	Illumina	Cat#20015964
Axygen™ Light Cycler 480 Compatible PCR Plates	Thermo Fisher	Cat#14-223-212
Promega MTase-Glo™	Promega	Cat#V7602
Deposited Data		
H3K9me1 and H3K9me3 ChIP-sequencing Data	This paper	GEO Accession Number: GSE122565
RNA-sequencing Data	This paper	GEO Accession Number: GSE138574
Experimental Models: Cell Lines		
H. sapiens: HCT116	ATCC	CCL-247
H. sapiens: HEK-293T	ATCC	CRL-3216
H. sapiens: HEK-293	ATCC	CRL-1573
H. sapiens: HepG2	ATCC	HB-8065
H. sapiens: MCF7	ATCC	HTB-22
H. sapiens: Panc1	ATCC	CRL-1469

M. musculus: Hepa-1c1c7	ATCC	CRL-2026
Experimental Models: Organisms/Strains		
M. musculus: C57BL/6J (9-weeks of age)	The Jackson Laboratory	JAX: 000664
M. musculus: C57BL/6J (2- and 18-months of age)	The National Institute on Aging Rodent Colony	N/A
Oligonucleotides		
5-Methylcytosine and 5-Hydroxymethylcytosine DNA	Zymo Research	Cat#D505
Stealth RNAi Sense Sequence: *H. sapiens* MATIIα: 5′AUCAAGGACAGCAUCACUGAUUUGG-3′	Thermo Fisher	Kera et al., 2013
Stealth RNAi Sense Sequence: Control: 5′-AGGAGGAUAUUACCAUGGACAAGAC-3′	Thermo Fisher	Kera et al., 2013
SUV39H1 RNAi: *H. sapiens*	Novus Biologicals	H00006839-R01-20nmol

SUV39H2 RNAi: *H. sapiens*	Novus Biologicals	H00079723-R01-20nmol
SETDB1 RNAi: *H. sapiens*	Novus Biologicals	H00009869-R01-20nmol
G9a/EHMT2 RNAi: *H. sapiens*	Novus Biologicals	H00010919-R02-20nmol
GLP/EHMT1 RNAi: *H sapiens*	Novus Biologicals	H00079813-R01-20nmol
RT-qPCR Primers	See Table 2-1	See Table 2-1
Software and Algorithms		
Bowtie2-2.1.0	Langmead and Salzberg, 2012	http://bowtie-bio.sourceforge.net/bowtie2/index.shtml
Samtools 1.5	Li et al., 2009	http://samtools.sourceforge.net/
MACS2-2.1.1.20160309	Zhang et al., 2008	http://liulab.dfci.harvard.edu/MACS/
Bedtools v2.25.0	Quinlan and Hall, 2010	https://bedtools.readthedocs.io/en/latest/
HOMER v4.9	Heinz et al., 2010	http://homer.ucsd.edu/homer/
GelAnalyzer 2010a	Lazar Software	http://gelanalyzer.com/index.html

MAVEN	Melamud et al., 2010; Clasquin et al., 2012	http://genomics-pubs.princeton.edu/mzroll/index.php
MAXQUANT	Cox et al., 2014	http://www.biochem.mpg.de/5111795/maxquant
Trimmomatic v0.39	Bolger et al., 2014	http://www.usadellab.org/cms/?page=trimmomatic
RSEM v1.2.4	Li et al., 2011	https://deweylab.github.io/RSEM/
EBSeq v1.24.0	Leng et al., 2013	http://bioconductor.org/packages/release/bioc/html/EBSeq.html
GSEA 2	Tamayo et al., 2005 Mootha et al., 2003	http://software.broadinstitute.org/gsea/index.jsp
Skyline	MacLean et al., 2010	https://skyline.ms/project/home/software/Skyline/begin.view
Other		
Control *M. musculus* Diet	Envigo	TD.01084
Methionine Deficient *M. musculus* Diet	Envigo	TD.140119

Table 2-1: Quantitative PCR Primer Sequences. DNA sequences and references for primers used in Chapter 2.

Gene	Species	Forward primer	Reverse primer	Ref.
GAPDH	*H. Sapiens*	CGAGATCCCTCCAAAATCAA	CATGAGTCCTTCCACGATACCAA	[9]
HERV-K	*H. Sapiens*	GGCCATCAGAGTCTAAACCACG	CTGACTTTCTGGGGGTGGCCG	[67]
HERV-R	*H. Sapiens*	CATGGGAAGCAAGGGAACT	CTTTCCCCAGCGAGCAATAC	[68]
LINE 1	*H. Sapiens*	ACAGCTTTGAAGAGAGCAGTGGTT	AGTCTGCCCGTTCTCAGATCT	[67]
G9a	*H. Sapiens*	GCAAGGCCAAGAAGAAATGGCGAA	TCTCGCTGATGCGGTCAATCTT	[69]
Glp	*H. Sapiens*	GACATCAACATCCGAGACAA	GAAAGAAAGAGGACGACACAG	[70]
SUV39H1	*H. Sapiens*	GCTAGGCCCGAATGTCGTTA	GCCTTCTGCACCAGGTAGTT	[71]
SUV39H2	*H. Sapiens*	GTGTGTGCCTTGCCTAGTTTCACT	CTGTCCTCGTCTTTCAGCTTCTTCAC	[69]
SETDB1	*H. Sapiens*	GGGCAAGGGTGTTTTCATTAAC	GTTAGTTGATGGCAGGCACACTT	[72]
ACTB	*M. Musculus*	ACCTTCTACAATGAGCTGCG	CTGGATGGCTACGTACATGG	[23]
SINE B1	*M. Musculus*	CAGCATTTAGGAGGCAGAGG	TCCAGGAGCTACTTTGTAAACC	[73]
SINE B2	*M. Musculus*	TGAAAAGGGCTGGTGAGATG	TGCTGGGATTTGAACTCTGG	[73]
LINE 1	*M. Musculus*	GAAAGGACCCAGATGTAGCTG	TGAAGATCCCTTTAGCTCCTTG	[74]

2.6 Acknowledgements

This research was supported in part by grants from the NIH (S.A.H. – T32 DK007665; K.A.K. – T32 DK007665; W.H.L. – T32 DK007665, F32 GM128399; R.S. – GM113033; B.P.T. – R01 GM094314; C.Y. – K99 GM129415; J.M.D. – R37 GM059785; D.W.L. – AG041765, AG050135, AG051974, AG056771, AG062328), grants-in-aid from the Japan Society for the Promotion of Science (K.I. – 18H05374), a UW-Madison SCRMC postdoctoral fellowship (C.K.W.), a New Investigator Program Award (D.W.L.) and a Collaborative Health Sciences Program Award (V.L.C.) from the Wisconsin Partnership Program, the V Foundation for Cancer Research (V.L.C.), and a Glenn Foundation Award for Research in the Biological Mechanisms of Aging (D.W.L.), as well as startup funds from the UW-Madison School of Medicine and Public Health and the UW-Madison Department of Medicine (V.L.C. and D.W.L.). This research was conducted while D.W.L. was an AFAR Research Grant recipient from the American Federation for Aging Research. D.Y. was supported in part by a fellowship from the American Heart Association (17PRE33410983). The Lamming laboratory is supported in part by the U.S. Department of Veterans Affairs (I01-BX004031), and this work was supported using facilities and resources from the William S. Middleton Memorial Veterans Hospital. This work does not represent the views of the Department of Veterans Affairs or the United States Government. We would like to thank Alexis J. Lawton for the bioinformatics analysis presented in Figure S3I. We would also like to thank the University of Wisconsin-Madison Biotechnology Center and the University of Wisconsin-Madison Center for High Throughput Computing for their help in generating and analyzing the ChIP-sequencing data presented in Figure 5, respectively.

2.7 References

1. Fan, J. et al. (2015) Metabolic regulation of histone post-translational modifications. *ACS Chem. Biol.* 10, 95–108.
2. Li, X. et al. (2018) Regulation of chromatin and gene expression by metabolic enzymes and metabolites. *Nature Reviews Molecular Cell Biology*. 19, 563–578.
3. Ducker, G. S. & Rabinowitz, J. D. (2017) One-Carbon Metabolism in Health and Disease. *Cell Metab.* 25, 27–42.
4. Sanderson, S. M. et al. (2019) Methionine metabolism in health and cancer: a nexus of diet and precision medicine. *Nat. Rev. Cancer.* 19, 625–637.
5. Ding, W. et al. (2015) s-Adenosylmethionine Levels Govern Innate Immunity through Distinct Methylation-Dependent Pathways. *Cell Metab.* 22, 633–645.
6. Hayashi, T. et al. (2018) S-Adenosylmethionine Synthetase Is Required for Cell Growth, Maintenance of G0 Phase, and Termination of Quiescence in Fission Yeast. *iScience* 5, 38–51.
7. Kera, Y. et al. (2013) Methionine Adenosyltransferase II-dependent Histone H3K9 Methylation at the COX-2 Gene Locus. *J. Biol. Chem.* 288, 13592–13601.
8. Mentch, S. J. et al. (2015) Histone Methylation Dynamics and Gene Regulation Occur through the Sensing of One-Carbon Metabolism. *Cell Metab.* 22, 861–873.
9. Shiraki, N. et al. (2014) Methionine Metabolism Regulates Maintenance and Differentiation of Human Pluripotent Stem Cells. *Cell Metab.* 19, 780–794.
10. Shyh-Chang, N. et al. (2013) Influence of Threonine Metabolism on S-Adenosylmethionine and Histone Methylation. *Science.* 339, 222–226.

11. Strekalova, E. et al. (2019) S-adenosylmethionine biosynthesis is a targetable metabolic vulnerability of cancer stem cells. *Breast Cancer Res. Treat.* 175, 39–50.
12. Tang, S. *et al.* Methionine metabolism is essential for SIRT1-regulated mouse embryonic stem cell maintenance and embryonic development. *The EMBO Journal* **36**, 3175–3193 (2017).
13. Towbin, B. D. et al. (2012) Step-Wise Methylation of Histone H3K9 Positions Heterochromatin at the Nuclear Periphery. *Cell.* 150, 934–947.
14. Ye, C. et al. (2017) A Metabolic Function for Phospholipid and Histone Methylation. *Mol. Cell.* 66, 180-193.
15. Farmer, B. (2014) Nutritional adequacy of plant-based diets for weight management: observations from the NHANES. *Am. J. Clin. Nutr.* 100, 365S-368S.
16. Schmidt, J. A. et al. (2016) Plasma concentrations and intakes of amino acids in male meat-eaters, fish-eaters, vegetarians and vegans: a cross-sectional analysis in the EPIC-Oxford cohort. *Eur. J. Clin. Nutr.* 70, 306–312.
17. Krishnaiah, S. Y. et al. (2017) Clock Regulation of Metabolites Reveals Coupling between Transcription and Metabolism. *Cell Metab.* 25, 961-974.
18. Brown-Borg, H. M. et al. (2018) Metabolic adaptation of short-living growth hormone transgenic mice to methionine restriction and supplementation. *Annals of the New York Academy of Sciences.* 1418, 118–136.
19. Green, C. L. & Lamming, D. W. (2019) Regulation of metabolic health by essential dietary amino acids. *Mechanisms of Ageing and Development.* 177, 186–200.
20. Lees, E. K. et al. (2014) Methionine restriction restores a younger metabolic phenotype in adult mice with alterations in fibroblast growth factor 21. *Aging Cell.* 13, 817–827.

21. Miller, R. A. et al. (2005) Methionine-deficient diet extends mouse lifespan, slows immune and lens aging, alters glucose, T4, IGF-I and insulin levels, and increases hepatocyte MIF levels and stress resistance. *Aging Cell.* 4, 119–125.
22. Orentreich, N. et al. (1993) A. Low Methionine Ingestion by Rats Extends Life Span. *J. Nutr.* 123, 269–274.
23. Yu, D. et al. (2018) Short-term methionine deprivation improves metabolic health via sexually dimorphic, mTORC1-independent mechanisms. *The FASEB Journal.* 32, 3471–3482.
24. Greer, E. L. & Shi, Y. (2012) Histone methylation: a dynamic mark in health, disease and inheritance. *Nat. Rev. Genet.* 13, 343–357.
25. Liu, F. et al. (2013) Discovery of an in vivo chemical probe of the lysine methyltransferases G9a and GLP. *J. Med. Chem.* 56, 8931–8942.
26. Loyola, A. et al. (2006) PTMs on H3 Variants before Chromatin Assembly Potentiate Their Final Epigenetic State. *Mol. Cell.* 24, 309–316.
27. Pinheiro, I. et al. (2012) Prdm3 and Prdm16 are H3K9me1 Methyltransferases Required for Mammalian Heterochromatin Integrity. *Cell.* 150, 948–960.
28. Bröer, A. et al. (2001) Association of 4F2hc with light chains LAT1, LAT2 or y+LAT2 requires different domains. *Biochem. J.* 355, 725–731.
29. Loyola, A. et al. (2009) The HP1alpha-CAF1-SetDB1-containing complex provides H3K9me1 for Suv39-mediated K9me3 in pericentric heterochromatin. *EMBO Rep.* 10, 769–775.
30. Peters, A. H. et al. (2001) Loss of the Suv39h histone methyltransferases impairs mammalian heterochromatin and genome stability. *Cell.* 10**7**, 323–337.

31. Bannister, A. J. et al. (2001) Selective recognition of methylated lysine 9 on histone H3 by the HP1 chromo domain. *Nature.* 410, 120–124.

32. Lachner, M. et al. (2001) Methylation of histone H3 lysine 9 creates a binding site for HP1 proteins. *Nature.* 410, 116–120.

33. Rea, S. et al. (2000) Regulation of chromatin structure by site-specific histone H3 methyltransferases. *Nature.* 406, 593–599.

34. Larson, K. et al. (2012) Heterochromatin formation promotes longevity and represses ribosomal RNA synthesis. *PLoS Genet.* 8, e1002473.

35. Ni, Z. et al. (2012) Two SET domain containing genes link epigenetic changes and aging in Caenorhabditis elegans. *Aging Cell.* 11, 315–325.

36. Scaffidi, P. & Misteli, T. (2006) Lamin A-dependent nuclear defects in human aging. *Science.* 312, 1059–1063.

37. Tvardovskiy, A. et al. (2017) Accumulation of histone variant H3.3 with age is associated with profound changes in the histone methylation landscape. *Nucleic Acids Res.* 45, 9272–9289.

38. Wood, J. G. et al. (2010) Chromatin remodeling in the aging genome of Drosophila. *Aging Cell.* 9, 971–978.

39. Booth, L. N. & Brunet, A. (2016) The Aging Epigenome. *Mol. Cell* **62**, 728–744.

40. De Cecco, M. et al. (2019) L1 drives IFN in senescent cells and promotes age-associated inflammation. *Nature.* 566, 73–78.

41. De Cecco, M. et al. (2013) Genomes of replicatively senescent cells undergo global epigenetic changes leading to gene silencing and activation of transposable elements. *Aging Cell.* 12, 247–256.

42. Oberdoerffer, P. & Sinclair, D. A. (2007) The role of nuclear architecture in genomic instability and ageing. *Nat. Rev. Mol. Cell Biol.* 8, 692–702.

43. Wood, J. G. et al. (2016) Chromatin-modifying genetic interventions suppress age-associated transposable element activation and extend life span in Drosophila. *Proc. Natl. Acad. Sci. U.S.A.* 113, 11277–11282.

44. Zee, B. M. et al. (2010) In vivo residue-specific histone methylation dynamics. *J. Biol. Chem.* 285, 3341–3350.

45. Mostoslavsky, R. et al. (2006) Genomic instability and aging-like phenotype in the absence of mammalian SIRT6. *Cell.* 124, 315–329.

46. Simon, M. et al. (2019) LINE1 Derepression in Aged Wild-Type and SIRT6-Deficient Mice Drives Inflammation. *Cell Metab.* 29, 871-885.

47. Van Meter, M. et al. (20140 SIRT6 represses LINE1 retrotransposons by ribosylating KAP1 but this repression fails with stress and age. *Nat. Commun.* 5, 5011.

48. Flurkey, K. et al. (2007) The mouse in aging research. In The Mouse in Biomedical Research, 2nd Edition, J.G. Fox, ed. (Elsevier), pp. 637–671.

49. Wu, S. E. (1983) Chiral instability at sulfur of S-adenosylmethionine. *Biochemistry.* 22, 2828–2832.

50. Katoh, Y. et al. (2011) Methionine Adenosyltransferase II Serves as a Transcriptional Corepressor of Maf Oncoprotein. *Mol. Cell.* 41, 554–566.

51. Li, S. et al. (2015) Serine and SAM Responsive Complex SESAME Regulates Histone Modification Crosstalk by Sensing Cellular Metabolism. *Mol. Cell.* 60, 408–421.

52. Clasquin, M. F. et al. (2012) LC-MS data processing with MAVEN: a metabolomic analysis and visualization engine. *Curr. Protoc. Bioinformatics.* Chapter 14, Unit14.11.

53. Melamud, E. et al. (2010) Metabolomic analysis and visualization engine for LC-MS data. *Anal. Chem.* 82, 9818–9826.

54. MacLean, B. et al. (2010) Skyline: an open source document editor for creating and analyzing targeted proteomics experiments. *Bioinformatics*. 26, 966–968.

55. Cox, J. et al. (2014) Accurate proteome-wide label-free quantification by delayed normalization and maximal peptide ratio extraction, termed MaxLFQ. *Mol. Cell. Proteomics.* 13, 2513–2526.

56. Langmead, B. & Salzberg, S. L. (2012) Fast gapped-read alignment with Bowtie 2. *Nat. Methods.* 9, 357–359.

57. Li, H. et al. (2009) The Sequence Alignment/Map format and SAMtools. *Bioinformatics.* 25, 2078–2079.

58. Zhang, Y. et al. (2008) Model-based analysis of ChIP-Seq (MACS). *Genome Biol.* 9, R137.

59. Quinlan, A. R. & Hall, I. M. (2010) BEDTools: a flexible suite of utilities for comparing genomic features. *Bioinformatics.* 26, 841–842.

60. Heinz, S. et al. (2010) Simple Combinations of Lineage-Determining Transcription Factors Prime cis-Regulatory Elements Required for Macrophage and B Cell Identities. *Mol. Cell.* 38, 576–589.

61. Bolger, A. M. et al. (2014) Trimmomatic: a flexible trimmer for Illumina sequence data. *Bioinformatics.* 30, 2114–2120.

62. Li, B. & Dewey, C. N. (2011) RSEM: accurate transcript quantification from RNA-Seq data with or without a reference genome. *BMC Bioinformatics.* 12, 323.

63. Leng, N. et al. (2013) EBSeq: an empirical Bayes hierarchical model for inference in RNA-seq experiments. *Bioinformatics.* 29, 1035–1043.

64. Mootha, V. K. et al. (2003) PGC-1alpha-responsive genes involved in oxidative phosphorylation are coordinately downregulated in human diabetes. *Nat. Genet.* 34, 267–273

65. Subramanian, A. et al. (2005) Gene set enrichment analysis: a knowledge-based approach for interpreting genome-wide expression profiles. *Proc. Natl. Acad. Sci. U.S.A.* 102, 15545–15550.

66. Arriola Apelo, S. I. et al. (2016) Alternative rapamycin treatment regimens mitigate the impact of rapamycin on glucose homeostasis and the immune system. *Aging Cell.* 15, 28–38.

67. Klawitter, S. et al. (2016) Reprogramming triggers endogenous L1 and Alu retrotransposition in human induced pluripotent stem cells. *Nat. Commun.* 7, 10286.

68. Rhyu, D.-W. et al. (2014) Expression of human endogenous retrovirus env genes in the blood of breast cancer patients. *Int. J. Mol. Sci.* 15, 9173–9183.

69. Mauger, O. et al. (2015) Alternative splicing regulates the expression of G9A and SUV39H2 methyltransferases, and dramatically changes SUV39H2 functions. *Nucleic Acids Res.* 43, 1869–1882.

70. Northcott, P. A. et al. (2009) Multiple recurrent genetic events converge on control of histone lysine methylation in medulloblastoma. *Nat. Genet.* (2009) 41, 465–472.

71. Watson, G. W. et al. (2014) SUV39H1/H3K9me3 attenuates sulforaphane-induced apoptotic signaling in PC3 prostate cancer cells. *Oncogenesis.* 3, e131.

72. Fei, Q. et al. (2015) Histone methyltransferase SETDB1 regulates liver cancer cell growth through methylation of p53. *Nat. Commun.* 6, 1–12.

73. Kang, Y. K. et al. (1999) Efficient integration of short interspersed element-flanked foreign DNA via homologous recombination. *J. Biol. Chem.* 274, 36585–36591.

74. Hardies, S. C. et al. (2000) LINE-1 (L1) lineages in the mouse. *Mol. Biol. Evol.* 17, 616–628.

Chapter 3: Development of Radiometric EZ-Tip Assay

Spencer A. Haws[1,2] and John M. Denu[1,2]

[1]Wisconsin Institute for Discovery, University of Wisconsin-Madison
[2]Department of Biomolecular Chemistry, SMPH, University of Wisconsin-Madison

*Results presented here are unpublished at time of thesis deposition.

3.1 Abstract

Histone methylation controls diverse aspects of chromatin biology under both healthy and diseased states. Therefore, great interest exists to uncover the catalytic properties of histone methyltransferases and develop a better understanding of the factors that regulate their activities. The EZ-Tip assay detailed here offers a quantitative, endpoint assay that directly measures HMT product formation using radiolabeled S-adenosylmethionine and C18 StageTip spin columns. The method marks an improvement over current radiometric assays due to its greater throughput, ability to accommodate diverse protein loads, and lower associated costs.

3.2 Introduction

Radiometric assays have long been the gold standard for assessing methyltransferase activity due to their extraordinary sensitivity and ability to directly quantify methylated product formation. Traditional radiometric assays leverage the cation exchange properties of P81 phosphocellulose membrane to facilitate the separation of radiolabeled S-adenosylmethionine (SAM) from proteinaceous assay components [1,2]. Although effective, limited P81 phosphocellulose availability as a result of ceased commercial production has created the need for an alternative approach.

It has recently been shown C18 reversed-phase resin-filled pipette tips (ZipTips®) can be used as a P81 alternative due to their hydrophobic properties that facilitate the binding and retention of proteinaceous material but not SAM, a polar molecule [3,4]. ZipTips® however come with their own limitations including a fixed resin capacity, laborious pipetting, and high-associated costs. In the proteomics field these limitations have been addressed through the introduction of StageTips – spin columns easily made from pipette tips and C18 solid-phase extraction (SPE) discs [5]. Advantages of StageTips include their ability to accommodate diverse protein capacities, relatively high throughput, and low associated costs. Here, we repurpose StageTips for the separation of radiolabeled SAM from proteinaceous material as a core component of the EZ-Tip (Enzyme Tip) assay: a simple, reliable methyltransferase assay with comparable sensitivity to P81-dependent methods.

While EZ-Tip has been optimized for the separation of radiolabeled SAM from histone H3 peptide, the general principles can be readily adapted to assess the *in vitro* activity of non-histone methyltransferases [6] as well as other enzymes that utilize polar cofactors such as

protein kinases [7,8]. This significantly broadens the protocol's usefulness beyond the fields of chromatin biology and biochemistry.

3.3 Development and Optimization

3.3.1 Wash Volumes

Efficient separation of residual [methyl-^{3}H] SAM from histone peptide substrate is critical for maximizing EZ-Tip sensitivity. When $1x10^3$ picomoles of acidified SAM are initially loaded onto a StageTip containing two C18 SPE discs, the majority (~70%) pass directly through (data not shown). This confirms the low affinity of C18 SPE discs for SAM, suggesting an aqueous solution may be sufficient in removing the residual [methyl-^{3}H] SAM. Using an aqueous wash solution (H_2O + 0.5% Formic Acid) is advantageous as washing with organic solvents would introduce risk of prematurely eluting proteinaceous assay components by disrupting their hydrophobic interactions with the C18 SPE discs.

Four wash volumes (i.e., 50 µl, 100 µl, 200 µl, and 400 µl) were tested for their ability to remove the remaining C18 SPE disc bound [methyl-^{3}H] SAM. Optimizing wash volume is critical to *1.)* limit opportunities for proteinaceous components to prematurely elute and *2.)* minimize the amount of materials consumed per reaction. As wash volumes increased there was a corresponding increase in [methyl-^{3}H] SAM detected in the flowthrough, up to 200 µl (Figure 3-1A). [methyl-^{3}H] SAM in the flowthrough was lowest for the largest wash volume of 400 µl (Figure 3-1A). This result was unexpected as a the 400 µl wash was performed as 2 x 200 µl washes due to a limited StageTip volume capacity of 200 µl. Therefore, the 400 µl wash should minimally have been as effective as the 200 µl wash. However, variability between replicates across all washes limited the ability to directly compare wash efficiency by measuring flowthrough [methyl-^{3}H] SAM CPM units.

Next, an organic solvent solution (80% ACN + 0.5% Formic Acid) was used to elute any remaining [methyl-^{3}H] SAM from the C18 SPE discs following all four wash volumes.

Measuring [methyl-^{3}H] SAM CPM units in the eluate provides insight into final assay background signal as all histone peptide substrate would also elute at this stage. Eluate [methyl-^{3}H] SAM CPM units were much more consistent across replicates compared to wash flowthrough measurements, revealing a 200 µl wash is the minimum volume required to remove the greatest amount of non-specific [methyl-^{3}H] SAM signal (Figure 3-1B). 200 µl and 400 µl washes resulted in statistically similar eluate signal, 0.13% and 0.11% of initial [methyl-^{3}H] SAM CPM units present, respectively. These background levels were roughly 4-fold lower than those following a 50 µl wash and 2-fold lower than those following a 100 µl wash (Figure 3-1B). Therefore, these data show that 200 µl of wash solution is the most efficient volume for removal of residual [methyl-^{3}H] SAM from C18 SPE discs, providing assay sensitivity down to ~0.1% substrate turnover.

Figure 3-1: Wash Volume Optimization for EZ-Tip Assay. (*A*) Percent of CPM from a [methyl-^{3}H] SAM-only mock reaction detected following four unique wash volumes. (*B*) Percent of CPM from a [methyl-^{3}H] SAM-only mock reaction detected in 100 µl acetonitrile-based eluate following each unique wash volume. Mock reaction details prior to acidification – Volume = 20 µl; SAM [c] = 50 µM; [methyl-^{3}H] SAM CPM = ~1x10^{5}. Mock reactions acidified with 10 µl 6% TFA prior to StageTip loading. n = 3; error bars represent SD. *p < 0.05.

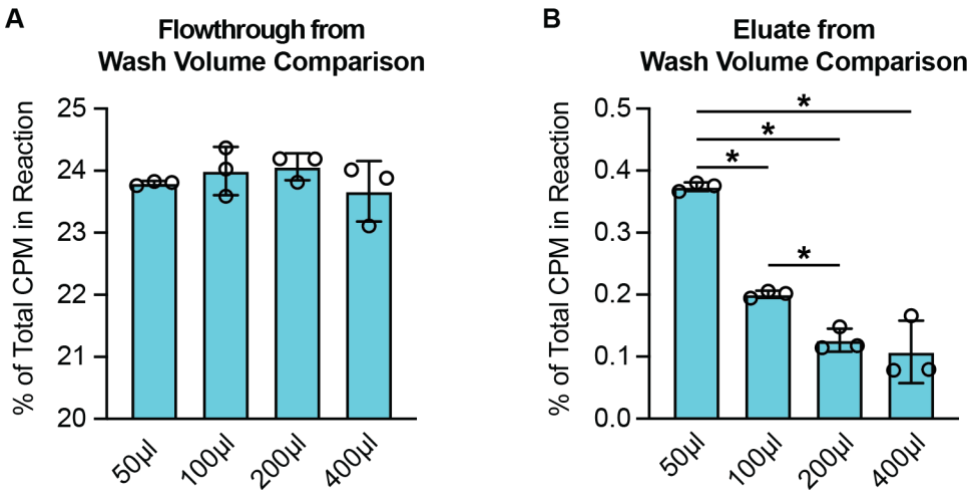

3.3.2 Reaction Buffer

The greatest differentiating factor across published HMT activity assay buffers is the presence or absence of detergent. For example, the activity assay buffer used by Hassani et al., 2012 includes 0.01% Triton X-100 while the buffer used by Jayaram et al., 2016 has no detergent present [9,10]. To determine if a low concentration of detergent has a significant impact on HMT activity, possibly by minimizing non-specific protein-substrate interactions and/or general protein aggregation, an EHMT2 H3K9un saturation curve was generated using buffer containing either 0.01% Triton X-100 or no detergent. Both buffers shared the following components: 50 mM HEPES (pH 7.9), 2 mM $MgCl_2$, 0.5 mM dithiothreitol, and 0.1 mM AEBSF. Interestingly, EHMT2 + 0.01% Triton X-100 possessed a k_{cat} of 15.61 min^{-1}, nearly 3-fold greater than in the absence of detergent (k_{cat} = 5.88 min^{-1}) (Figure 3-2A). In addition to a greater k_{cat}, detergent also significantly decreased the EHMT2 $K_{m,\ H3K9un}$ from 12.72 μM to 2.08 μM (Figure 3-2A). As a result, the catalytic efficiency of EHMT2 increased greater than 10-fold from 0.46 min^{-1} μM^{-1} to 7.5 min^{-1} μM^{-1} (Figure 3-2A). These data suggest the presence of detergent at low concentrations significantly improves HMT catalytic efficiency via improvements in both k_{cat} and K_m. Therefore, 0.01% Triton X-100 is included in the final EZ-Tip reaction buffer.

Figure 3-2: EZ-Tip Reaction Buffer Comparison. (*A*) EHMT2 H3K9un peptide saturation curve using buffers with or without 0.01% Triton X-100. Reaction details – Time = 60 min; Volume = 20 µl; EHMT2 [c] = 25 nM; SAM [c] = 50 µM; [methyl-^{3}H] SAM CPM = ~100,000. n = 1.

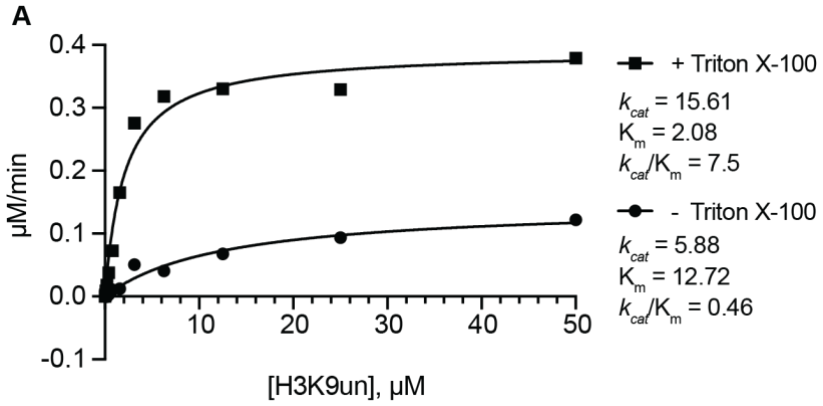

3.3.3 StageTip Peptide Capacity

Empirically calculating the peptide binding capacity of C18 SPE discs is important for ensuring all peptide loaded onto the StageTip is accounted for during downstream data processing. To determine the peptide binding capacity of StageTips packed with two C18 SPE discs, the StageTip eluate CPM units from a broad range of H3K9un peptide concentrations (i.e., 0.5 – 100 μM) containing a fixed concentration of 0.5 μM radiolabeled H3K9 peptide were measured. Peptide concentrations were calculated for a 20 μl volume after which 10 μl of 6% TFA was added to mimic the composition of a quenched EZ-Tip reaction. With all peptide concentrations containing identical amounts of radiolabeled peptide, it is possible to directly compare binding efficiency by evaluating CPM units measured in StageTip eluates.

A simple linear regression analysis fit a line with a $R^2 = .958$ to a plot of CPM units measured from all peptide concentration eluates, suggesting peptide binding efficiency decreases linearly as H3K9un concentration increases (Figure 3-3A). This R^2 value appeared to be largely dictated by peptide concentrations ranging from 10 μM to 100 μM. A simple linear regression analysis fit a line with a $R^2 = 0.004$ for H3K9un concentrations ranging from 0.5 μM to 10 μM while the same analysis for peptide concentrations ranging from 10 μM to 100 μM produced a fit of $R^2 = 0.977$ (Figure 3-3B, 3-3C). Therefore, a StageTip packed with two C18 SPE discs can retain peptide concentrations up to 10 μM (in a 20 μl volume prior to acidification) with equal efficiency. However, if the peptide concentration of a 20 μl reaction exceeds 10 μM, peptide binding efficiency decreases linearly up to 100 μM. Because this loss in peptide binding efficiency is linear, the equation derived using the linear regression analysis from 10 μM to 100 μM can be used to generate reliable correction factors, allowing for accurate calculations of kinetic constants during downstream data processing.

Figure 3-3: Analysis of StageTip Peptide Capacity. (*A-C*) Scatter plots depicting CPM units of eluates for eight unique H3K9un peptide concentrations. Peptide concentrations were calculated for 20 µl prior to acidification. Equal CPM units (from 0.5 µM [methyl-^{3}H] SAM methylated H3K9un peptide) were present in all H3K9un peptide dilutions prior to StageTip cleanup. n = 3; error bars represent SD.

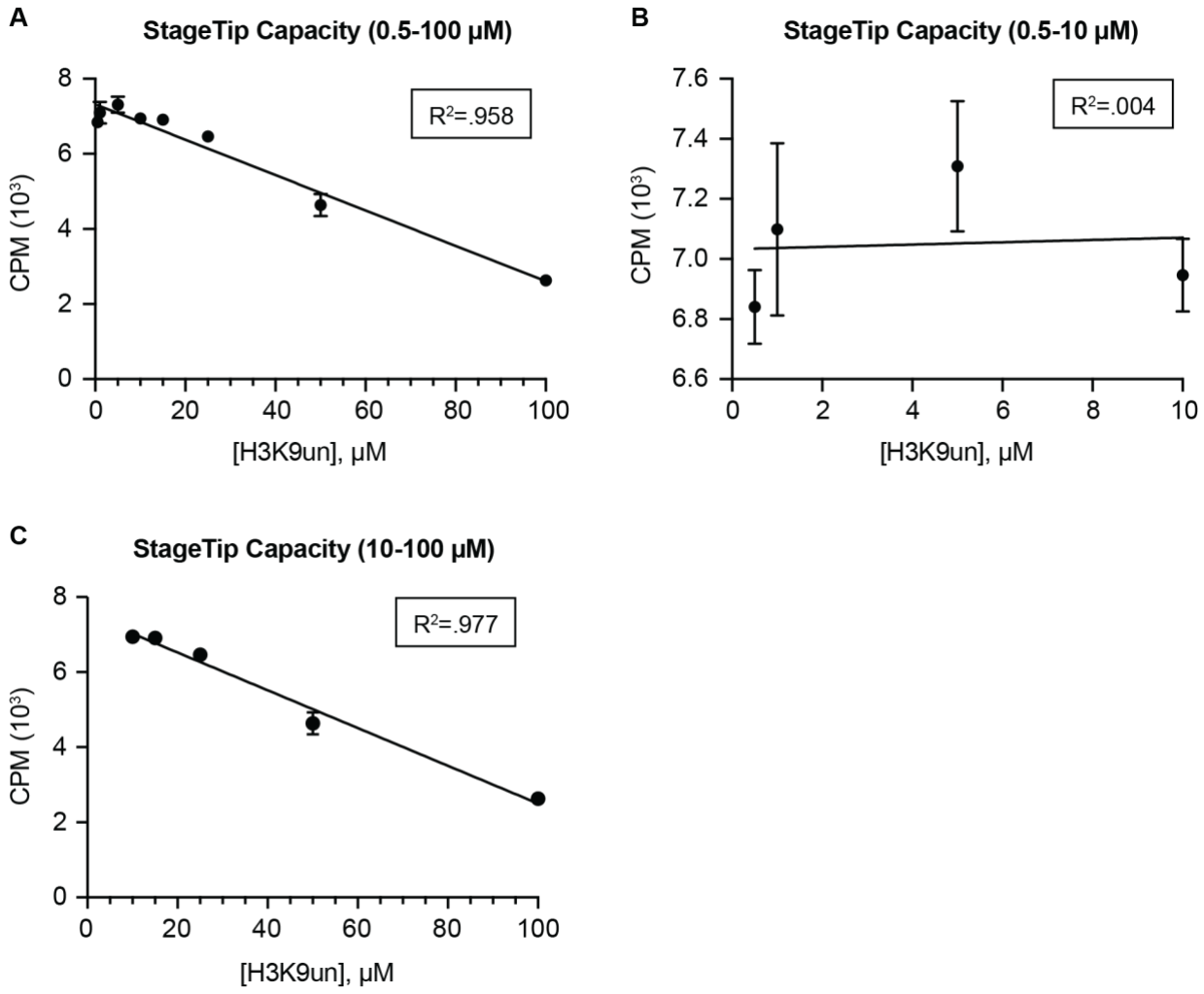

3.3.4 Sensitivity vs P81 Phosphocellulose

Results from wash volume, reaction buffer, and StageTip capacity optimization steps show EZ-Tip is a sensitive, reliable method for quantifying radiolabeled peptide product formation. However, as previously published radiometric methyltransferase data has largely been generated using P81 phosphocellulose, it is important that EZ-Tip is similarly efficacious. To directly compare EZ-Tip and P81-based methods, EHMT2 was incubated with H3K9un peptide over a 20 min time course after which aliquots from a common time point were assayed by both methods. Substrate turnover measurements generated from either EZ-Tip or P81 were very similar, with P81 averaging only 15% greater substrate turnover across all time points (i.e., 5 min, 10min, and 20 min) (Figure 3-4A). [methyl-^{3}H] SAM background signal was also similar for both EZ-Tip (0.2% of total reaction CPM units) and P81 methods (0.13% of total reaction CPM units) (Figure 3-4B). Therefore, these data show EZ-Tip is an effective replacement for P81-based radiometric methods.

Figure 3-4: EZ-Tip vs P81 Phosphocellulose Comparison. (*A*) Radiometric EHMT2 activity time course assayed using either EZ-Tip and P81 phosphocellulose membrane. Reaction details – Volume = 500 µl; EHMT2 [c] = 25 nM; H3K9un peptide = 50 µM; SAM [c] = 50 µM; [methyl-^{3}H] SAM = ~100,000 per 20 µl. n = 3; error bars represent SD. (*B*) Background measurement depicted as percent of total reaction CPM eluted from StageTips or P81 in no-peptide control assay. Volume = 150 µl; EHMT2 [c] = 25 nM; SAM [c] = 50 µM; [methyl-^{3}H] SAM CPM = ~100,000 per 20 µl. n = 3; error bars represent SD. For panels (*A*) and (*B*) 30 µl aliquots were taken for EZ-Tip or P81 cleanup following a TFA quench to directly compare methods.

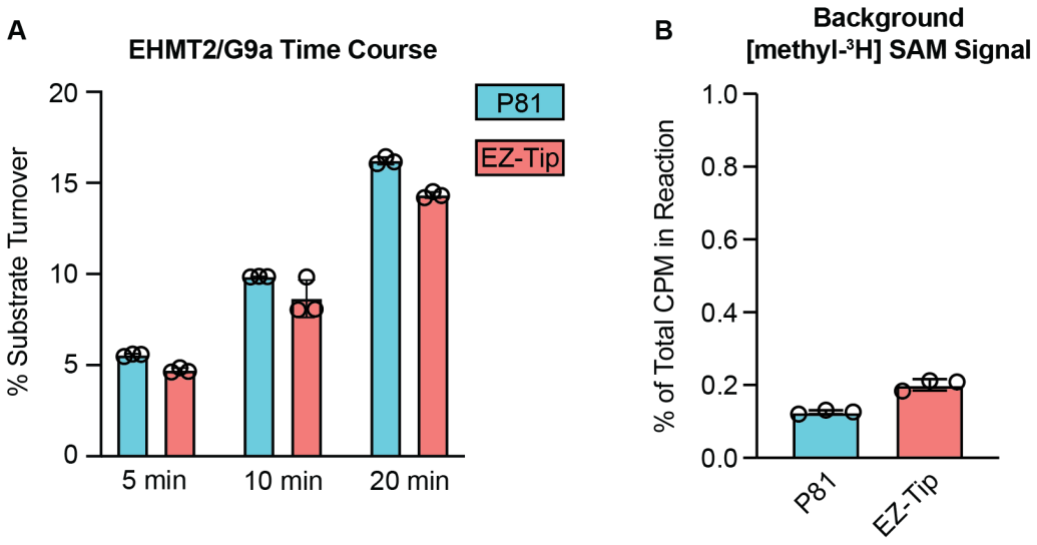

3.4 Final Protocol

3.4.1 Introduction to Final Protocol

Below, we describe how EZ-Tip can be used to determine Michaelis-Menten kinetic constants from a histone peptide saturation curve using [methyl-^{3}H] SAM and recombinantly purified HMT. However, the protocol can be easily adapted to determine kinetic constants from histone, nucleosome, or SAM saturation curves as well as to test the effects of small molecules on HMT activity. See Chapter 4 for more diverse EZ-Tip assay use.

3.4.2 Key Resources

REAGENT or RESOURCE	SOURCE	IDENTIFIER
Chemicals, Peptides, and Recombinant Proteins		
Ehmt2/G9a	This Chapter	N/A
H3K9 unmodified peptide	This Chapter	N/A
7 ml Pico Glass Vial	Perkin Elmer	Cat#6000167
Ultima Gold™ LSC Cocktail	Perkin Elmer	Cat#6013326
Adenosyl-L-methionine, S-[methyl-^{3}H] (SAM[^{3}H]), 250 µCi	Perkin Elmer	Cat#NET155V250 UC
S-adenosylmethionine, 32 mM, 0.5 ml	New England BioLabs	Cat#B9003S
Acetonitrile, 1L	Fischer Scientific	Cat#A998-1
Methanol, 1L	Fischer Scientific	Cat#A452-4
Formic Acid, 100ml	Millipore-Sigma	Cat#F0507-100ML
Trifluoroacetic Acid, 100ml	Millipore-Sigma	Cat#T6508-100ML
HEPES	Fischer Scientific	Cat#BP310-100
Triton™ X-100, 50ml	Millipore-Sigma	Cat#T8787-50ML
Dithiothreitol (DTT)	Gold Biotechnology	Cat#DTT10
AEBSF	Gold Biotechnology	Cat#A-540-500
$MgCl_2$ hexahydrate	Millipore-Sigma	Cat#M9272-100G
Software and Algorithms		
GraphPad Prism v9.0.0	GraphPad	N/A
Equipment		
BRAND® Dispensette® S Organic, Digital bottle-top dispenser	Millipore-Sigma	Cat# BR4630341-1EA
Affinisep AttractSPE™ Disks C18	Thomas Scientific	Cat#SPE-Disks-AN-47.T1.20
Centrifuge Adapter for 10µL, 200µL Tip	GL Sciences	Cat# 5010-21514
Tri-Carb 2190TR Liquid Scintillation Counter	Perkin Elmer	Discontinued – See Cat#A491000 as alternative
Sorvall™ Legend™ Micro 21 Centrifuge	Thermo Scientific	Cat#75002437
5L General Purpose Water Bath	Thermo Scientific	Cat#TSGP05

3.4.3 Assay Materials to Prepare in Advance

Buffers and Solutions

Time Required: 10-15 min

1. Notes specific to each individual buffer or solution are found below:
    a. HMT Activity Assay Buffer
        i. 50 mM HEPES (pH 7.9), 2 mM $MgCl_2$, 0.5 mM dithiothreitol, 0.1 mM AEBSF, and 0.01% Triton X-100
        ii. Store at 4°C to extend buffer longevity.
        iii. Buffer stored up to 2 months has no impact on reaction performance.
    b. Conditioning Solution
        i. 100% Methanol
        ii. Low-use reagent, will need 30 µl for each reaction.
    c. Quench Solution
        i. 6% Trifluoroacetic Acid in H_2O
        ii. Will be used as 3x stock.
    d. Wash Solution
        i. H_2O + 0.5% Formic Acid
        ii. High-use reagent, will need 230 µl for each reaction.
    e. Elution Solution
        i. 80% Acetonitrile +0.5% Formic Acid in H_2O
        ii. High-use reagent, will need 100 µl for each reaction.

Liquid Scintillation Counter Vials

Time Required: 5-10 min

1. Fill one, 7 ml Pico Glass Vial with 2 ml of Ultima Gold™ liquid scintillation counter (LSC) cocktail for each reaction, three vials for 10x [methyl-^{3}H] SAM stock standards, and three vials to assess LSC background
    a. Use a BRAND® Dispensette® S Organic, Digital bottle-top dispenser to efficiently aliquot Ultima Gold™ into vials.

b. Add 100 µl Elution Solution to each of the 3 prepared LSC background vials, mimicking the amount of Elution Solution that will be present in all [methyl-^{3}H] SAM reaction containing vials.

CRITICAL: Do not place any labels on vials or caps, this may impair light detection in the scintillation counter and/or result in vials jamming instrument. Label vials on cap using marker/pen.

C18 StageTip Preparation

Time Required: 5-10 min

1. Generate C18 membrane StageTips using 200 µl pipette tips as described in Rappsilber et al., 2007 [5].
    a. Each StageTip must contain two discs of AttractSPE™ C18 solid-phase extraction material.
        i. You will need to prepare one StageTip for each HMT reaction, including no peptide controls.
        ii. StageTips should be prepared fresh for each experiment.

CRITICAL: When preparing C18 StageTips, do not pack individual AttractSPE™ C18 discs too tightly. This will prevent your solutions from freely flowing through the material during downstream centrifugation steps.

NOTE: Empirically determine StagTip capacity prior to using EZ-Tip for HMT kinetics experiments. Optimization experiments suggest peptide StageTip retention decreases linearly from $1.0x10^{-4}$ to $1.0x10^{-3}$ micromoles peptide.

StageTip Collection Tube Preparation

Time Required: 5-10 min

1. Label two, 2 ml microcentrifuge tubes for each reaction including no peptide controls.
    a. The first tube will be used to collect StageTip flow-through and wash solution.
    b. The remaining tube will be used to collect StageTip eluent solution containing radiolabeled histone peptide.
2. Place centrifuge adapter in the first collection tube to accommodate 200 µl StageTip.

CRITICAL: Before beginning protocol determine whether benchtop microcentrifuge can accommodate 2 ml tubes with open caps. If not, cut off caps prior to fitting centrifuge adapters.

Dilute Methyltransferase and Histone Peptide to Final Working Concentrations in Individual 0.2 ml PCR Reaction Tubes

Time Required: 20-30 min

1. Using HMT Activity Assay Buffer, dilute HMT to 10x final desired assay concentration.
    a. Add 2 µl of 10x HMT stock to 12 individual 0.2 ml PCR tubes per replicate.
        i. Final HMT concentration chosen should keep SAM substrate turnover below 20% upon reaction quenching.
        ii. We recommend performing preliminary activity assays with varying concentrations of HMT (e.g. 1 nM to 500 nM) under saturating substrate conditions to empirically determine the optimal concentration for a fixed reaction time.
    b. If performing replicate reactions, HMT for each replicate should come from separate storage aliquots when possible.
2. Using HMT Activity Assay Buffer, initially dilute histone peptide to ~100x the estimated/previously determined $K_{m,\ PEPTIDE}$ corresponding to the HMT being used in your experiment.

   a. Using HMT Activity Assay Buffer, serial dilute peptide stock 2x, 10 times, resulting in 11 peptide stocks possessing unique concentrations. (e.x. 500 µM, 250 µM, 125 µM, 62.5 µM, etc.)
3. Treat each concentration of serially diluted peptide as a 10x stock and add 2 µl of each to separate 0.2 ml PCR tubes that already contain 2 µl of 10x HMT.
   a. To the remaining 1 tube that did not receive serially diluted peptide, add 2 µl of HMT Activity Assay Buffer as a no peptide control.
      i. The no-peptide control will be used to correct for both 1.) residual [methyl-^{3}H] SAM eluted from StageTip and 2.) HMT auto-methylation.
4. Bring volume of each 0.2 ml PCR tube up to 18 µl by adding 14 µl HMT Activity Assay Buffer

CRITICAL: Always determine concentration of individual enzyme aliquots immediately prior to use in order to correct for any precipitation that may have occurred during storage.

NOTE: All steps should be performed with reagents on ice.

Determine 10x Concentration of [methyl-3H] SAM Needed to Provide CPM Target

Time Required: 20 min initially but must only be done once for each original stock of [methyl-3H] SAM received from distributor.

1. Dilute [methyl-^{3}H] SAM 1:10 and 1:100 in Elution Buffer with a final volume of 50 µl and 200 µl, respectively
2. Add 10 µl of 1:10 and 1:100 [methyl-^{3}H] SAM dilutions to LSC vials containing 2 ml Ultima Gold™ LSC cocktail + 90 µl Elution Solution with 3 replicates of each dilution.
3. Analyze 6 LSC vials containing [methyl-^{3}H] SAM dilutions as well as three vials containing LSC cocktail + 100 µl Elution Solution as background controls in LSC.
4. Calculate specific activity and number of moles [methyl-^{3}H] SAM per CPM present in both 1:10 and 1:100 dilutions, averaging replicates to obtain final values.
   a. Note: Two dilutions are used to ensure a single dilution is not saturating the LSC.

5. Using the empirically derived moles per CPM value, calculate concentration of [methyl-^{3}H] SAM needed in 10x stock to provide 1x10^5 CPMs in a 20 µl reaction.
    a. With a final CPM count of 1x10^5 in a reaction, there is sufficient sensitivity to reliably quantify substrate turnover as low as ~0.1%.

NOTE: All steps should be performed with reagents on ice.

10x [methyl-^{3}H] SAM Stock Preparation

Time Required: 5 min

1. Calculate volumes needed to meet the 10x target concentrations of [methyl-^{3}H] and non-radiolabeled SAM, using HMT Activity Assay Buffer to bring your 10x [methyl-^{3}H] SAM stock up to its final volume.
    a. Final total SAM concentration in reaction should be at minimum 5x greater than the HMT's previously calculated or estimated $K_{M,\,SAM}$.
2. In three separate 0.2 ml PCR tubes, add 2 µl of 10x [methyl-^{3}H] SAM stock to 98 µl of Elution Solution.
    a. Transfer each mixture of 10x [methyl-^{3}H] SAM and Elution Solution into separate, previously prepared Pico Glass Vials containing 2 ml Ultima Gold™ LSC cocktail.
        i. These LSC vials will be used to empirically determine the total CPMs present in your reactions – which should average to roughly 1x10^5.

NOTE: All steps should be performed with reagents on ice.

3.4.4 Major Step Method Details

Incubate Individual 0.2 ml PCR Reaction Tubes and 10x [methyl-^{3}H] SAM Stock at 30^{o}C

Time Required: 10 min

1. Using a thermostat-controlled water bath, incubate prepared reaction tubes and 10x [methyl-^{3}H] SAM stock at 30^{o}C for 10 minutes.

NOTE: This major step ensures assay reactions maintain a constant temperature from initiation through quenching.

Initiate, Run, and Quench HMT Activity Assay

Time Required: 40 min

2. Initiate first reaction tube with 2 µl of 10x [methyl-^{3}H] SAM stock and return to 30^{o}C thermostat-controlled water bath.
    a. Upon initiating first reaction, start digital timer.
3. Every 30 seconds initiate a new reaction tube with 2 µl of 10x [methyl-^{3}H] SAM stock and return to 30^{o}C thermostat-controlled water bath.
    a. Remember to include no peptide controls.
    b. By initiating reactions in 30 second increments, it is possible to include three complete peptide dilutions and no peptide control replicates (i.e., 12 reactions per replicate) before the first reaction tube must be quenched.
4. 20 minutes following initiation of the first reaction tube, quench that reaction with 10 µl of Quench Solution and place tube on ice.
    a. Every 30 seconds quench the next reaction using 10 µl of Quench Solution in the same order they were initiated in, placing the tubes on ice following quenching.
        i. This ensures every reaction tube (including no peptide controls) runs for identical reaction times.

NOTE: This major step describes how to initiate and quench the HMT Activity Assay with a total reaction time of 20 minutes. Reaction time should be adjusted when needed to best fit the HMT of interest.

Bind, Wash, and Elute HMT Activity Assays from Prepared StageTips

Time Required: 25-35 min per 24 samples

5. Pre-wet StageTips fitted into 1st collection tube with 30 µl methanol. Spin at 2,000xg for 1 min at room temperature (RT).
6. Wash residual methanol from StageTips with 30 µl Wash Solution. Spin at 2,000xg for 1 min at RT.
7. Bind quenched reactions to StageTips fitted to correspondingly labeled collection tubes. Spin at 2,000xg for 1 min at RT.
8. Wash residual [methyl-^{3}H] SAM from StageTips with 200 µl Wash Solution. Spin at 2,000xg for 1 min at RT.
9. Transfer centrifuge adapters and StageTips from 1st set of collection tubes to correspondingly labeled 2nd set of collection tubes.
10. Elute HMT and histone peptide from StageTips with 100 µl Elution Solution. Spin at 2,000xg for 1 min at RT.

NOTE: This major step is critical for separating residual [methyl-^{3}H] SAM not consumed in the HMT activity assay from both the HMT and histone peptide of interest. Use StageTips as spin columns, pipetting solutions onto AttractSPE™ C18 discs from top of pipette tip.

Prepare and Count StageTip Eluent CPM Values from LSC Vials

Time Required: 10-15 min to transfer 24 samples to prepared LSC vials and 1 min counting duration in LSC per sample.

11. Transfer StageTip eluate from final collection tube into correspondingly labeled, previously prepared LSC vial.
    a. Flick tube to mix eluent with LSC cocktail.
12. Read CPM values in LSC.
    a. If performing HMT Activity Assay to generate a single replicate, you will have the following numbers of samples:
        i. Background blanks containing only LSC cocktail – 3
        ii. Replicate vials containing 2 µl 10x SAM stock – 3
        iii. Reactions covering serial peptide dilutions and no peptide control – 12
    b. If performing HMT Activity Assay in triplicate, you will have the following numbers of samples:
        i. Background blanks containing only LSC cocktail – 3
        ii. Replicate vials containing 2 µl 10x SAM stock – 3
        iii. Reactions covering serial peptide dilutions and no peptide controls – 36
    c. Protocol Settings:
        i. Energy window range: 1-18.6 keV
        ii. Count time per LSC vial: 1 minute

NOTE: This major step describes the final wet lab phase of the protocol where experimental data will be collected for downstream analyses.

<u>Determine Michaelis-Menten Constants</u>

Time Required: 10 min

13. Subtract average of background blank CPM values from reaction and standard CPM values.
    a. This step corrects for LSC instrument background.
14. For each replicate subtract no peptide control CPM value from all reaction CPM values
    a. This step corrects for both 1.) residual [methyl-^{3}H] SAM eluted from StageTip and 2.) HMT auto-methylation.

15. Divide corrected reaction CPM values by average CPM values of 10x [methyl-^{3}H] SAM stock standards
    a. This step will calculate the percentage of [methyl-^{3}H] SAM substrate turnover in decimal format.
16. Multiply values from Major Step 15 by micromolar concentration of total SAM present in reaction tubes to convert CPM values to µM.
17. Divide the µM values from Major Step 16 by the length in minutes HTM reactions ran.
    a. This step will calculate the rate of product formation.
    b. These values will be used to generate Michaelis-Menten constants.
18. Determine Michaelis-Menten constants
    a. Enter and plot the µM/min values from Major Step 17 into a new GraphPad Prism 9, "Enzyme Kinetics – Michaelis-Menten" table.
    b. Under "Analysis" select "Fit a curve with nonlinear regression."
    c. Under "Model" find the "Enzyme kinetics – Velocity as a function of substrate" header and select "kcat."
        i. The equation for the "Enzyme kinetics – Velocity as a function of substrate" model is as follows:
            1. Y = Et*kcat*X/(Km + X)
        ii. Variable Definitions:
            1. Y = rate of product formation/enzyme velocity
            2. X = substrate concentration
            3. Et = concentration of enzyme in reaction
    d. Under "Constrain" set Et equal to the µM concentration of enzyme present in your reactions and select "OK."
    e. Following these steps, you will have calculated the following values:
        i. $k_{cat,\ \mathrm{PEPTIDE}}$
        ii. $K_{m,\ \mathrm{PEPTIDE}}$
        iii. Vmax

3.5 Troubleshooting

3.5.1 Problem 1 – Low CPM Values

Low CPM values can result from numerous circumstances. One possibility is the HMT of interest has extremely low activity, which can be corrected by increasing the concentration of HMT in each reaction and/or by extending the reaction time. To avoid this possibility, we again recommend pre-determining the optimal concentration of HMT and reaction time prior to generating peptide saturation curves. Another possibility is the quality of [methyl-^{3}H] SAM stock from the manufacturer has degraded during long-term storage, resulting in untransferable [methyl-^{3}H] groups. As SAM is known to be highly unstable [11] we recommend aliquoting the original [methyl-^{3}H] SAM stock from the manufacturer into individual use aliquots, stored at -20^{o}C, to avoid freeze-thaw cycles. We also recommend empirically assessing the quality of [methyl-^{3}H] SAM aliquots by running HMT Activity Assays to completion in order to determine the percent of [methyl-^{3}H] SAM CPM values capable of being transferred to peptide substrate. Performing this type of assay regularly will allow you to track the quality of your [methyl-^{3}H] SAM over time. Similarly, HMT activity can be negatively affected by freeze-thaw cycles and/or long-term storage. Therefore, we also recommend storing the HMT in individual use aliquots and regularly assessing enzyme activity over time.

3.5.2 Problem 2 – Linear Saturation Curve

A linear saturation curve may suggest the peptide substrate concentrations used in the assay were not high enough to reach and surpass the HMT of interest's $K_{m,\ PEPTIDE}$. This issue can easily be addressed by increasing the greatest concentration of histone peptide prior to serial dilution. If increasing peptide concentrations does not solve this problem, it may be possible the HMT of interest is non-specifically methylating and/or interacting with the peptide substrate. The HMT Activity Assay Buffer contains 0.01% Trition X-100 to limit non-specific HMT-peptide interactions; however, if this issue persists, increasing the percent of Triton X-100 or adding other crowding such as bovine serum albumin may be beneficial.

3.5.3 Problem 3 – Dilute Stock Assay Components

The final reaction volume can easily be adjusted to accommodate low reaction component stock concentrations. However, if adjusting the reaction volume, continue to use the Quench Solution as a 3x reagent to obtain a final TFA concentration of 2% upon reaction quenching. Significantly increasing the reaction volume may also require the use of additional collection tubes to avoid flow-through in Major Steps 7 and 8 from coming in contact with the bottom of the StageTip.

3.6 Discussion

Here, we introduce EZ-Tip as a radiometric assay used for the removal of [methyl-^{3}H] SAM and detection of [methyl-^{3}H] histone peptide from *in vitro* methyltransferase reactions. EZ-Tip is a customizable, high throughput, cost effective alternative to current ZipTips® and P81 phosphocellulose-based assays. Furthermore, as EZ-Tip provides comparable results to P81 phosphocellulose, there are no compromises regarding assay sensitivity or reliability.

The direct detection of [methyl-^{3}H] peptide product is also an advantage for EZ-Tip compared to other fluorescence and luminescence-based methyltransferase assays that require coupled reactions to quantify S-adenosylhomocysteine (SAH) production, an indirect measurement of HMT activity [9,12,13]. The reliance of these assays on subsequent SAH processing introduces potential for downstream steps to become rate-limiting for signal production. In this scenario, the fluorescent/luminescent signal would not accurately reflect a methyltransferase's activity. For example, fluorescence-based assays first use SAH hydrolase (SAHH) to hydrolyze SAH at the sulfur atom, generating a free adenosine and homocysteine molecule. The now free SAH sulfur is then available to react with a fluorescent dye that can be excited to emit fluorescent signal. Therefore, both SAHH and fluorescent dye labeling steps must be more efficient than SAH production to accurately assess HMT activity. Fluorescence- and luminescence-based assays are valuable tools for high-throughput small molecule screening [13]; however, the ability of EZ-Tip to directly quantify [methyl-^{3}H] peptide product formation makes it a superior assay for more detailed, mechanistic enzymology studies.

EZ-Tip leverages the hydrophobic properties of C18 SPE discs to facilitate the separation of [methyl-^{3}H] peptide product, but not polar [methyl-^{3}H] SAM, from *in vitro* methyltransferase reactions. This general principle can be readily adapted to assay the activity of non-

methyltransferase enzymes that utilize polar cofactors such as protein kinases. Protein kinases utilize a polar ATP molecule as a cofactor for the transfer of a phosphate group to a protein substrate. Radiometric P81-based assays have also been the gold standard for quantifying *in vitro* protein kinase activity, creating the similar need for a P81 assay replacement due to ceased commercial P81 phosphocellulose production [14–16]. Therefore, with minimal optimization, EZ-Tip has potential to be a significant resource for diverse areas of study beyond chromatin biology and biochemistry.

3.7 Experimental Procedures

3.7.1 EZ-Tip Wash Optimization

For each replicate, 20 µl of 50µM of SAM containing ~$1x10^5$ CPM from [methyl-^{3}H] was acidified using 10 µl of 6% TFA and loaded onto a StageTip containing two C18 SPE disks. StageTips were centrifugated for at 2,000xg for 1 min at room temperature after which flow-through was collected and transferred to LSC vials containing 2 ml Ultima Gold LSC cocktail. Different volumes of wash buffer (H_2O + 0.5% TFA) were added to individual StageTips which were centrifugated as described earlier. 400 µl washes were split into 2 x 200 µl washes. Flowthrough from all washes were collected and transferred to LSC vials containing 2 ml Ultima Gold LSC cocktail. Following washes, residual SAM was eluted from StageTips using 100 µl elution buffer (80% ACN, 19.5% H_2O, 0.5% TFA) and previously described centrifugation conditions. Eluates were collected and transferred to LSC vials containing 2 ml Ultima Gold LSC cocktail. Wash and elution buffer was added to each vial when necessary bring final volumes wash and elution buffer volumes up to 400 µl and 100 µl, respectively. This ensures the solution composition of each vial is identical, eliminating potential variability in LSC signal quenching. CPM values were collected in Perkin Elmer TRI-CARB 2190TR liquid scintillation counter, converted to % of total CPM values present, and compared across conditions to assess wash volume efficiencies.

3.7.2 Reaction Buffer Optimization

Reaction buffers (50 mM HEPES pH 7.9, 2 mM $MgCl_2$, 0.5 mM DTT, and 0.1 mM AEBSF) ± 0.01% Triton X-100 were cross compared for their influence on Ehmt2 H3K9un^{PEPTIDE} saturation curves using the radiometric EZ-Tip methyltransferase assay. CPM

values generated from the saturation curves were converted to rates of product formation (µM/min) and used to generate Michaelis-Menten kinetic constants via GraphPad Prism v9.1.0 via the following equation: Y = Et*kcat*X/(Km + X). Variable definitions are as follows: Y = rate of product formation/enzyme velocity; X = substrate concentration; Et = concentration of enzyme in reaction.

3.7.3 Determination of StageTip Binding Capacity

H3K9un peptide was diluted into 20 µl using EZ-Tip methyltransferase activity buffer (50 mM HEPES pH 7.9, 2 mM $MgCl_2$, 0.5 mM DTT, 0.1 mM AEBSF, 0.1% Triton X-100) with final concentrations ranging from 100 µM to 0.5 µM. Each replicate contained a fixed concentration of 0.5 µM [methyl-^{3}H] H3K9me1 peptide. Peptide dilutions were acidified using 10 µl of 6% TFA after which they were loaded, washed, and eluted from StageTips containing two C18 SPE disks as described in Chapter 3.4. Eluates were transferred to LSC vials containing 2 ml Ultima Gold LSC cocktail and read using Perkin Elmer TRI-CARB 2190TR liquid scintillation counter. CPM values were plotted as a function of final peptide concentration. Simple linear regression analysis was performed on plot to derive equation that can be used to generate peptide binding efficiency correction factors when appropriate.

3.7.4 P81 Phosphocellulose Methyltransferase Assay Comparison

25nM Ehmt2 was incubated with 50 µM H3K9un^{PEPTIDE} and 50 µM total SAM with ~1x10^5 CPM from [methyl-^{3}H] SAM for 5 min, 10 min, or 15 min. At each time point an aliquot was removed from a master reaction and quenched with 3x 6% TFA. From the acidified reaction, 30 µl aliquots were prepared for LSC analysis using EZ-Tip or P81 phosphocellulose. No

peptide control reactions were also included. EZ-Tip samples were prepared as discussed in Chapter 3.4. For P81 phosphocellulose, 30 µl of acid quenched reaction was spotted onto P81 membrane and allowed to air dry for 10 min. Once dry, P81 membranes were washed 3 x 5 min in 300 ml 0.1 M $NaHCO^3$ with agitation. After final wash, P81 membranes were dipped in acetone and allowed to air dry for 10 min. Once dry, P81 membranes were added to LSC vials containing 3 ml Ultima Gold LSC cocktail. Parallel EZ-Tip reactions were also added to LSC vials containing 3 ml, as opposed to the normal 2 ml, of Ultima Gold LSC cocktail. LSC vials were read in Perkin Elmer TRI-CARB 2190TR liquid scintillation counter after which CPM values were converted to % of total CPM values present in pre-cleaned reaction for direct comparison of assay sensitivities.

3.8 Acknowledgements

This research was supported through grants from the NIH (S.A.H. – T32 DK007665 and J.M.D. – R37 GM059785). We also thank the Peter Lewis laboratory at the University of Wisconsin-Madison for providing us with the P81 phosphocellulose used in section 3.3.4.

3.9 References

1. Fingerman, I. M. et al. (2008) In Vitro Histone Methyltransferase Assay. *CSH. Protoc* pdb.prot4939.
2. Strahl, B. D. et al. (2001) Methylation of histone H4 at arginine 3 occurs in vivo and is mediated by the nuclear receptor coactivator PRMT1. *Current Biology.* 11, 996–1000.
3. Hevel, J. M. & Price, O. M. (2020) Rapid and direct measurement of methyltransferase activity in about 30 min. *Methods.* 175, 3–9.
4. Suh-Lailam, B. B. & Hevel, J. M. (2010) A fast and efficient method for quantitative measurement of S-adenosyl-l-methionine-dependent methyltransferase activity with protein substrates. *Analytical Biochemistry.* 398, 218–224.
5. Rappsilber, J. et al. (2007) Protocol for micro-purification, enrichment, pre-fractionation and storage of peptides for proteomics using StageTips. *Nature Protocols.* 2, 1896–1906.
6. Murn, J. & Shi, Y. (2017) The winding path of protein methylation research: milestones and new frontiers. *Nature Reviews Molecular Cell Biology.* 18, 517–527.
7. Manning, G. et al. (2002) Evolution of protein kinase signaling from yeast to man. *Trends in Biochemical Sciences.* 27, 514–520.
8. Ubersax, J. A. & Ferrell Jr, J. E. (2007) Mechanisms of specificity in protein phosphorylation. *Nature Reviews Molecular Cell Biology.* 8, 530–541.
9. Allali-Hassani, A. et al. (2011) Fluorescence-Based Methods for Screening Writers and Readers of Histone Methyl Marks: *Journal of Biomolecular Screening.* doi:10.1177/1087057111422256.

10. Jayaram, H. et al. (2016) S-adenosyl methionine is necessary for inhibition of the methyltransferase G9a by the lysine 9 to methionine mutation on histone H3. *PNAS.* 113, 6182–6187.
11. Wu, S. E. et al. (1983) Chiral instability at sulfur of S-adenosylmethionine. *Biochemistry.* 22, 2828–2832.
12. Hsiao, K. et al. (2016) Methyltransferase-Glo: a universal, bioluminescent and homogenous assay for monitoring all classes of methyltransferases. *Epigenomics.* 8, 321–339.
13. Dong, G. et al. (2020) Optimization of High-Throughput Methyltransferase Assays for the Discovery of Small Molecule Inhibitors. *ACS Comb. Sci.* 22, 422–432.
14. Davis, M. I. et al. (2011) Comprehensive analysis of kinase inhibitor selectivity. *Nature Biotechnology.* 29, 1046–1051.
15. Ma, H. et al. The challenge of selecting protein kinase assays for lead discovery optimization. *Expert Opin Drug Discov.* 3, 607–621.
16. Duong-Ly, K. C. & Peterson, J. R. (2016) A high-throughput radiometric kinase assay. *Methods Mol Biol.* 1360, 87–95.

Chapter 4: Comparative Enzymatic Analysis of H3 Lys9 Methyltransferases

Spencer A. Haws[1,2], Lillian J. Miller[1,2], Vyacheslav I. Kuznetsov[1,2], and John M. Denu[1,2]

[1]Wisconsin Institute for Discovery, University of Wisconsin-Madison
[2]Department of Biomolecular Chemistry, SMPH, University of Wisconsin-Madison

*Results presented here are unpublished at time of thesis deposition.

4.1 Abstract

Deprivation of the universal methyl-donor S-adenosylmethionine (SAM) significantly disrupts histone methylation patterns. Di-/tri-methylation levels are exceedingly sensitive to this metabolic perturbation while mono-methyl modifications are robust and can be actively maintained. This apparent discrepancy in enzyme activity could be driven by differences in the inherent catalytic properties of histone methyltransferases (HMTs), resulting in select enzymes being better equipped to function during decreased SAM availability. Here, we address this hypothesis by performing detailed biochemical analyses on three functionally distinct H3 Lys9 HMT pairs. Favorable k_{cat}, but not $K_{m,\ substrate}$, values were found to improve catalytic efficiency on $H3K9un^{PEPTIDE}$ relative to $H3K9me2^{peptide}$ substrate, regardless of HMT functional classifications. This observation was conserved across SAM and peptide Michaelis-Menten saturation curves, revealing a fundamental property of H3K9 HMTs and the mechanistic basis for epigenetic adaptation to methyl-metabolite depletion.

4.2 Introduction

Histone methylation (K_{me}) is an epigenetic post-translational modification (PTM) catalyzed by histone methyltransferases (HMTs) on the ε-amino group of lysine residues. Histone lysine residues can be utilized as platforms for three distinct methylation states (mono-, di-, and tri-methylation), that along with the residue's primary amino acid sequence location, confer K_{me} biological function [1]. For example, H3 Lys4 mono-methylation (H3K4me1) is known to mark active or primed enhancers while H3 Lys27 tri-methylation (H3K27me3) at gene promoters is associated with transcriptional repression [2–7]. The multiplicity and location of histone K_{me} deposition is dependent on HMTs which have specificities in both respects, enabling tight regulation over a cell's histone K_{me} profile [8].

Although lysine HMTs vary based on their catalytic domains, K_{me} multiplicity, and histone lysine targets, all enzymes require S-adenosylmethionine (SAM) as their methyl-donor cofactor. SAM is the metabolic product of methionine in the methionine cycle which is the only known mechanism supporting intracellular SAM availability in higher eukaryotes [9]. This reliance on intracellularly derived SAM to support HMT activity creates an interdependence between metabolism and the epigenome [10–12]. Various studies have highlighted this relationship, illustrating how impaired SAM metabolism negatively impacts histone K_{me} abundance. Published literature as well original data presented in Chapter 2 suggest all forms of histone K_{me} are not equally sensitive to decreased SAM availability, with di- and tri-methyl PTMs generally possessing greater sensitivity than mono-methyl PTMs. For example, in Chapter 2, we show H3 Lys9 mono-methylation (H3K9me1) is actively maintained during SAM depletion in cancerous cell lines from diverse lineages as well as in whole organisms [13]. This H3K9me1 maintenance occurs in the presence of lost di- and tri-methylation to preserve acute

heterochromatin stability and long-term epigenetic persistence upon metabolic recovery. Kera et al., 2013 have also shown in mouse embryonic fibroblasts (MEFs) that siRNA knockdown of the mammalian SAM synthetase MATIIα stimulates decreased H3K4me3 and H3K9me3 abundance although H3K4me1/2 and H3K9me1/2 are unaffected [14].

It is hypothesized the sensitivity or robustness of histone K_{me} to fluctuations in SAM availability may be explained by the inherent catalytic properties of HMTs [12,15]. Unfortunately, prior enzymatic analyses of HMTs are unable to address this question as 1.) only a small subset of HMTs have been characterized in a single study and 2.) multiple forms of substrate K_{me} multiplicity are not typically included making it difficult to assess substrate-specific effects on enzyme activity. Therefore, a detailed comparative analysis is needed to comprehensively determine how metabolic fluctuations in SAM availability could impact HMT catalysis on substrates with different degrees of K_{me} multiplicity.

In this study, the inherent catalytic properties of six H3K9 HMTs are compared by employing detailed biochemical analyses that include steady-state kinetics and quantitative binding assays with both $H3K9un^{PEPTIDE}$ and $H3K9me2^{PEPTIDE}$ substrates. The H3K9 HMTs assessed in this study represent three distinct groups of enzymes: PRDM3/PRDM16, EHMT1/EHMT2, and SUV39H1/SUV39H2. PRDM3 and PRDM16 catalyze H3K9 mono-methylation on cytoplasmic H3 proteins, which once translocated to the nucleus, facilitate heterochromatin anchoring to the nuclear lamina and major satellite repeat repression in MEFs [16]. EHMT1 and EHMT2 are the primary nuclear H3K9 mono-/di-methyltransferases, best known for regulating facultative heterochromatin and subsequent gene repression [17–20]. SUV39H1 and SUV39H2 catalyze nuclear H3K9 di-/tri-methylation from H3K9me1 substrate, regulating constitutive heterochromatin formation and maintenance [21–24]. These functions are

critical for the repression of repetitive and retrotransposable elements as well as 3-dimensional chromosome compartmentalization [25–28]. By assessing the biochemical characteristics of these enzymes in a single study, we generate a comprehensive view of the inherent catalytic properties that dictate HMT activity during SAM depletion.

4.3 Results

4.3.1 Differences in k_{cat} Broadly Differentiate Nuclear from Cytoplasmic HMTs

Due to a lack of detailed biochemical investigations, the intrinsic catalytic properties of cytoplasmic H3K9 mono-methyltransferases PRDM3 and PRDM16 are unknown. As a result, it is unclear whether these more recently identified HMTs possess relevant catalytic activity compared to better studied nuclear enzymes in the context of SAM depletion. To begin revealing how these HMTs may be enzymatically similar or distinct from nuclear H3K9 HMTs, Michaelis-Menten SAM saturations curves were generated for all enzymes using H3K9un^{PEPTIDE} substrate. When comparing kinetic constants calculated from SAM saturation curves, major differences in k_{cat} between nuclear and cytoplasmic enzymes were striking (Table 4-1). Both PRDM3 and PRDM16 possessed k_{cat} values a minimum of three orders of magnitude below those of all nuclear HMTs, including SUV39H1 and SUV39H2 for which H3K9un^{PEPTIDE} is not a physiologically relevant substrate. Differences in k_{cat} were the major discrepancy between cytoplasmic and nuclear enzymes as all HMTs possessed relatively similar $K_{m,\,SAM}$ values (Table 4-1). Therefore, these data suggest the drastically lower k_{cat} for PRDM3 and PRDM16 make it unlikely intrinsic catalytic properties alone account for their retained activity under SAM depleted conditions.

Interestingly, it has been proposed that PRDM3 and PRDM16 possess unique catalytic mechanisms compared to other SET domain-containing methyltransferases due to lack of key residue conservation in the catalytic and SAM binding domains [29]. In the catalytic domain, neither PRDM3 nor PRDM16 possess the final tyrosine residue of the consensus ELxF/YDY sequence. This residue has both structural and catalytic importance in canonical SET domain-containing HMTs [30–32]. In place of this critical tyrosine, PRDM3 and PRDM16 contain

methionine and valine residues, respectively, which lack the aromatic structure and functional hydroxyl group provided by the consensus tyrosine. Regarding the PRDM3 and PRDM16 SAM binding domains, neither enzyme possesses the asparagine residue which begins the NHS/CxxPN consensus sequence [33]. Instead, both enzymes contain an arginine residue that has been shown to prevent SAH binding in PRDM4 [29]. Together, these observations suggest PRDM3 and PRDM16 must rely on non-canonical SET domain mechanisms to support their catalytic activities.

Table 4-1: SAM^{H3K9UN} Saturation Curve Michaelis-Menten Constants. Table of Michaelis-Menten kinetic constants generated using EZ-Tip assay and $H3K9un^{PEPTIDE}$ substrate. Enzyme concentrations and reaction times were optimized to limit maximal substrate turnover to 20%. Saturating $H3K9un^{PEPTIDE}$ concentrations are a minimum 5x greater than the $K_{m,\ H3K9un}$ associated with/estimated for each enzyme.

	SAM^{H3K9un} Michaelis-Menten Constants		
	K_m (μM)	k_{cat} (min^{-1})	k_{cat}/K_m ($min^{-1}\ \mu M^{-1}$)
EHMT1	13.51 ± 4.95	12.69 ± 0.65	1.01 ± 0.27
EHMT2	19.21 ± 2.00	7.62 ± 0.11	0.40 ± 0.04
SUV39H1	4.52 ± 0.49	0.43 ± 0.04	0.10 ± 0.02
SUV39H2	12.58 ± 3.60	12.20 ± 3.90	0.97 ± 0.07
PRDM3	18.11 ± 0.51	$4.61E^{-3} \pm 1.7E^{-4}$	$2.55E^{-4} \pm 9.1E^{-6}$
PRDM16	20.77 ± 2.92	$6.23E^{-3} \pm 2.2E^{-4}$	$3.03E^{-4} \pm 3.5E^{-5}$

4.3.2 $K_{m,\ SAM}$ Does Not Dictate HMT Activity Under Decreased SAM Availability

Due to the relatively insignificant catalytic activity of PRDM3 and PRDM16, inherent catalytic properties of nuclear HMTs are more likely to drive H3K9 mono-methylation during SAM depletion. For example, a lower $K_{m,\ SAM}$ for nuclear mono-methyl HMTs (EHMT1/EHMT2) relative to tri-methyl HMTs (SUV39H1/SUV39H2) may help support preferential H3K9 mono-methylation during periods of decreased SAM availability.

To test this hypothesis, $K_{m,\ SAM}$ values generated from physiologically relevant substrates (i.e., H3K9un^{PEPTIDE} for EHMT1/EHMT2 and H3K9me2^{PEPTIDE} for SUV39H1/SUV39H2) were compared across all nuclear enzymes. On H3K9un^{PEPTIDE} substrate, EHMT1 and EHMT2 possess low micromolar $K_{m,\ SAM}$ values of 13.51 µM and 19.21 µM, respectively (Figure 4-1A, Table 4-1). These $K_{m,\ SAM}$ values were slightly higher than those of SUV39H1 (3.6 µM) and SUV39H2 (8.18 µM) on H3K9me2^{PEPTIDE} substrate, suggesting decreased SAM availability is more likely to have a negative impact on mono-methyl rather than tri-methyl HMT activity (Table 4-2). However, as the difference in EHMT1/EHMT2 and SUV39H1/SUV39H2 $K_{m,\ SAM}$ is slight, it is unlikely intracellular SAM levels would stabilize within this tight range (i.e., ~9 µM to ~13 µM) and allow $K_{m,\ SAM}$ to dictate HMT activity. Furthermore, as only mono-methylation has been shown to be significantly retained during intracellular SAM depletion, these data suggest $K_{m,\ SAM}$ values alone cannot account for preferential mono-methyl HMT activity under this condition.

Table 4-2: $SAM^{H3K9me2}$ Saturation Curve Michaelis-Menten Constants. Table of Michaelis-Menten kinetic constants generated using EZ-Tip assay and $H3K9me2^{PEPTIDE}$ substrate. Enzyme concentrations and reaction times were optimized to limit maximal substrate turnover to 20%. Saturating $H3K9un^{PEPTIDE}$ concentrations are a minimum 5x greater than the $K_{m,\ H3K9un}$ associated with each enzyme.

	$SAM^{H3K9me2}$ Michaelis-Menten Constants		
	K_m (μM)	k_{cat} (min^{-1})	k_{cat}/K_m ($min^{-1}\ \mu M^{-1}$)
EHMT1	2.21 ± 0.65	0.67 ± 0.02	0.32 ± 0.08
EHMT2	6.1 ± 1.03	1.05 ± 0.07	0.17 ± 0.03
SUV39H1	3.60 ± 1.72	0.03 ± 0.01	0.01 ± 0.003
SUV39H2	8.18 ± 3.14	4.22 ± 0.35	0.55 ± 0.15

Figure 4-1: Comparative View of SAM$^{H3K9un/me2}$ Saturation Curve Michaelis-Menten Constants. Plots of (*A*) $K_{m,\ SAM}$, (*B*) k_{cat}, and (*C*) $k_{cat}/K_{m,\ SAM}$ values generated for the nuclear H3K9 HMTs EHMT1, EHMT2, SUV39H1, and SUV39H2. Raw data values are present in Table 4-1 and Table 4-2.

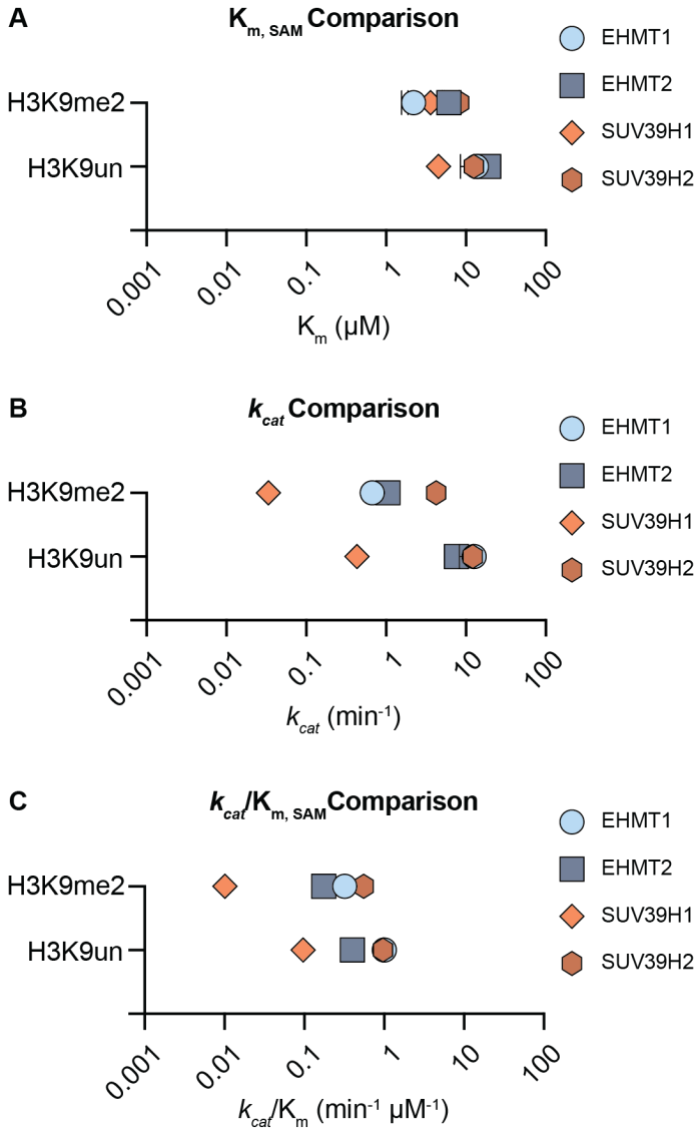

4.3.3 Substrate K_{me} Multiplicity Influences Inherent HMT Catalytic Properties

Higher $K_{m,\ SAM}$ values from H3K9un^{PEPTIDE} compared to H3K9me2^{PEPTIDE} saturation curves suggested substrate K_{me} multiplicity may significantly impact the inherent catalytic properties of H3K9 HMTs. To determine whether lower SUV39H1 and SUV39H2 $K_{m,\ SAM}$ values were influenced by substrate K_{me} multiplicity, $K_{m,\ SAM}$ values were compared across all nuclear enzymes using their non-physiologically relevant substrate (i.e., H3K9me2^{PEPTIDE} for EHMT1/EHMT2 and H3K9un^{PEPTIDE} for SUV39H1/SUV39H2). Interestingly, replacing H3K9un^{PEPTIDE} with H3K9me2^{PEPTIDE} decreased the EHMT1/EHMT2 $K_{m,\ SAM}$ to similar levels (2.21 µM and 6.1 µM, respectively) as SUV39H1 and SUV39H2 (Figure 4-1A, Table 4-2). The reverse was true when replacing H3K9me2^{PEPTIDE} with H3K9un^{PEPTIDE} for SUV39H1/SUV39H2, where $K_{m,\ SAM}$ increased for both enzymes with the later (12.58 µM) reaching similar levels as EHMT1/EHMT2 (Figure 4-1A, Table 4-1). These data reveal substrate K_{me} multiplicity has a significant impact on $K_{m,\ SAM}$ independent of HMT functional classification.

This phenomenon was similarly true when comparing k_{cat} and catalytic efficiency (i.e., $k_{cat}/K_{m,\ SAM}$) values generated from all Michaelis-Menten SAM saturation curves. The k_{cat} and $k_{cat}/K_{m,\ SAM}$ values generated with H3K9un^{PEPTIDE} substrate were consistently greater than those generated with H3K9me2^{PEPTIDE} from the same enzyme (Figure 4-1B, Table 4-1, Table 4-2). For EHMT1 and EHMT2, k_{cat} values were two orders of magnitude greater when H3K9un^{PEPTIDE} was utilized rather than H3K9me2^{PEPTIDE} (Figure 4-1B). SUV39H1 and SUV39H2 k_{cat} values were not influenced to the same extent as those for EHMT1 and EHMT2, although increased substrate K_{me} multiplicity still significantly decreased the k_{cat} for SUV39H1 and SUV39H2 (Figure 4-1B). Similarly trending differences were reflected in $k_{cat}/K_{m,\ SAM}$ values. However, changes in catalytic efficiency were slightly muted compared to those for k_{cat} as $K_{m,\ SAM}$ also decreases with

increased substrate K_{me} multiplicity (Figure 4-1C, Table 4-1, Table 4-2). Together, these data show substrate K_{me} multiplicity significantly impacts inherent HMT catalytic properties in a highly conserved manner.

4.3.4 Increased Mono-Methylation Catalytic Efficiency is Conserved Feature of H3K9 HMTs

Kinetic constants extracted from Michaelis-Menten SAM saturation curves revealed as substrate K_{me} multiplicity increases, catalytic efficiency of a given reaction decreases. This decrease in catalytic efficiency, which is driven by large decreases in k_{cat}, may be the mechanism supporting H3K9me1 abundance during SAM depletion. To determine whether mono-methyltransferase reactions also possessed greater catalytic efficiency under saturating SAM conditions, kinetic constants generated from Michaelis-Menten $H3K9un^{PEPTIDE}$ and $H3K9me2^{PEPTIDE}$ saturation curves were compared across nuclear enzymes.

Supporting the original observation made from SAM saturation curves, all Michaelis-Menten kinetic constants from peptide saturation curves were significantly impacted by substrate K_{me} multiplicity (Table 4-3, Table 4-4). $K_{m,\ PEPTIDE}$ values, although remaining within a low micromolar range, increased with K_{me} multiplicity for each enzyme (Figure 4-2A). These differences in $K_{m,\ PEPTIDE}$ were relatively minor in comparison to the large decreases observed in k_{cat} which reflected those obtained from SAM saturation curves as expected (Figure 4-2B, Table 4-3, Table 4-4).

Opposing responses of $K_{m,\ PEPTIDE}$ and k_{cat} values to increasing substrate K_{me} multiplicity resulted in significantly larger decreases in catalytic efficiency than those identified from SAM saturation curves (Table 4-3, Table 4-4). The $k_{cat}/K_{m,\ PEPTIDE}$ value ranges dropped from low micromolar (i.e., 1.03 min^{-1} μM^{-1} to 6.38 min^{-1} μM^{-1}) to nanomolar levels (i.e., 10 min^{-1} nM^{-1} to 430 min^{-1} nM^{-1}) for all enzymes (Figure 4-2C). Therefore, these results reveal increases in substrate K_{me} multiplicity negatively influence H3K9 HMT catalytic efficiency, primarily via large decreases in k_{cat}. Furthermore, as these conclusions support the original observations drawn

from SAM saturation curves, the negative influence of substrate K_{me} multiplicity on catalytic efficiency appears to be a fundamental characteristic of H3K9 HMTs.

Table 4-3: H3K9un^{PEPTIDE} Saturation Curve Michaelis-Menten Constants. Table of Michaelis-Menten kinetic constants generated using EZ-Tip assay and H3K9un^{PEPTIDE} substrate. Enzyme concentrations and reaction times were optimized to limit maximal substrate turnover to 20%. Saturating SAM concentrations are a minimum 5x greater than the $K_{m,\ H3K9un}$ associated with/estimated for each enzyme.

	H3K9un^{PEPTIDE} Michaelis-Menten Constants		
	K_m (μM)	k_{cat} (min^{-1})	k_{cat}/K_m (min^{-1} $μM^{-1}$)
EHMT1	2.18 ± 0.32	13.79 ± 0.70	6.38 ± 0.67
EHMT2	3.62 ± 0.87	9.36 ± 0.59	2.66 ± 0.46
SUV39H1	0.60 ± 0.08	0.61 ± 0.05	1.03 ± 0.18
SUV39H2	5.26 ± 1.44	6.06 ± 0.56	1.19 ± 0.22

Table 4-4: H3K9me2^{PEPTIDE} Saturation Curve Michaelis-Menten Constants. Table of Michaelis-Menten kinetic constants generated using EZ-Tip assay and H3K9me2^{PEPTIDE} substrate. Enzyme concentrations and reaction times were optimized to limit maximal substrate turnover to 20%. Saturating SAM concentrations are a minimum 5x greater than the $K_{m, H3K9un}$ associated with/estimated for each enzyme.

	H3K9me2^{PEPTIDE} Michaelis-Menten Constants		
	K_m (μM)	k_{cat} (min^{-1})	k_{cat}/K_m (min^{-1} $μM^{-1}$)
EHMT1	15.74 ± 6.77	0.47 ± 0.04	0.033 ± 0.01
EHMT2	6.51 ± 1.60	0.48 ± 0.07	0.08 ± 0.01
SUV39H1	10.37 ± 2.78	0.09 ± 0.01	0.01 ± 0.003
SUV39H2	8.01 ± 2.95	3.38 ± 1.12	0.43 ± 0.11

Figure 4-2: Comparative View of H3K9un/me2^{PEPTIDE} Saturation Curve Michaelis-Menten Constants. Plots of (*A*) $K_{m,\ PEPTIDE}$, (*B*) k_{cat}, and (*C*) $k_{cat}/K_{m,\ PEPTIDE}$ values generated for the nuclear H3K9 HMTs EHMT1, EHMT2, SUV39H1, and SUV39H2. Raw data values are present in Table 4-3 and Table 4-4.

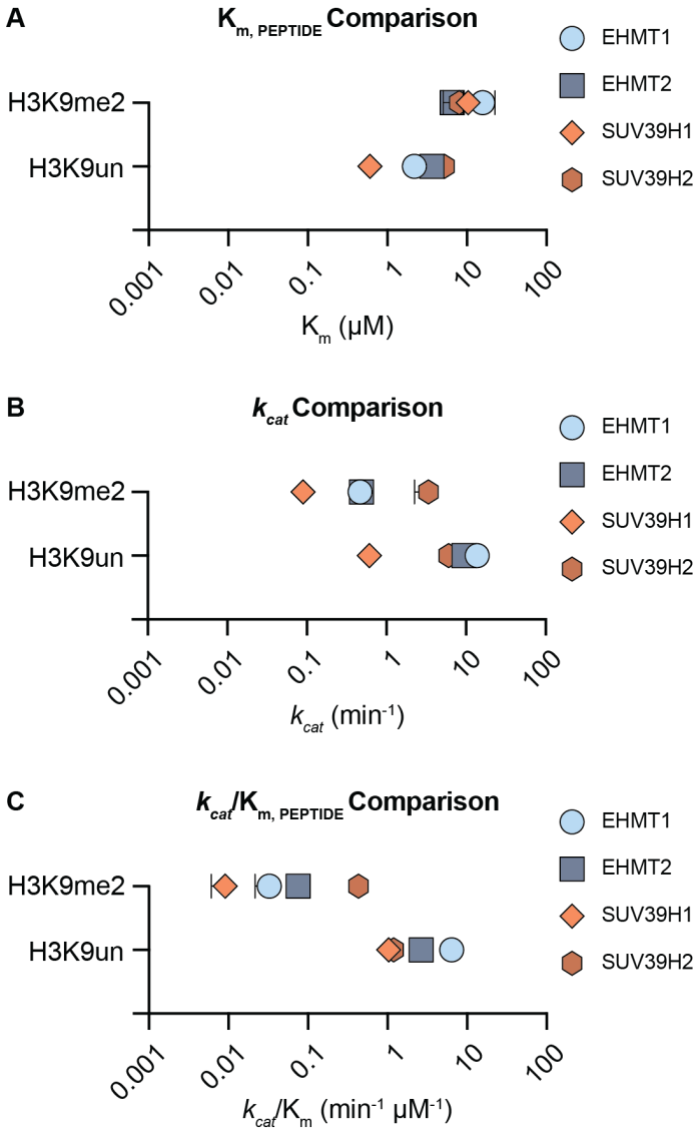

4.3.5 Peptide Binding Affinity has Negligible Influence on HMT Catalysis

Disruption of enzyme-substrate interactions due to methylation of the H3K9 ε-amino group could explain the conserved negative effects of K_{me} multiplicity on HMT catalytic efficiency. To determine how K_{me} multiplicity impacts HMT peptide binding affinities, fluorescence polarization (FP) assays were used to generate $H3K9un^{PEPTIDE}$ and $H3K9me2^{PEPTIDE}$ dissociation constants (K_d) for nuclear enzymes. Interestingly, unlike the previously discussed Michaelis-Menten kinetic constants, $K_{d,\ PEPTIDE}$ values were more greatly influenced by HMT functional classification than substrate K_{me} multiplicity (Table 4-5). EHMT1 and EHMT2 possessed low-nanomolar $K_{d,\ PEPTIDE}$ values for both $H3K9un^{PEPTIDE}$ and $H3K9me2^{PEPTIDE}$ substrates, with $K_{d,\ H3K9un}$ being slightly lower than $K_{d,\ H3K9me2}$ (Figure 4-3A). Minimal decreases in peptide affinity as a function of increased substrate K_{me} multiplicity were also observed for both SUV39H1 and SUV39H2. However, $K_{d,\ PEPTIDE}$ values were significantly greater for these enzymes relative to EHMT1 and EHMT2, reaching mid-nanomolar to low-micromolar levels (Figure 4-3A). When compared to the substrate K_{me} effects on $k_{cat}/K_{m,\ PEPTIDE}$, these data show $K_{d,\ PEPTIDE}$ is effected by substrate K_{me} appreciably less three of the four nuclear H3K9 HMTs (i.e., EHMT1, EHMT2, and SUV39H1) (Figure 4-3B). This suggests decreased peptide binding affinity cannot explain K_{me} multiplicity dependent changes in catalytic efficiency. Instead, substrate K_{me} multiplicity must dictate catalytic efficiency by directly influencing H3K9 HMT catalysis.

Table 4-5: H3K9un^{PEPTIDE} and H3K9me2^{PEPTIDE} Dissociation Constants. Table of enzyme $K_{d,\ PEPTIDE}$ values generated from fluorescence polarization binding assays using N-terminal 5-Carboxyfluorecin labeled H3K9un^{PEPTIDE} or H3K9me2^{PEPTIDE}.

	H3K9X Peptide K_d (μM)	
	H3K9un	H3K9me2
EHMT1	0.029 ± .001	0.124 ± 0.024
EHMT2	0.016 ± 0.0004	0.04 ± 0.003
SUV39H1	0.499 ± 0.045	0.629 ± 0.263
SUV39H2	1.075 ± 0.226	4.111 ± 2.426

Figure 4-3: Comparative View of $K_{d,\,PEPTIDE}$ and $k_{cat}/K_{m,PEPTIDE}$ Values. (*A*) Plot of $K_{d,\,PEPTIDE}$ values generated from both FAM-H3K9un^{PEPTIDE} and FAM-H3K9me2^{PEPTIDE} substrates using the nuclear H3K9 HMTs EHMT1, EHMT2, SUV39H1, and SUV39H2. (*B*) Log_2 H3K9me2^{PEPTIDE}/H3K9un^{PEPTIDE} fold-change $K_{d,\,PEPTIDE}$ and $k_{cat}/K_{m,PEPTIDE}$ values. Raw data values used to generate Figure 4-3A and 4-3B are present in Table 4-3, Table 4-4, and Table 4-5.

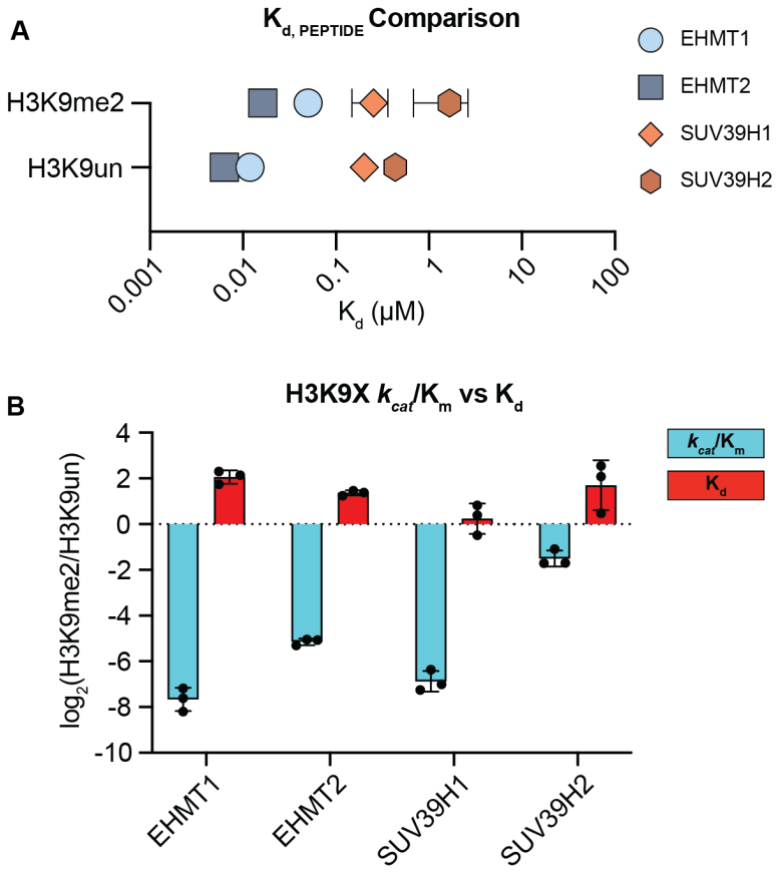

4.4 Discussion

Here, the biochemical properties of three functionally distinct pairs of H3K9 HMTs were assessed using *in vitro* steady-state kinetics and quantitative substrate binding assays. Results from these assays revealed $K_{m,\,SAM}$ values generated from physiologically relevant substrates are alone unable to drive mono-methyl HMT activity under SAM depleted conditions. Instead, greater HMT catalytic efficiency for mono-methylation relative to tri-methylation reactions is dictated by substrate K_{me} multiplicity, largely due to its negative influence on enzyme k_{cat}. This opposing effect of substrate K_{me} multiplicity on catalytic efficiency was identified from both SAM and peptide saturation curves for all six enzymes, revealing a fundamental inherent property of H3K9 HMTs.

While H3K9me1^{PEPTIDE} substrate has yet to have been included in this study, a structural study of the mutated SET domain lysine methyltransferase SET7/9 Y305F suggests H3K9 di-methylation is also less catalytically efficient than mono-methylation [34]. SET7/9 is considered the representative model for studying SET domain catalysis while the Y305F construct mimics the presence of a critical active site phenylalanine residue in the nuclear HMTs studied here [33,35,36]. Specifically, Rizzo et al., 2010 determined an active site water molecule positions the unmodified lysine substrate ε-amino group for nucleophilic attack of the SAM sulfur atom. The water molecule positions the lysine ε-amino group by facilitating a network of four hydrogen bonds between active site residues and the peptide substrate. However, the active site water molecule is lost when SET7/9 Y305F is provided with a mono-methyl lysine due to steric limitations. Loss of the active site water molecule frees a solvent pocket for the mono-methyl lysine to reside in, ultimately positioning the ε-amino group for nucleophilic attack of the SAM molecule. This loss of water molecule-substrate coordination for mono-methyl lysine residues is

the proposed mechanism driving significant decreases in catalytic efficiency for SET7/9 Y305F on TAF10^{PEPTIDE} K189me1 compared to K189un substrate [34]. Addition of H3K9me1^{PEPTIDE} substrate to the biochemical analyses of nuclear H3K9 HMTs will be critical for determining whether their catalytic efficiencies respond similarly to mono-methyl substrate as SET7/9 Y305F.

Irrespective of H3K9me1^{PEPTIDE} substrate exclusion, comparison of fundamental HMT properties across H3K9un^{PEPTIDE} and H3K9^{PEPTIDE} substrates provided invaluable insight into mechanistic foundation supporting epigenetic adaptation to methyl-metabolite depletion. Specifically, *in vivo* methyl-metabolite depletion stimulates significant changes in H3K9 substrate availability, with global decreases in di-/tri-methylation being accompanied by increases in unmodified lysine abundance. This shift towards lower global K_{me} multiplicity complements the greater catalytic efficiency of H3K9me1 HMTs as the relative concentration of their preferred substrate is increasing. Opposingly, this shift in K_{me} multiplicity negatively impacts H3K9me3 HMT activity as these enzymes, which are already limited by their poor catalytic efficiency, face significant loses in their relative substrate availability. Therefore, the synergism between greater catalytic efficiency for H3K9 mono-methylation and decreased global K_{me} multiplicity creates a biochemically favorable environment to support active regulation of H3K9me1 during methyl-metabolite depletion.

4.5 Experimental Procedures

4.5.1 Recombinant Protein Purification

The *H. sapiens* EHMT1 catalytic subunit (Addgene plasmid # 51314) and *H. sapiens* SUV39H2 catalytic subunit (Addgene plasmid # 25115) *E. coli* expression plasmids used in this study were acquired from addgene, made possible through a gift by Cheryl Arrowsmith. The *H. sapiens* EHMT2 catalytic subunit *E. coli* expression plasmid used in this study was provided by the laboratory of Peter W. Lewis at the University of Wisconsin-Madison. All remaining histone methyltransferase expression plasmids were generated for this study and will be made freely available from addgene. HMT amino acids included in expression plasmids are as follows: PRDM3 = 2-221; PRDM16 = 2-226; EHMT1 = 982-1266; EHMT2 = 913-1193; SUV39H1 = full length with N-terminal maltose binding protein; SUV39H2 = 162-410.

Transformed Rosetta™ *E. coli* competent cells were cultured in 1L of 2XYT media at 37^{o}C to an O.D. 600 of 0.8. IPTG was then added to each culture at a final concentration of 1mM. Cultures were allowed to grow for 16 hours at 18^{o}C before being harvested and stored at -80^{o}C. Pellets were resuspended in 30ml Buffer A (50 mM NaPi, 250 mM NaCl, 10mM imidazole, pH 7.8) and sonicated on ice in the presence of lysozyme. Lysate was centrifugated at 45,000xg for 45 min and the supernatant was collected. The supernatant was then loaded onto a HisTrap FF nickel column in line with a GE AKTA FPLC. Protein was eluted off the column using a linear gradient ending in 100% Buffer B (50 mM NaPi, 250 mM NaCl, 250 mM imidazole, pH 7.8) and collected into time-dependent fractions. Fractions were analyzed by coomassie staining of SDS-PAGE gels to assess purity.

Fractions determined to contain the protein of interest were pooled and dialyzed overnight at 4^{o}C in 4 L of HMT dialysis buffer (20 mM HEPES pH 7.5, 300 mM NaCl, 1 mM

TCEP, 10% Glycerol). Following dialysis, precipitated protein was pelleted via centrifugation at 4^{o}C for 10 min at 18,000xg and the supernatant was collected. Protein concentration determined via A280 absorbance values and extinction coefficient correction. Final protein samples were aliquoted into single-use 0.2 ml PCR tubes and flash frozen in liquid nitrogen prior to long-term storage at -80^{o}C.

4.5.2 Radiometric EZ-Tip Methyltransferase Assay

Michaelis-Menten saturation curves were generated under steady state-state conditions with the non-titrated component concentration being present at ≥ 5x K_m specific to each enzyme. Roughly 1x10^5 CPM values were provided by [methyl-^{3}H] SAM in each reaction. Reaction times and enzyme concentrations were optimized for each HMT to ensure substrate turnover remained below 20%. All CPM values were corrected for decreased StageTip capacity when peptide concentrations rose above 10 µM.

For specific details on EZ-Tip assay steps and components see Chapter 3.4.

4.5.3 Michaelis-Menten Constant Calculations

CPM values were converted to rates of product formation (µM/min) and used to generate Michaelis-Menten kinetic constants via GraphPad Prism v9.1.0 via the following equation: Y = Et*kcat*X/(Km + X). Variable definitions are as follows: Y = rate of product formation/enzyme velocity; X = substrate concentration; Et = concentration of enzyme in reaction.

4.5.4 Fluorescence Polarization Peptide Binding Assay

HMT, N-terminus 5-Carboxyfluorescein (5-FAM) labeled peptide, and SAH assay components were diluted in fluorescence polarization binding buffer (50mM HEPES pH7.9, 2 mM $MgCl_2$, 0.5 mM DTT, 0.1 mM AEBSF, 0.01% Triton X-100, 10% glycerol). SAH was present at a final concentration of 100 µM while 5-FAM labeled peptides were present at a final concentration of 20 nM. Protein concentrations ranged from low micromolar to nanomolar concentrations. Reactions were assembled in a black low-flange 384-welll plate with a final volume of 20 µl final volume. Upon addition of diluted enzyme as final reaction component, 384-well plates were sealed and centrifugated at 1,000xg for 30 sec at room temperature. Prepared 384-well plates were loaded into the BioTek Synergy H4 plate reader after which plates were shook for 10 sec followed by a 10 min incubation at 25^{o}C. Once the incubation was complete, polarization values were calculated using the BioTek Instruments Gen5 v1.11.5 software package.

4.5.5 Peptide Dissociation Constant (K_d) Calculations

Polarization values were exported from BioTek Instruments Gen5 v1.11.5 software and imported into GraphPad Prism v9.1.0 to calculate dissociation constants using the following one site- specific binding equation: Y = Bmax*X/(Kd + X). Variable definitions are as follows: Y = fluorescence polarization; X = enzyme concentration; Bmax = maximum specific binding; Kd = equilibrium dissociation constant.

4.5.6 Key Resources

REAGENT or RESOURCE	SOURCE	IDENTIFIER
Chemicals, Peptides, and Recombinant Proteins		
HEPES	Gold Biotechnology	Cat#H-400-100
Magnesium Chloride Hexahydrate	Millipore Sigma	Cat#M9272-100G
Sodium Chloride	Millipore Sigma	Cat#S9888-1KG
Glycerol	Thermo Fisher	Cat# G33-4
Acetonitrile	Thermo Fisher	Cat#A996-4
Formic Acid	Millipore Sigma	Cat#F0507-100ML
Trifluoroacetic Acid	Millipore Sigma	Cat#302031-100ML
Aprotinin	Gold Biotechnology	Cat#A-655-100
Leupeptin Hemisulfate	Gold Biotechnology	Cat#L-010-25
4-(2-Aminoethyl)-benzenesulfonylfluoride (AEBSF)	Gold Biotechnology	Cat# A-540-500

Dithiothreitol (DTT)	Gold Biotechnology	Cat#DTT100
Attract SPE Disks C18 47mm	Affinisep	Cat# SPE-Disks-C18-47.T1.20
H3K9 unmodified peptide (5'-ARTKQTARK$_{un}$STGGKAPRW-3')	This paper	N/A
H3K9 di-methylated peptide (5'-ARTKQTARK$_{me2}$STGGKAPRW-3')	This paper	N/A
pET28a-LIC-hEHMT1_982-1266	Addgene	N/A
pET28a-LIC-hEHMT2_913-1193	Peter W. Lewis Laboratory	N/A
pET45b-MBP-TEV-hSUV39h1_FL	This paper	N/A
pET28a-LIC-hSUV39H2_162-410	Addgene	Cat#25115
pET45b-hPRDM3_2-221	This paper	N/A
pET45b-hPRDM16_2-226	This paper	N/A
Software and Algorithms		
GraphPad Prism v9.1.0	N/A	https://www.graphpad.com/scientific-software/prism/

4.6 Acknowledgements

This research was supported through grants from the NIH (S.A.H. – T32 DK007665 and J.M.D. – R37 GM059785).

4.7 References

1. Greer, E. L. & Shi, Y. (2012) Histone methylation: a dynamic mark in health, disease and inheritance. *Nat. Rev. Genet.* 13, 343–357.
2. Heintzman, N. D. et al. (2009) Histone modifications at human enhancers reflect global cell-type-specific gene expression. *Nature.* 459, 108–112.
3. Heintzman, N. D. et al. (2007) Distinct and predictive chromatin signatures of transcriptional promoters and enhancers in the human genome. *Nat. Genet.* 39, 311–318.
4. Rada-Iglesias, A. et al. (2011) A unique chromatin signature uncovers early developmental enhancers in humans. *Nature.* 470, 279–283.
5. Local, A. et al. (2018) Identification of H3K4me1-associated proteins at mammalian enhancers. *Nature Genetics.* 50, 73–82.
6. Barski, A. et al. (2007) High-resolution profiling of histone methylations in the human genome. *Cell.* 129, 823–837.
7. Margueron, R. & Reinberg, D. (2011) The Polycomb complex PRC2 and its mark in life. *Nature.* 469, 343–349.
8. Hyun, K. et al. (2017) Writing, erasing and reading histone lysine methylations. *Experimental & Molecular Medicine.* 49, e324–e324.
9. Ducker, G. S. & Rabinowitz, J. D. (2017) One-Carbon Metabolism in Health and Disease. *Cell Metab.* 25, 27–42.
10. Haws, S. A. et al. (2020) Metabolism and the Epigenome: A Dynamic Relationship. *Trends Biochem. Sci.* 45, 731–747.
11. Boon, R. et al. (2020) Nuclear metabolism and the regulation of the epigenome. *Nature Metabolism.* 2, 1190–1203.

12. Dai, Z. et al. (2020) The evolving metabolic landscape of chromatin biology and epigenetics. *Nature Reviews Genetics.* 21, 737–753.
13. Haws, S. A. et al. (2020) Methyl-Metabolite Depletion Elicits Adaptive Responses to Support Heterochromatin Stability and Epigenetic Persistence. *Mol. Cell.* 78, 210-223.
14. Kera, Y. et al. (2013) Methionine Adenosyltransferase II-dependent Histone H3K9 Methylation at the COX-2 Gene Locus. *J. Biol. Chem.* 288, 13592–13601.
15. Mentch, S. J. & Locasale, J. W. (2016) One-carbon metabolism and epigenetics: understanding the specificity. *Ann. N. Y. Acad. Sci*.1363, 91–98.
16. Pinheiro, I. et al. (2012) Prdm3 and Prdm16 are H3K9me1 Methyltransferases Required for Mammalian Heterochromatin Integrity. *Cell.* 150, 948–960.
17. Tachibana, M. et al. (2002) G9a histone methyltransferase plays a dominant role in euchromatic histone H3 lysine 9 methylation and is essential for early embryogenesis. *Genes Dev.* 16, 1779–1791.
18. Ueda, J. et al. (2006) Zinc finger protein Wiz links G9a/GLP histone methyltransferases to the co-repressor molecule CtBP. *J. Biol. Chem.* 281, 20120–20128.
19. Zylicz, J. J. et al. (2015) Chromatin dynamics and the role of G9a in gene regulation and enhancer silencing during early mouse development. *eLife.* 4:e09571.
20. Jiang, Q. et al. (2020) G9a Plays Distinct Roles in Maintaining DNA Methylation, Retrotransposon Silencing, and Chromatin Looping. *Cell Rep.* 33, 108315.
21. Lachner, M. et al. (2001) Methylation of histone H3 lysine 9 creates a binding site for HP1 proteins. *Nature.* 410, 116–120.
22. Peters, A. H. et al. (2001) Loss of the Suv39h histone methyltransferases impairs mammalian heterochromatin and genome stability. *Cell.* 107, 323–337.

23. Rice, J. C. et al. (2003) Histone Methyltransferases Direct Different Degrees of Methylation to Define Distinct Chromatin Domains. *Mol. Cell.* 12, 1591–1598.
24. Loyola, A. et al. (2009) The HP1alpha-CAF1-SetDB1-containing complex provides H3K9me1 for Suv39-mediated K9me3 in pericentric heterochromatin. *EMBO Rep.* 10, 769–775.
25. Harr, J. C. et al. (2015) Directed targeting of chromatin to the nuclear lamina is mediated by chromatin state and A-type lamins. *J. Cell. Biol.* 208, 33–52.
26. Falk, M. et al. (2019) Heterochromatin drives compartmentalization of inverted and conventional nuclei. *Nature.* 570, 395–399.
27. Towbin, B. D. et al. (2012) Step-Wise Methylation of Histone H3K9 Positions Heterochromatin at the Nuclear Periphery. *Cell.* 150, 934–947.
28. Saksouk, N. et al. (2015) Constitutive heterochromatin formation and transcription in mammals. *Epigenetics & Chromatin.* 8, 3.
29. Wu, H. et al. (2013) Molecular Basis for the Regulation of the H3K4 Methyltransferase Activity of PRDM9. *Cell Reports.* 5, 13–20.
30. Wu, H. et al. (2010) Structural Biology of Human H3K9 Methyltransferases. *PLOS ONE.* 5, e8570.
31. Qian, C. & Zhou, M.-M. (2006) SET domain protein lysine methyltransferases: Structure, specificity and catalysis. *Cell. Mol. Life Sci.* 63, 2755–2763.
32. Smith, B. C. & Denu, J. M. (2009) Chemical mechanisms of histone lysine and arginine modifications. *Biochim. Biophys. Acta.* 1789, 45–57.
33. Dillon, S. C. et al. (2005) The SET-domain protein superfamily: protein lysine methyltransferases. *Genome Biol.* 6, 227.

34. Rizzo, P. A. D. et al. (2010) SET7/9 Catalytic Mutants Reveal the Role of Active Site Water Molecules in Lysine Multiple Methylation. *Journal of Biological Chemistry.* 285, 31849–31858.

35. Collins, R. E. et al. (2005) In Vitro and in Vivo Analyses of a Phe/Tyr Switch Controlling Product Specificity of Histone Lysine Methyltransferases. *Journal of Biological Chemistry.* 280, 5563–5570.

36. Couture, J.-F. et al. (2008) Structural origins for the product specificity of SET domain protein methyltransferases. *PNAS.* 105, 20659–20664.

Chapter 5: Conclusions and Future Directions

Spencer A. Haws[1,2] and John M. Denu[1,2]

[1]Wisconsin Institute for Discovery, University of Wisconsin-Madison
[2]Department of Biomolecular Chemistry, SMPH, University of Wisconsin-Madison

*Results presented here are unpublished at time of thesis deposition.

5.1 Conclusions

Many chromatin modifying enzymes rely on central metabolic cofactors to support their catalytic activities [1–3]. As a result, fluctuations in the availability of these cofactors directly influences a cell's ability to both "write" and "erase" chromatin post-translational modifications. This dynamic has been investigated in particular detail regarding histone methylation, which requires adequately available S-adenosylmethionine (SAM) to be used as a methyl-donor cofactor by histone methyltransferases (HMTs). Studies published prior to this work have largely focused on the susceptibility of histone methylation to altered SAM abundance [4]. For example, Mentch et al., 2015 have shown SAM deprivation stimulates global losses in *M. musculus* H3K4me3 abundance [5]. Opposingly, Ye et al., 2017 have shown SAM accumulation in *S. cerevisiae* stimulates accumulation of higher-order (i.e., di-/tri-) methylation at H3K4, H3K36, and H3K79 [6].

In vivo, methyl-donor metabolite availability is influenced by common physiologic factors (e.g., diet composition and circadian rhythms) [7–10]. As a result, one may hypothesize the sensitivity of histone methylation to altered SAM availability would pose a threat to human health as dysregulated histone methylation has been associated with negative pathologies including intellectual disability syndromes, cancers, and aging [11]. However, moderate methionine restriction (Met-R) in rodents has been associated with positive phenotypes such as improved glucose tolerance, reduced fat mass, and lifespan extension [12–14]. This creates a potential discrepancy between epigenetic and physiologic phenotypes. Therefore, the primary goal for my Ph.D. research was to determine whether adaptive epigenetic responses to methyl-metabolite depletion exist which support the abundance of critical modifications to prevent detrimental epigenetic dysregulation and promote beneficial Met-R associated phenotypes.

Global histone post-translational modification (PTM) profiling of diverse *in vitro* and whole organism methyl-metabolite depletion systems enabled the identification of H3K9me1 maintenance as a highly conserved response to this metabolic perturbation. In each methyl-metabolite depletion system, global H3K9me1 abundance was unaffected by decreased SAM availability while H3K9me2/3 experienced significantly decreased abundances. I determined maintenance of global H3K9me1 levels was not a passive consequence of H3K9me2/3 demethylation but rather actively maintained by both cytoplasmic and nuclear H3K9me1 HMTs.

This active H3K9 mono-methylation activity was deemed critical for preserving global heterochromatin stability as well as repression of individual transposable and repetitive DNA elements. ChIP-sequencing analyses suggested a remodeling of H3K9me1 around susceptible heterochromatic regions may facilitate this protection of heterochromatin function. Active maintenance of H3K9me1 during methyl-metabolite depletion was also found to be critical for facilitating epigenetic persistence upon metabolic recovery. Excitingly, both acute heterochromatin stability and long-term epigenetic persistence phenotypes appeared to be conserved in young and aged C57BL/6J mice.

Although this work revealed active H3K9me1 HMT activity is critical during methyl-metabolite depletion, it remained unclear how mono-methyl HMT activity was preferentially maintained compared to di-/tri-methyl HMTs. Using fundamental enzymology approaches, I sought to determine whether inherent catalytic properties of mono-methyl HMTs facilitated their retained catalytic activity in low SAM environments. To address this hypothesis, three functionally distinct pairs of H3K9 HMTs were recombinantly purified and assessed using steady-state kinetics and quantitative substrate binding assays. The three pairs of enzymes tested in this analysis included the cytoplasmic H3K9 mono-methyltransferases PRDM3/PRDM16,

nuclear H3K9 mono-/di- methyltransferases EHMT1/EHMT2, and nuclear H3K9 di-/tri-methyltransferases SUV39H1/SUV39H2 [15].

Radiometric EZ-Tip (Enzyme Tip) activity assays revealed cytoplasmic HMTs PRDM3/PRDM16 possess drastically lower k_{cat} values compared to nuclear HMTs, making it unlikely inherent properties of these enzymes would be sufficient in supporting their activity during SAM depletion. Use of physiologically relevant peptide substrates (i.e., $H3K9un^{PEPTIDE}$ for EHMT1/EHMT2 and $H3K9me2^{PEPTIDE}$ for SUV39H1/SUV39H2) also showed $K_{m,\,SAM}$ values are unable to explain preferential mono-methyltransferase activity when SAM availability is limited. However, significantly lower catalytic efficiency values (k_{cat}/K_m) where seen for all nuclear enzymes when provided $H3K9un^{PEPTIDE}$ rather than $H3K9me2^{PEPTIDE}$ substrate. These differences in catalytic efficiency were driven by significant decreases in k_{cat} and were not influenced by altered substrate binding as peptide methylation multiplicity increased. Therefore, greater catalytic efficiency for mono-methylation compared to tri-methylation provides the mechanistic foundation for preferential H3K9me1 HMT activity during SAM depletion.

5.2 Future Directions

5.2.1 Determining Functional Roles for H3K9me1 in Supporting Heterochromatin Stability

Findings from Chapter 2 suggesting H3K9me1 is functionally important for maintaining constitutive heterochromatin stability were unexpected as this function had previously only been associated with di- and tri-methylation at H3K9 [16–18]. H3K9me2/3 regulate constitutive heterochromatin formation and maintenance via their recognition by reader domain (e.g., chromo- and tandem Tudor) containing proteins that subsequently recruit chromatin effectors [19–21]. As the reader domain containing proteins are unable to recognize H3K9me1, the mechanism by which this post-translational modification supports heterochromatin stability is likely unique from H3K9me2/3.

The simplest way H3K9me1 may be mediating heterochromatin maintenance during methyl-metabolite depletion is by acting as a local substrate for H3K9me2/3 methylation. Although our ChIP-sequencing study in Chapter 2 shows a remodeling of H3K9me1 around regions of constitutive heterochromatin where H3K9me3 is lost, we have limited insight into the function of this remodeling as the ChIP-sequencing study did not assess the impact of EHMT1/EHMT2 inhibition under Met-R. For example, it may be possible that although global H3K9me3 levels are not impacted by EHMT1/EHMT2 inhibition during Met-R, genomic loci containing repetitive and transposable elements experience decreased H3K9me3 enrichment and are subsequently derepressed. This may be similarly true for H3K9me2, a modification we have no loci-specific resolution for due to technical limitations.

Another mechanism to consider is adaptive H3K9me1 may act to prevent H3K9 acetylation at newly demethylated loci during Met-R. Spurious H3K9ac could facilitate local de-repression of constitutively silenced DNA elements as well as broad changes in heterochromatin

architecture through the recruitment of histone modifying enzymes, transcription initiation machinery, and chromatin remodelers [22–24]. Loci-specific resolution of H3K9 acetylation changes during Met-R ± Ehmt1/Ehmt2 inhibition will be critical for testing this hypothesis. However, impaired H3K9 deacetylation has previously been associated with global genomic instability and retrotransposable element derepression, providing support for this general mechanism [25–27].

5.2.2 Investigating Roles for Epigenetic Adaptation in Methionine Restriction-Induced Lifespan Extension

A moderate reduction in dietary methionine intake has been shown to stimulate increased maximal lifespan in numerous mammalian model systems [13,14]. This was first demonstrated by Orentreich et al. who showed an 80% dietary methionine reduction in male Fischer 344 rat extended lifespan by 30% [28]. Over time, Met-R induced lifespan extension has been associated with beneficial metabolic reprogramming that includes – but is not limited to – altered lipid metabolism and fat loss, increased energy expenditure, and improved insulin sensitivity [12]. While the mechanism(s) responsible for these positive metabolic and lifespan extension phenotypes have been studied in detail, the focus has largely been on nutrient and hormone signaling. The contribution of epigenetic mechanisms to these phenotypes has been minimally investigated in spite of methionine's role as the obligatory metabolic precursor to SAM.

In Chapter 2, we determined the epigenetic responses to total Met-R which support heterochromatin stability are retained in aged organisms. This was a significant finding as heterochromatin dysregulation is an epigenetic hallmark of aging [29–33], suggesting dietary Met-R may be a successful intervention to preserve genome stability with age. As a result, an exciting hypothesis to consider is that moderate Met-R may also stimulate adaptive regulation of heterochromatin and thereby support Met-R lifespan extension via preservation of genome stability. In this model, epigenetic adaptation to Met-R would not directly regulate genes responsible for supporting the previously noted physiologic phenotypes. Instead, the adaptive response would be critical for maintaining a stable genome that in turn supports Met-R induced regulation of relevant genes and signaling pathways.

5.2.3 Expanding Fundamental Assessment of H3K9 HMT Catalytic Properties

The biochemical assessment of H3K9 HMTs discussed in Chapter 4 reveals mono-methylation reactions are more catalytically efficient than tri-methylation reactions. While this finding provides the mechanistic foundation for active H3K9me1 regulation in response to methyl-metabolite depletion, more detailed biochemical analyses are needed to complete a comprehensive characterization of the chosen H3K9 HMTs (i.e., PRDM3/PRDM16, EHMT1/EHMT2, and SUV39H1/SUV39H2).

Regarding the cytoplasmic H3K9 mono-methyl HMTs PRDM3 and PRDM16, follow-up studies are needed to determine whether their proposed dependence on non-canonical catalytic mechanisms due to lack of SET domain residue conservation is responsible for their low activity [34]. To directly address this hypothesis, site-directed mutagenesis was used to generate consensus sequence corrected PRDM3 (i.e., M189Y, R152N, and M189Y/R152N) and PRDM16 (i.e., V210Y, R173N, and V210Y/R173N) constructs. M/V to Y mutations introduce the final tyrosine residue of the catalytic domain (i.e., ELxF/YDY) while R to N mutations introduce the primary asparagine residue of the SAM binding domain (i.e., NHS/CxxPN). PRDM3 and PRDM16 also share a conserved tyrosine residue (i.e., Y173 and Y194, respectively) with PRDM9 that was proven critical in supporting PRDM9 catalytic activity. Therefore, loss of function PRDM3 (i.e., Y173F) and PRDM16 (i.e., Y194F) constructs were generated as negative controls for this study.

Comprehensiveness of the current H3K9 HMT assessment is also limited by lack of $H3K9me1^{PEPTIDE}$ substrate inclusion. Structural studies suggest H3K9 HMTs are able to direct unmodified lysine positioning for nucleophilic attack of the SAM sulfur atom through coordination via an active site water molecule [35,36]. Presence of a mono-methyl lysine results

in loss of this water molecule which frees a solvent pocket for the methyl-group to reside while simultaneously positioning the lysine ε-amino group for nucleophilic attack of the SAM molecule. While these studies provide structural insights into the accommodation of unmodified and mono-methyl lysines by SET domain methyltransferases, it is unclear how di-methyl lysines are sterically accommodated within the active site. As a result, it is possible differences in catalytic efficiency between mono-/tri-methylation are significantly greater than between mono-/di-methylation. Understanding relative differences in catalytic efficiency across all H3K9 methylation reactions will be critical for understanding the extent to which HMT catalytic properties may support H3K9me1 regulation during methyl-metabolite depletion.

Incorporating H3K9me1^{PEPTIDE} into this study will result in inclusion of all forms of substrate lysine methylation (K_{me}) multiplicity; however, relevance of the results may be limited as peptides are not physiologic substrates for HMTs. Nucleosome core particles (NCPs) are the endogenous substrate for nuclear HMTs and have been shown to significantly influence their catalytic properties [37–43]. This does not discount current conclusions from Chapter 4 which suggest increased K_{me} multiplicity negatively impacts catalytic efficiency as this effect appears to be driven by inherent catalytic properties not substrate interactions. Nonetheless, it is important to test these findings using NCP substrates to better assess their *in vivo* relevance.

5.2.4 Testing H3K9 HMT Biochemistry Insights Under Cellular Methionine Restriction

Translating the HMT biochemistry insights from Chapter 4 into cell-based studies is needed to assess their relevance in supporting the epigenetic response to methyl-metabolite depletion presented in Chapter 2. These insights suggest greater catalytic efficiency for H3K9 mono-methylation relative to tri-methylation would support epigenetic adaptation to methyl-metabolite depletion.

In vivo, only EHMT1/EHMT2 catalyze nuclear H3K9me1 while SUV39H1/SUV39H2 are restricted to H3K9 di-/tri-methylation. As a result, SUV39H1/SUV39H2 are thought to be largely inactive under SAM depleted conditions. Therefore, it would be possible to directly test the H3K9me1 catalytic efficiency model by mutating SUV39H1 and/or SUV39H2 to mono-methyltransferases and in an attempt to rescue their catalytic activity during methyl-metabolite depletion. Following this conversion, cells expressing endogenously mutated SUV39H1^{K9me1} and/or SUV39H2^{K9me1} could be subjected to Met-R ± EHMT1/EHMT2 small molecule inhibition to determine whether H3K9me1 levels are negatively impacted similarly to wild-type controls. Decreased impact on global H3K9me1 levels in SUV39H1^{K9me1} and/or SUV39H2^{K9me1} cells would provide cell-based support for the model by revealing novel mono-methyl activity from non-EHMT1/EHMT2 HMTs is capable of maintaining global H3K9me1 levels during SAM depletion. Existing literature suggest it may be possible to change the catalytic specificity of SUV39H1 and SUV39H2 through a simple phenylalanine (Phe) to tyrosine (Tyr) mutation. Collins et al., 2005 identified a Phe/Tyr switch in SET domain-containing HMTs that largely dictates whether an enzyme is restricted to mono-methylation or can perform subsequent di-/tri-methylation reactions [44]. For example, presence of a Phe in the corresponding position of F1152 in EHMT2 allows for recombinant enzyme di-/tri-methylation while an F1152Y mutation

restricts enzyme catalysis to mono-methylation [35,44]. SUV39H1 and SUV39H2 also contain conserved the Phe/Tyr switch residue (i.e., F363 and F370, respectively), providing an opportunity to change the catalytic specificity of these enzymes to strict H3K9 mono-methyltransferases [35].

An alternative approach for testing the catalytic efficiency model would be to mutate SUV39H1 and/or SUV39H2 into more efficient H3K9 di-/tri-methyltransferases. If achievable, the current model suggests the activity of SUV39H1 and/or SUV39H2 would be rescued, resulting in H3K9me2/3 becoming less susceptible to SAM depletion. Unfortunately, it is unclear how to introduce SET domain di-/tri-methylation gain-of-function mutations. Stearic restrictions in the SET domain active site are believed to significantly contribute to decreased di-/tri-methyltransferase catalytic activity [45]. Restructuring of the SET domain active site might then be necessary to relieve such restrictions; however, this may result in compromising critical contacts between the active site, SAM, and substrate, ultimately leading to decreased catalytic activity.

It is important to note that an inability of either approach to support the catalytic efficiency model would not suggest increased efficiency for mono-methylation reactions is irrelevant during SAM depletion. This fundamental catalytic property of H3K9 HMTs may be critical in combination with other supporting mechanisms such as those proposed in Chapter 5.2.5.

5.2.5 Evaluating Mechanisms of Nuclear SAM Synthesis During Methyl-Metabolite Depletion

Numerous enzymes originally characterized based on their metabolic functions have recently been identified as critical epigenetic regulators. Such enzymes alter the epigenome via production of metabolic cofactors that either support or inhibit the catalytic activity of chromatin modifying enzymes. Interestingly, many of these metabolic enzymes appear capable of directly regulating the epigenome from within the nucleus via general or loci-specific cofactor production [2,3,46]. To date this mechanism is best studied regarding Krebs cycle (e.g., PDH and IDH1) and non-mitochondrial acetyl-CoA producing (e.g., ACSS2 and ACLY) enzymes.

Unpublished, preliminary data suggest the systemic mammalian SAM synthetase methionine adenosyltransferase IIα (MATIIα) may have nuclear-specific functions during methyl-metabolite depletion. To begin summarizing this preliminary data, RT-qPCR was first used to quantify relative transcript levels of both MATIIα and its regulatory subunit MATIIβ over 24 hours of Met-R in HCT116 *H. sapiens* colorectal cancer cells. MATIIα transcript abundance responded significantly and rapidly to Met-R, increasing nearly 5-fold after 2 hours and greater than 35-fold after 24 hours (Figure 5-1A). Unlike MATIIα, the MATIIβ transcriptional response to Met-R was delayed and significantly lower in magnitude. MATIIβ transcript levels increased by just 2-fold after 24 hours of Met-R (Figure 5-1B). These data indicate dynamic transcriptional regulation of MATIIα, but not MATIIβ, may be critical for supporting epigenetic adaptation to methyl-metabolite depletion.

SILAC proteomics results presented in Chapter 2 suggest newly transcribed MATIIα mRNA facilitates the translation and accumulation of MATIIα protein during Met-R (Figure 2-5I). Immunoblot assays confirmed these results, revealing a 2-fold increase in whole-cell MATIIα protein abundance over 24 hours of Met-R (Figure 5-1C, 5-1E). The discrepancy

between MATIIα transcript and whole-cell protein abundance was largely expected as Met-R is known to inhibit translation initiation and polysome formation [47]. Therefore, as these data show MATIIα is both actively transcribed and translated during Met-R, SAM synthesis appears to be a critical cellular function under this condition.

MATIIα-dependent SAM synthesis is known to support important biological processes both in and outside of the nucleus. For example, the synthesis of one phosphatidylcholine molecule requires three molecules of SAM be consumed [48]. Therefore, it was important to follow-up on the previously described transcriptional and translational response data to determine if nuclear MATIIα occupancy is specifically altered under methyl-metabolite depletion. To begin revealing the importance of nuclear SAM synthesis under Met-R, immunoblot analyses of subcellularly fractionated cytoplasmic and nuclear pools from HCT116 cells was used to quantify relative changes in MATIIα protein abundance within each compartment. Cytoplasmic MATIIα protein abundance was determined to respond similarly as whole-cell levels, increasing by 2-fold after 24 hours of Met-R (Figure 5-1E, 5-1F). Interestingly, nuclear MATIIα protein abundance increased by nearly 5-fold after 24 hours of Met-R (Figure 5-1E, 5-1F). A greater accumulation of MATIIα in the nucleus relative to whole-cell and cytoplasmic increases suggests MATIIα may be actively translocated into the nucleus under this condition. Immunoblot results were validated via immunofluorescence, showing the cytoplasmic increase in MATIIα protein abundance is accompanied by a relatively greater accumulation of nuclear MATIIα (Figure 5-1G). Together, these data indicate nuclear SAM synthesis dynamically responds to methyl-metabolite depletion.

These preliminary results raise numerous exciting questions about the possible mechanisms of MATIIα nuclear accumulation and function. Regarding potential mechanisms of

MATIIα nuclear accumulation, it is interesting to note the initial MATIIα transcriptional response to Met-R correlates temporally with onset of the adaptive epigenetic response described in Chapter 2. This suggests SAM depletion independent of methionine availability may be the signal that ultimately initiates dynamic changes in MATIIα protein abundance and subcellular localization. It has recently been shown that cytoplasmic SAM availability can directly regulate mechanistic target of rapamycin complex 1 (mTORC1) activity via S-adenosylmethionine sensor upstream of mTORC1 (SAMTOR) [49]. This provides a potential mechanism by which decreased SAM availability may stimulate MATIIα transcription as mTORC1 activity is known to directly influence gene expression by altering transcription factor activity [50].

Met-R stimulated increases in MATIIα protein abundance as a consequence of its transcriptional upregulation may not alone be sufficient in driving MATIIα into the nucleus. The molecular weight of a MATIIα monomer (i.e., ~44kDa) is near, but below, the proposed upper protein size limit (i.e., ~60kDa) for passive diffusion through the nuclear pore complex (NPC) [51–55]. However, it is unclear whether MATIIα predominantly exists as a monomer in the cell. Structural studies suggest MATIIα and MATIIβ share a low nanomolar dissociation constant (i.e., K_d = 8.77 nM) and readily adopt a 2:1 MATIIα:MATIIβ trimeric complex *in vitro* [56]. Such a trimeric MATIIα/MATIIβ complex would possess a molecular weight of ~125kDa, far above the upper size limit for passive diffusion through the NPC. A protein complex of this size would require active transport through the NPC which is tightly regulated. One major mechanism that regulates transport through an NPC is protein phosphorylation [57]. Interestingly, the activity and specificity of protein phosphatase 2A (PP2A) has been shown to be dynamically regulated by SAM availability and dictates the subcellular localization of the

histone demethylase Rph1 in *S. cerevisiae* [6,58]. This provides precedence for a similar mechanism to regulate MATIIα nuclear occupancy during methyl-metabolite depletion.

Once in the nucleus, MATIIα activity may support epigenetic adaptation to methyl-metabolite depletion via numerous avenues. The simplest mechanism would be nuclear MATIIα activity is critical for generating and sustaining a local, nucleus-specific pool of SAM for use by HMTs. As results described in Chapter 4 suggest a greater catalytic efficiency for mono-methylation relative to tri-methylation is a conserved feature of SET domain-containing HMTs, general nuclear SAM synthesis could be capable of supporting mono-methyl HMT activity. This may be especially true if MATIIα activity occurs at specific genomic loci to support the adaptive mono-methylation events detailed in Chapter 2. However, as MATIIα-dependent SAM synthesis relies on adequate methionine availability, it is possible nuclear MATIIα activity during Met-R may require complex formation with MATIIβ. Upon binding with MATIIβ, the MATIIα $K_{m,\ Methionine}$ decreases significantly [59–62]. While complex formation also increases MATIIα product inhibition by SAM, this would unlikely impact MATIIα activity under Met-R as SAM availability is significantly depleted. Therefore, a MATIIα/MATIIβ complex would likely result in more catalytically efficient SAM synthesis when methionine availability is limited.

Beyond general or loci-specific SAM synthesis, nuclear MATIIα activity could also support epigenetic adaptation to methyl-metabolite depletion via direct shuttling of newly synthesized SAM to HMTs. This would be the most efficient mechanism of SAM production and utilization under the assumption that 100% of all newly synthesized SAM would be immediately consumed. This efficiency would significantly benefit a methionine depleted cell/organism as SAM is energetically expensive to synthesize and notoriously unstable [63]. Similar mechanisms have been proposed under the contexts of serine metabolism in *S. cerevisiae*

and oxidative stress in *M. musculus* embryonic fibroblasts [64,65]. Tools detailed in Chapters 3 and 4, along with recombinant full length MATIIα readily purified in the Denu laboratory, provide the framework to begin testing this hypothesis *in vitro*. For example, size exclusion chromatography and/or crosslinking mass spectrometry could be employed to identify *in vitro* MATIIα-HMT interactions. The EZ-Tip assay described in Chapter 3 could also be used to determine whether HMT catalysis is influenced by the source of SAM (i.e., coming directly from MATIIα as opposed to being freely available in solution). It should be noted that many of the HMT constructs from Chapter 4 are limited to SET domain catalytic subunits, making it possible potential contact points between MATIIα and these HMTs may not be present. As a result, it may be necessary to follow-up on negative results by assessing the binding capabilities of full-length HMTs. It will also be important for future studies to investigate SAM shuttling mechanisms involving cytoplasmic mono-methyltransferases as HMTs in this compartment have greater competition for the metabolite with other SAM consuming enzymes.

Figure 5-1: MATIIα Abundance and Localization is Regulated by Methyl-Metabolite Depletion. Scatter plots of relative (*A*) MATIIα and (*B*) MATIIβ mRNA abundance cells as measured by RT-qPCR. Error bars represent SD, n=3, *p<0.05 (Welch's t-Test). Scatter plots of relative (*C*) whole-cell and (*D*) sub-cellular specific MATIIα protein levels as measured by immunoblots. See panels (*E*) and (*F*) for representative immunoblot images as well as REVERT Total Protein Stain images used for normalization. Error bars represent SD, n≥2, *p<0.05 (Welch's t-Test). (*G*) Immunofluorescence images of HCT116 cells. Blue signal is from nuclear DAPI stain while green signal is from MATIIα antibody.

Figure 5-1: MATIIα Abundance and Localization is Regulated by Methyl-Metabolite Depletion.

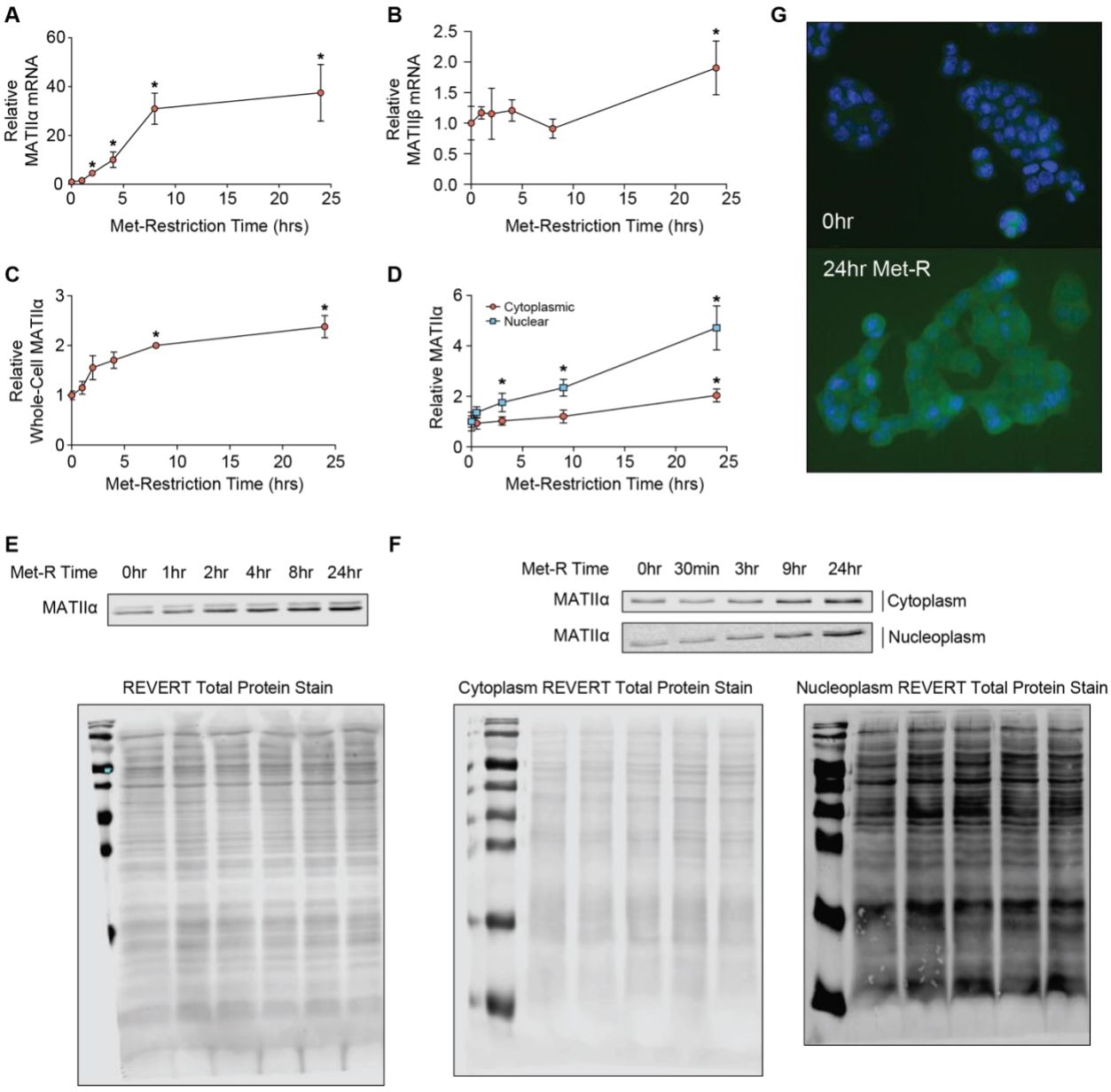

5.3 Impact Statement

The interdependence between metabolism and the epigenome has become greatly appreciated as a major pathway for chromatin regulation. Prior to this work, many studies have highlighted the susceptibility of individual epigenetic modifications to fluctuations in metabolite cofactor availability. Here, with a focus on the relationship between histone methylation and methyl-donor metabolism, I show all forms of histone methylation are not equally susceptible to SAM depletion. This is due to the presence of highly conserved epigenetic responses which actively regulate the abundance and genomic distribution of a critical modification (i.e., H3K9me1). This modification facilitates the preservation of heterochromatin stability under SAM depletion as well as long-term epigenetic persistence upon metabolic recovery. Conservation of this response in young and aged *M. musculus* highlights the physiological relevance of these findings. Furthermore, through the use of fundamental enzymology approaches, I determined favorable inherent catalytic properties of the histone methyltransferases which deposit H3K9me1 provide the mechanistic foundation for its active maintenance. Together, these results uncovered novel mechanisms by which the epigenome is capable of sensing and responding to metabolic perturbations, revealing critical roles the epigenome can hold during periods of metabolic stress.

5.4 References

1. Haws, S. A. et al. (2020) Metabolism and the Epigenome: A Dynamic Relationship. *Trends Biochem. Sci.* 45, 731–747.
2. Boon, R. et al. (2020) Nuclear metabolism and the regulation of the epigenome. *Nature Metabolism* **2**, 1190–1203 (2020).
3. Dai, Z. et al. (2020) The evolving metabolic landscape of chromatin biology and epigenetics. *Nature Reviews Genetics*. 21, 737–753.
4. Mentch, S. J. & Locasale, J. W. (2016) One-carbon metabolism and epigenetics: understanding the specificity. *Ann. N. Y. Acad. Sci.* 1363, 91–98.
5. Mentch, S. J. et al. (2015) Histone Methylation Dynamics and Gene Regulation Occur through the Sensing of One-Carbon Metabolism. *Cell Metab.* 22, 861–873.
6. Ye, C. et al. (2017) A Metabolic Function for Phospholipid and Histone Methylation. *Mol.r Cell.* 66, 180-193.
7. Farmer, B. (2014) Nutritional adequacy of plant-based diets for weight management: observations from the NHANES. *Am. J. Clin. Nutr.* 100, 365S-368S.
8. Schmidt, J. A. et al. (2016) Plasma concentrations and intakes of amino acids in male meat-eaters, fish-eaters, vegetarians and vegans: a cross-sectional analysis in the EPIC-Oxford cohort. *Eur. J. Clin. Nutr.* 70, 306–312.
9. Krishnaiah, S. Y. et al. (2017) Clock Regulation of Metabolites Reveals Coupling between Transcription and Metabolism. *Cell Metab.* 25, 961-974.
10. Greco, C. M. et al. (2020) S-adenosyl-l-homocysteine hydrolase links methionine metabolism to the circadian clock and chromatin remodeling. *Science Advances.* 6, eabc5629.

11. Greer, E. L. & Shi, Y. (2012) Histone methylation: a dynamic mark in health, disease and inheritance. *Nat. Rev. Genet.* 13, 343–357.
12. Green, C. L. & Lamming, D. W. (2019) Regulation of metabolic health by essential dietary amino acids. *Mechanisms of Ageing and Development.* 177, 186–200.
13. Brown-Borg, H. M. (2016) Reduced growth hormone signaling and methionine restriction: interventions that improve metabolic health and extend life span. *Ann. N. Y. Acad. Sci.* 1363, 40–49.
14. Brown-Borg, H. M. & Buffenstein, R. (2017) Cutting back on the essentials: Can manipulating intake of specific amino acids modulate health and lifespan? *Ageing Research Reviews.* 39, 87–95.
15. Hyun, K. et al. (2017) Writing, erasing and reading histone lysine methylations. *Experimental & Molecular Medicine.* 49, e324–e324.
16. Peters, A. H. et al. (2001) Loss of the Suv39h histone methyltransferases impairs mammalian heterochromatin and genome stability. *Cell.* 107, 323–337.
17. Loyola, A. et al. (2009) The HP1alpha-CAF1-SetDB1-containing complex provides H3K9me1 for Suv39-mediated K9me3 in pericentric heterochromatin. *EMBO Rep.* 10, 769–775.
18. Saksouk, N. et al. (2015) Constitutive heterochromatin formation and transcription in mammals. *Epigenetics & Chromatin.* 8, 3.
19. Lachner, M. et al. (2001) Methylation of histone H3 lysine 9 creates a binding site for HP1 proteins. *Nature.* 410, 116–120.
20. Janssen, A. et al. (2018) Heterochromatin: Guardian of the Genome. *Annual Review of Cell and Developmental Biology.* 34, 265–288.

21. Allshire, R. C. & Madhani, H. D. (2018) Ten principles of heterochromatin formation and function. *Nature Reviews Molecular Cell Biology*. 19, 229–244.

22. Fujisawa, T. & Filippakopoulos, P. (2017) Functions of bromodomain-containing proteins and their roles in homeostasis and cancer. *Nature Reviews Molecular Cell Biology*. 18, 246–262.

23. Gates, L. A. et al. (2017) Acetylation on histone H3 lysine 9 mediates a switch from transcription initiation to elongation. *J. Biol. Chem.* 292, 14456–14472.

24. Zhao, D. et al. (2017) YEATS Domain—A Histone Acylation Reader in Health and Disease. *Journal of Molecular Biology*. 429, 1994–2002.

25. Mostoslavsky, R. et al. (2006) Genomic instability and aging-like phenotype in the absence of mammalian SIRT6. *Cell.* 124, 315–329.

26. Simon, M. et al. (2019) LINE1 Derepression in Aged Wild-Type and SIRT6-Deficient Mice Drives Inflammation. *Cell Metab.* 29, 871-885.

27. Van Meter, M. et al. (2014) SIRT6 represses LINE1 retrotransposons by ribosylating KAP1 but this repression fails with stress and age. *Nat. Commun.* 5, 5011.

28. Orentreich, N. et al. (1993) A. Low Methionine Ingestion by Rats Extends Life Span. *J. Nutr.* 123, 269–274.

29. Booth, L. N. & Brunet, A. (2016) The Aging Epigenome. *Mol. Cell.* 62, 728–744.

30. De Cecco, M. et al. (2019) L1 drives IFN in senescent cells and promotes age-associated inflammation. *Nature.* 566, 73–78.

31. De Cecco, M. et al. (2013) Genomes of replicatively senescent cells undergo global epigenetic changes leading to gene silencing and activation of transposable elements. *Aging Cell.* 12, 247–256.

32. Oberdoerffer, P. & Sinclair, D. A. (2007) The role of nuclear architecture in genomic instability and ageing. *Nat. Rev. Mol. Cell Biol.* 8, 692–702.

33. Wood, J. G. et al. (2016) Chromatin-modifying genetic interventions suppress age-associated transposable element activation and extend life span in Drosophila. *Proc. Natl. Acad. Sci. U.S.A.* 113, 11277–11282.

34. Wu, H. et al. (2013) Molecular Basis for the Regulation of the H3K4 Methyltransferase Activity of PRDM9. *Cell Reports.* 5, 13–20.

35. Couture, J.-F. et al. (2008) Structural origins for the product specificity of SET domain protein methyltransferases. *PNAS.* 105, 20659–20664.

36. Rizzo, P. A. D. et al. (2010) SET7/9 Catalytic Mutants Reveal the Role of Active Site Water Molecules in Lysine Multiple Methylation. *Journal of Biological Chemistry.* 285, 31849–31858.

37. Janna, A. et al. (2020) Structural Paradigms in the Recognition of the Nucleosome Core Particle by Histone Lysine Methyltransferases. *Front. Cell Dev. Biol.* 8.

38. Qu, Q. et al. (2018) Structure and Conformational Dynamics of a COMPASS Histone H3K4 Methyltransferase Complex. *Cell.* 174, 1117-1126.e12.

39. Hsu, P. L. et al. (2018) Crystal Structure of the COMPASS H3K4 Methyltransferase Catalytic Module. *Cell.* 174, 1106-1116.

40. Valencia-Sánchez, M. I. et al. (2019) Structural Basis of Dot1L Stimulation by Histone H2B Lysine 120 Ubiquitination. *Mol. Cell.* 74, 1010-1019.

41. Worden, E. J. et al. (2019) Mechanism of Cross-talk between H2B Ubiquitination and H3 Methylation by Dot1L. *Cell.* 176, 1490-1501.

42. Li, W. et al. (2021) Molecular basis of nucleosomal H3K36 methylation by NSD methyltransferases. *Nature.* 590, 498–503.

43. Poepsel, S. et al. (2018) Cryo-EM structures of PRC2 simultaneously engaged with two functionally distinct nucleosomes. *Nat. Struct. Mol. Biol.* 25, 154–162.

44. Collins, R. E. et al. (2005) In Vitro and in Vivo Analyses of a Phe/Tyr Switch Controlling Product Specificity of Histone Lysine Methyltransferases. *Journal of Biological Chemistry.* 280, 5563–5570.

45. Qian, C. & Zhou, M.-M. (2006) SET domain protein lysine methyltransferases: Structure, specificity and catalysis. *Cell. Mol. Life Sci.* 63, 2755–2763.

46. Haws, S. A. et al. (2020) Methyl-Metabolite Depletion Elicits Adaptive Responses to Support Heterochromatin Stability and Epigenetic Persistence. *Mol. Cell.* 78, 210-223.

47. Mazor, K. M. et al. (2018) Effects of single amino acid deficiency on mRNA translation are markedly different for methionine versus leucine. *Sci. Rep.* 8, 8076.

48. Kent, C. & Carman, G. M. (1999) Interactions among pathways for phosphatidylcholine metabolism, CTP synthesis and secretion through the Golgi apparatus. *Trends Biochem. Sci.* 24, 146–150.

49. Gu, X. et al. (2017) SAMTOR is an S-adenosylmethionine sensor for the mTORC1 pathway. *Science.* 358, 813–818.

50. Laplante, M. & Sabatini, D. M. (2013) Regulation of mTORC1 and its impact on gene expression at a glance. *J. Cell. Sci.* 126, 1713–1719.

51. Weis, K. (2003) Regulating access to the genome: nucleocytoplasmic transport throughout the cell cycle. *Cell.* 112, 441–451.

52. Vasu, S. K. & Forbes, D. J. (2001) Nuclear pores and nuclear assembly. *Curr. Opin. Cell. Biol.* 13, 363–375.

53. Mattaj, I. W. & Englmeier, L. (1998) Nucleocytoplasmic transport: the soluble phase. *Annu. Rev. Biochem.* 67, 265–306.

54. Görlich, D. & Kutay, U. (1999) Transport between the cell nucleus and the cytoplasm. *Annu. Rev. Cell. Dev. Biol.* 15, 607–660.

55. Rout, M. P. & Aitchison, J. D. (2001) The nuclear pore complex as a transport machine. *J. Biol. Chem.* 276, 16593–16596.

56. Murray, B. et al. (2014) Structure and function study of the complex that synthesizes S-adenosylmethionine. *IUCrJ.* 1, 240–249.

57. Wente, S. R. & Rout, M. P. (2010) The Nuclear Pore Complex and Nuclear Transport. *Cold Spring Harb Perspect. Biol.* 2, a000562.

58. Ye, C. et al. (2019) Demethylation of the Protein Phosphatase PP2A Promotes Demethylation of Histones to Enable Their Function as a Methyl Group Sink. *Mol. Cell.* 73, 1115-1126.

59. Halim, A.-B. et al. (1999) Expression and Functional Interaction of the Catalytic and Regulatory Subunits of Human Methionine Adenosyltransferase in Mammalian Cells. *J. Biol. Chem.* 274, 29720–29725.

60. LeGros, H. L. et al. (2000) Cloning, Expression, and Functional Characterization of the β Regulatory Subunit of Human Methionine Adenosyltransferase (MAT II). *J. Biol. Chem.* 275, 2359–2366.

61. Markham, G. D. & Pajares, M. A. (2009) Structure-function relationships in methionine adenosyltransferases. *Cell. Mol. Life. Sci.* 66, 636–648.

62. Quinlan, C. L. et al. (2017) Targeting S -adenosylmethionine biosynthesis with a novel allosteric inhibitor of Mat2A. *Nat. Chem. Biol.* 13, 785–792.

63. Wu, S. E. et al. (1983) Chiral instability at sulfur of S-adenosylmethionine. *Biochemistry.* 22, 2828–2832.

64. Li, S. et al. (2015) Serine and SAM Responsive Complex SESAME Regulates Histone Modification Crosstalk by Sensing Cellular Metabolism. *Mol. Cell* 60, 408–421.

65. Kera, Y. et al. (2013) Methionine Adenosyltransferase II-dependent Histone H3K9 Methylation at the COX-2 Gene Locus. *J. Biol. Chem.* 288, 13592–13601.